UNIVERSITY of CALIFORNIA
Santa Barbara

Correlated Spectroscopic Study of Doped Semiconductor Nanocrystals

A Dissertation submitted in partial satisfaction of the
requirements for the degree

Doctor of Philosophy
in
Chemistry

by

Orlando E. Raola

Committee in charge:

Professor Geoffrey F. Strouse, Chair
Professor Steve K. Buratto
Professor Anthony K. Cheetham
Professor Richard J. Watts

December 2004

The dissertation of Orlando E. Raola is approved.

Professor Steve K. Buratto

Professor Anthony K. Cheetham

Professor Richard J. Watts

Professor Geoffrey F. Strouse, Committee Chair

December 2004

Correlated Spectroscopic Study
of Doped Semiconductor Nanocrystals

by

Orlando E. Raola

To all those who trusted me

on the winding road to this summit

I dedicate this work with love.

Acknowledgements

> “No man is an island, entire of itself; every man is a piece of the continent.”
>
> John Donne
> *Devotions*, 1624

It is a great pleasure for me to acknowledge the inspiration, encouragement and support received from so many people and institutions during these challenging years:

- Dr. Victor K. Chia, at Charles Evans and Associates, for pointing in a blunt manner the way to go;
- Dr. Nicholas Winter, at Lawrence Livermore National Laboratory, who was the first person to know, in a quiet Spring afternoon up in the hill of CalState Hayward of my dreaming about a doctorate;
- Dr. Joy C. Andrews, at California State University, Hayward, for the trust and encouragement to go for it, and for taking me for the first time to a synchrotron facility;
- Dr. Jun Kawai at Kyoto University, Japan; and Dr. Hellmutt Eckert at Westfälische Wilhelms-Universität Münster, in Germany, for the research experiences of a lifetime and for the reassurance that we live in one only world;
- Dr. Thomas Proffen at Lujan Neutron Science Center in Los Alamos National Laboratory, for opening the doors to wonderful neutron science;

Thanks to my advisor Professor Geoffrey F. Strouse for all the good science we have discovered in our join effort. He and the present and past members of his research group at the University of California Santa Barbara, provided all along the way a nurturing and demanding environment where I could grow as a scientist. I am also grateful for the stimulating discussions and fruitful interaction with many other faculty members here: Professors Bernard Kirtman, Anthony K. Cheetham and Galen Stucky, and Lecturers Leroy Leverman and Petra Van Koppen.

The work of the Chemistry Department staff made our lives easier during these years and due thanks go to Deedrea Edgard, Erika James, Dr. James Pavlovich and Dr. Paul Weakliem.

Thanks to the National Science Foundation and to the Eugene Cota-Robles Fellowship at University of California Santa Barbara, for their support was a key factor that allowed me to get through graduate school.

Part of this work made use of MRL Central Facilities supported by the National Science Foundation under award No. DMR96-32716.

Some experimental work reported here was carried out at Argonne National Laboratory Advanced Photon Source(ANL-APS). Thanks to CMC-CAT at ANL-APS. The collaboration with Drs. Tony van Büren and Louis Terminello at Lawerence Livermore National Laboratory is also acknowledged.

Thanks to the many good teachers and professors who kindled my scientific curiosity and at the same time educated my perseverance so that I could endure in sanity a lifelong dedication to the pursuit of knowledge.

Thanks to my parents and siblings for their distant and ever present inspira-

tion.

And for their great patience, understanding and unyielding support, the deepest thanks award goes to my close family: Elsa, Abel and Nora.

To all of you, thanks from the heart.

Curriculum Vitæ

Orlando E. Raola

Personal

Born	November 13, 1955 Havana, Cuba

Professional Employment

1999 to date	Graduate student researcher. Department of Chemistry and Biochemistry, University of California Santa Barbara, Calif.
1998–1999	XRF Applications Specialist. Kevex Instruments, Valencia, Calif.
1996–1998	Chemist. Matheson Gas Products Newark, Calif.
1995–1996	Chemist. General Chemical Corp. Pittsburg, Calif.
1994–1995	Chemist. Charles Evans & Assoc. Redwood City, Calif.
1981–1990	Researcher. Metallurgical Research Center Havana, Cuba.
1978–1981	Chemist. Nicaro Nickel Plant Holguin, Cuba.

Education

1973–1978	University of Havana Havana, Cuba B. S. in Chemistry (*Sp.* Licenciado en Química)
1998–1999	M.S. in Chemistry California State University Hayward, California.
1999-2003	University of California Santa Barbara. Ph. D. in Chemistry. April 2004 (expected)

Awards

NSF Graduate Research Fellowship, awarded 2001.

Eugene Cota-Robles Fellowship, University of California Santa Barbara, awarded 1999.

Publications

Raola, O. E.; Strouse, G. F.; Eckert, H.; Mosel, B. "Local structure and oxidation state of europium in europium-doped cadmium selenide nanocrystals", *J. Amer. Chem. Soc.*, 2004 (submitted).

Raola, O. E. and G. F. Strouse (2002). "Synthesis and characterization of Eu-doped cadmium selenide nanocrystals." *Nano Letters* 2(12): 1443-1447.

Kawai, J; Tohno, S.; Kitajima, Y.; Raola, O. E.; Takaoka, M. "Depth selective chemical state analysis of Pb and S in fly ash in municipal solid waste incinerators using X-ray absorption spectroscopy". (2003) S*pectrochimica Acta B,* 58(4): 635-639.

Fields of Study

Major field: Chemistry

Studies in inorganic spectroscopic methods with Geoffrey F. Strouse.

Studies in x-ray absorption spectroscopy with Joy C. Andrews

Abstract

Correlated Spectroscopic Study
of Doped Semiconductor Nanocrystals

by

Orlando E. Raola

Semiconductor nanocrystals are a class of novel materials with size-dependent properties that can be further tuned by the controlled introduction of guest ions. A series of CdSe:Eu nanocrystal alloys (x = 0 – 0.206) were prepared by adapting a single source precursor growth methodology. Their systematic characterization included the application of core-electron spectroscopies (XPS, XANES, EXAFS) and scattering techniques (p-XRD, p-ND), as well as nuclear γ-absorption resonance (Mössbauer) spectroscopy in order to provide answers to the fundamental question: where does the dopant ion reside in a doped nanocrystal?

Most of the work was directed towards the study of the local structure and oxidation state of europium in europium-doped cadmium selenide nanocrystal alloys. Even if europium is introduced as Eu(II) into the reaction and the whole system is kept under nitrogen, the Eu readily oxidizes to Eu(III) under the reaction conditions. The oxidation state change upon alloy formation is confirmed by XANES, Mössbauer, and XPS analysis on the alloy samples. The correlated data suggests a model of interstitial doping onto the octahedral holes of the wurtzite-type CdSe lattice, the presence of significant lattice distortion and generation of Cd vacancies (2 Eu(III) replace 3 Cd(II) for charge balancing) with the overall

effect of lattice contraction, as revealed by XRD. The coordination around the europium ions close to six, consistent with an O_h coordination of Se around the Eu ion instead of a T_d coordination as expected for a non-disturbed ion substitution on a Cd center. The EXAFS data furthermore shows an indication of the degree of local lattice distortion about the Eu center introduced in the nanocrystal by the doping, due to the lack of second-shell data for Eu or Se, but a clear second shell around Cd. The local lattice distortion introduced at the Eu center explains the observation of the appearance of new vibrational modes in the resonant Raman spectra that correlate with increased Eu doping levels. The new local modes apparently arise from symmetry breaking. The study also included other nanocrystalline systems, such as cobalt-doped cadmium selenide and manganese-doped zinc oxide. These findings provide a sound scientific basis for future developments of applications based on the electrooptic and magnetic properties of these materials.

Contents

List of Tables

List of Figures

Chapter 1

Introduction

> "The principles of physics, as far as I can see, do not speak against the possibility of maneuvering things atom by atom. . . . The problems of chemistry and biology can be greatly helped if our ability to see what we are doing, and to do things on an atomic level, is ultimately developed—a development which I think cannot be avoided."
>
> Richard Feynman
> Caltech, Pasadena, CA, 12/29/1959

1.1 Nanocrystalline semiconductor materials

The evolution of science and technology is in great part determined by the availability of new materials with the desired physical and chemical properties, to such an extent that the different stages of human development received their names from the main material shaping the lives at those times: The Stone Age, The Iron Age. Today we are living what has been called The Information Age, and even if Information is not a material, absolutely every aspect of its phenomenal growth is directly linked to progress in the field of semiconductor electronic, optic and magnetic materials.

The race towards ever diminishing dimensions (as shown in the International Technology Roadmap for Semiconductors [3]) is right now leaving behind microelectronics and moving into an area where the dimension of the features are expressed in nanometers. We are approaching the point where materials can be produced in the ultimate "bottom-up" fashion by the manipulation of individual atoms and molecules, as predicted by Feynman in 1959.

But the process of ever decreasing the dimensions of devices meets physical boundaries when we start working at this length scale. It was reported in 1981, that as the size of CuCl crystallites dispersed in a silicate glass dropped to ~3 nm, a blue shift was observed in the main exciton absorption [4]. In this case, the dimensions of a particle approach the average distance between an electron and a hole for the excited state wavefunction in the material (Bohr radius of the exciton) and the energy required to promote the electron from the valence to conduction band (E^* exciton energy) becomes dependent on the radius of the particle (R). This *quantum confinement effect* was understood by L. Brus and fit to a simple model of the particle-in-a-box, which predicts an increase in the spacing between the allowed levels as the dimensions of the box are reduced (Figure 1.1). Further development of this idea and improvements in the techniques used to prepare polycrystalline semiconductors, as reviewed by Murray and coworkers [5], provided the experimental basis for the derivation of the equation:

$$E^* \simeq E_g + \frac{\hbar^2\pi^2}{2R^2}\left[\frac{1}{m_e^*} + \frac{1}{m_h^*}\right] - \frac{1}{4\pi\epsilon\epsilon_0}\frac{e^2}{R} + \text{smaller terms}$$

besides the terms already defined, m_e^* and m_h^* are the effective mass of the electron and the hole, respectively, ϵ and ϵ_0 are the permeability of the semiconductor and of vacuum respectively. The original constants in the equation have been modified to reflect SI units. The transition between a bulk semiconductor and isolated molecules is represented in Figure 1.1

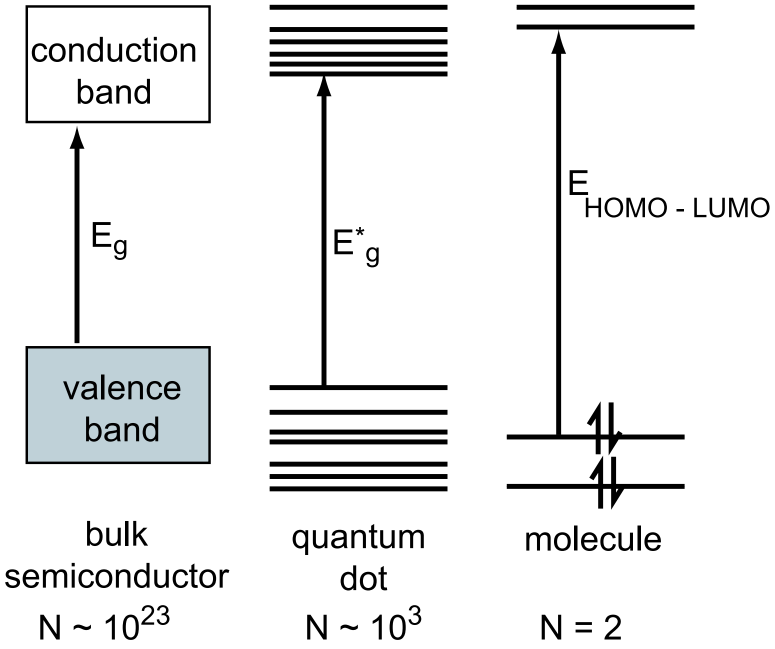

Figure 1.1. Schematic of the band gap opening as the dimensions of the particle are reduced

The absorption energy size dependence for the first excitonic transition is plotted in Figure 1.2, that shows experimental data for cadmium selenide nanoparticles together with a plot of the calculated energy based on Brus's equation without correction ("smaller terms" ignored) and with a correction term linearly dependent on the particle radius. The quantum confinement regime can be observed for nanocrystals with diameter up to 14 nm, of the order of twice the Bohr radius of the exciton in bulk CdSe (around 5 nm) [6].

Nanomaterials of binary semiconductors have been well-studied and their quantum size have been observed and characterized. A summary of the most common

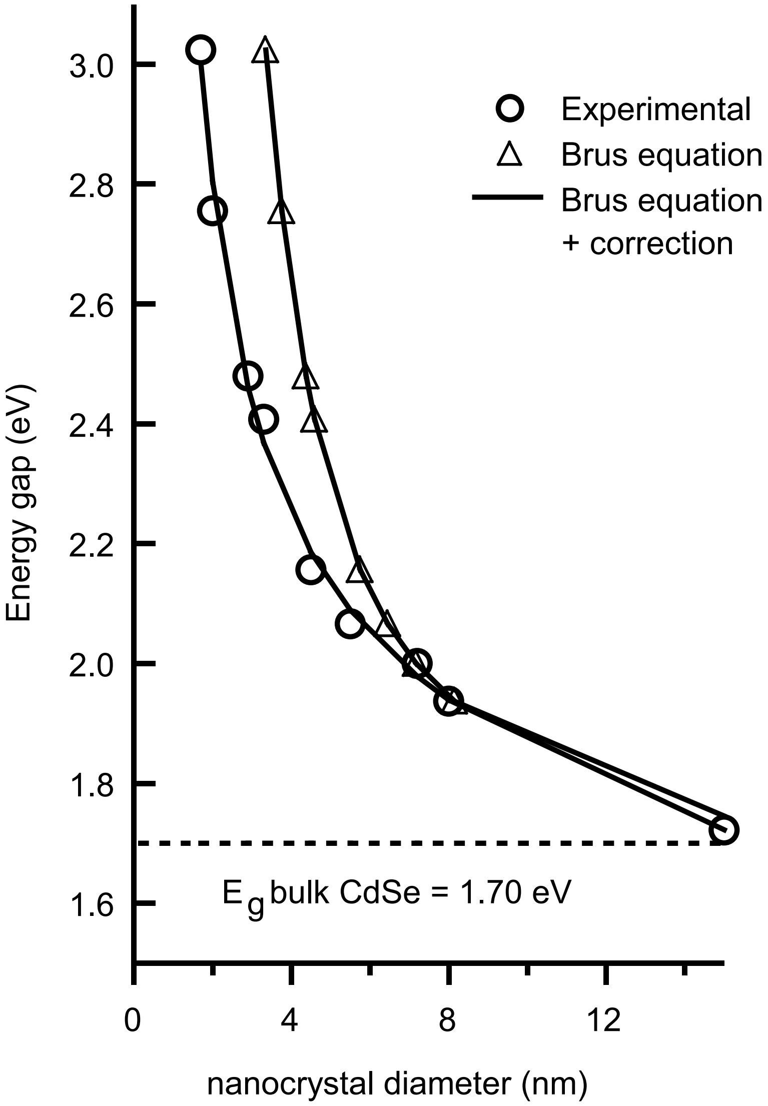

Figure 1.2. Band gap energy of CdSe nanoparticles as a function of particle size

binary nanocrystalline semiconductors, their properties and perspective uses is given in Table 1.1, adapted from Reference [7].

Several approaches are commonly used in the fabrication of such nanometer-sized objects:

- solid state routes: molecular beam epitaxy (MBE), chemical vapor deposition (CVD), laser ablation, sonochemical methods; that can produce localized objects with well-defined shapes and tight control on the properties.
- chemical synthesis: conducted in liquid phase, uses multiple techniques developed for wet chemistry and colloid science, that allow better control of the chemical composition, shape and size. Also colloidal nanocrystals are dispersable in liquid or solid matrices and show advantages when used as building blocks of more complex structures obtained by (self-)asembly.

The refinement of the preparation techniques has been a major goal of the scientific effort in the field, as reviewed by Trinidade et al [7]. The early reports of nanocrystalline preparations produced relatively polydisperse particles, that were produced by kinetically-controlled precipitation (arrested precipitation), in solvents like water, methanol, acetonitrile [8].

The use of a coordinating or capping solvent to prevent the agglomeration of the particle and the formation of a bulk phase yields materials with better crystallinity and narrower size distribution. The system TOP-TOPO has been extensively used and the elements were introduced as highly reactive dimethylated organometallics. The reaction temperature ran around 550 K [9].

An alternative growth route was introduced by several groups [10, 11], where the elements going to form the nanoparticle were introduced as a single source

Table 1.1. Properties of selected semiconductor nanomaterials

Compound	Band gap (eV)	Effective mass		Crystal structure	Lattice parameters (pm)	Applications
		m_e^*	m_h^*			
Group 14 Materials						
Si	1.11 (indirect)	1.58 (m_l)	0.3	diamond	566	
		0.08 (m_t)				
Ge	0.67 (indirect)	0.98 (m_l)	0.52	diamond	543	integrated circuits
		0.19 (m_t)				power electronics
13-15 Materials						
GaP	2.25 (indirect)	0.13	0.67	zinc blende	545	LED
GaAs	1.43	0.07	0.5	zinc blende	565.3	high-speed integrated circuits, displays
GaSb	0.69	0.045	0.39		609.5	thermal imaging devices
InSb	1.28	0.07	0.4	zinc blende	609.5	transistor devices
InSb	0.36	0.028	0.33	zinc blende	609.5	
InSb	0.17	0.0133	0.18		609.5	
12-16 Materials						
CdS	2.53	0.2	5 ∥	wurtzite	a: 413.6	photovoltaic cells
			0.7 ⊥		c: 671.13	
CdSe	1.74	0.13	2.5 ∥	wurtzite	a: 429.9	photovoltaic cells
			0.4 ⊥		c: 701.1	
CdTe	1.5	0.11	0.35	zinc blende	647.6	electrooptic modulators
ZnS	3.8	0.28	> 1∥	wurtzite	a: 318.4	phosphors, infrared windows
			0.5 ⊥		c: 625.7	
ZnS	3.6	0.39		zinc blende	540.6	
ZnSe	2.58	0.17		zinc blende	566.7	infrared windows, LED
ZnTe	2.28	0.15		zinc blende	610.1	
14-16 Materials						
PbS	0.37	0.1	0.1	halite	593.6	infrared sensors
		0.07 (m_l)	0.06 (m_l)			
PbSe	0.26	0.039 (m_t)	0.03 (m_t)	halite	612.4	infrared sensors
		0.24 (m_l)	0.03 (m_l)			
PbTe	0.29	0.02 (m_t)	0.02 (m_t)	halite	646	infrared sensors

precursor, dissolved in the coordinating solvent, e. g., hexadecylamine. The process is conducted in the absence of air but at somewhat lower temperatures (~ 400 K), and avoids the use of highly toxic and volatile dialkyl compounds.

The new materials based on ternary alloys possess unique magnetic and electronic behavior due to the fine tuning of the band gap by the presence of the ternary alloy and the inherent electronic and magnetic properties of the ternary element.

1.2 Doping and characterization of the doping site

In the development of bulk semiconductors, a fundamental role has been played by the possibilities of controlling the physicochemical properties of the material by the regulated incorporation of an impurity, dopant or guest ion. Technologically the most important doped system has been silicon-based materials, in which some of the silicon atoms (about 1 in 10^9 to 1 in 10^5) in the crystals are replaced by atoms of the neighboring groups in the periodic table. In the case where the dopant is from group 15 (P, As), the impurity will introduce an excess of electrons in the crystalline lattice, known as n-doping. If the impurity atom belongs to group 13 (B, Ga), its presence in the lattice will cause an excess of hole carriers, and is known as p-doping. When p- and n-doped layers are laid together in close contact (n-p junction), the application of a voltage making the n-doped layer negative and the p-doped layer positive (forward bias) will cause the flow of current across the junction, while in the reverse case, (reverse bias) current will not flow. This is the principle of the solid-state diode, and it has been the single most important discovery that started the evolution of what today we know as microelectronics. When current flows through the p-n junction, there is a recombination of electrons and holes at the barrier. When the doped material is silicon-based, the energy of the recombination process is released to the crystal lattice as heat, because the electron has to transfer linear momentum to the lattice in order to recombine with the hole (indirect gap), but in materials like GaAs, the electron can recombine without linear momentum transfer (direct semiconductor) and the energy of the recombination is emitted as light. This is the principle of the light emitting diode, another of the fundamental applications in contemporary electronics.

The presence of impurity ions is also important in the study and development of optical materials. It has been known a long time that many gems owe their color to the presence of very small concentration of impurity ions, that sit in the crystal field created by the atoms of the host and participate actively in the processes of light emission and absorption (e. g., ruby owes its red color to the optical transitions of Cr^{3+} inside the crystal of $\alpha-Al_2O_3$). This optical behavior has been further exploited in the development of solid-state lasers (ruby laser, neodymium-yttrium granate), where the amplified light emission originates in transitions between the energy levels of the impurity atoms.

Following the approach and decisive results obtained by the introduction of impurities in bulk semiconductors, great research efforts have been directed towards the introduction of guest or doping ions into nanocrystalline semiconductors, as reviewed by Shim et al. [12]. Doping provides extra possibilities of gaining further control of the properties of nanocrystals by introducing guest ions into the particles. This has been an area of active research for the last fifteen years, given their potential for phosphor, magnetic, and electronic applications. The main difficulty found in their preparation was the tendency of the nanocrsytals to exclude the dopant ions from its lattice at the high temperatures used to grow nanocrystals in the early solvothermal techniques published.

The interest in introducing a paramagnetic ion in a semiconductor nanocrystal is related to their possible application in spintronics [13] and quantum information processing. Efros and coworkers [14] have proposed a voltage-controlled spin valve based on the presence of a single spin in a nanocrystal. The possibility of optical injection of carriers in such a nanocrystal also seems promising for the manipulation and detection of single spins.

A first observation of doping in nanocrystals was made by Bhargava et al. in 1994 [15, 16] for Mn^{2+}-doped nanocrystalline ZnS. The enhanced luminescence observed in the doped nanocrystals was attributed to the replacement of the non-radiative decay processes via surface trap states for the energy transfer from the exciton in the host to the electronic states localized in the impurity ion. These observations suggested the study of the magnetooptical properties of the system, that can be classified as a dilute magnetic semiconductor (DMS). In bulk DMS's there are strong *sp-d* exchange interaction between the band carriers and the transition metal ions. A consequence of this mixing is the appearance of giant magnetooptical effects, but it has been argued that as a result of quantum confinement, the magnitude of the Zeeman splitting can be decreased [17].

When a guest ion is introduced in a crystalline lattice, it can occupy several different locations in the crystalline lattice, as depicted by the structures shown in Figure 1.3. The way in which the properties of the nanoparticles are affected by the presence of the guest is very sensitive to which of these four arrangements dominates.

For neodymium-doped barium fluoride nanoparticles made by reverse microemulsion technique, Bender et al. [18] found the position occupied by the dopant to be dependent on its concentration. For doping up to 10 % molar, the Nd^{3+} replace substitutionally the BaF_2 in the crystal lattice, causing a linear variation of the lattice parameter as a function of the concentration, while at higher levels of guest presence the segregation of a neodymium fluoride phase can be observed from the x-ray diffraction patterns.

Bol and coworkers [19] tried to use various methods of aqueous coprecipitation

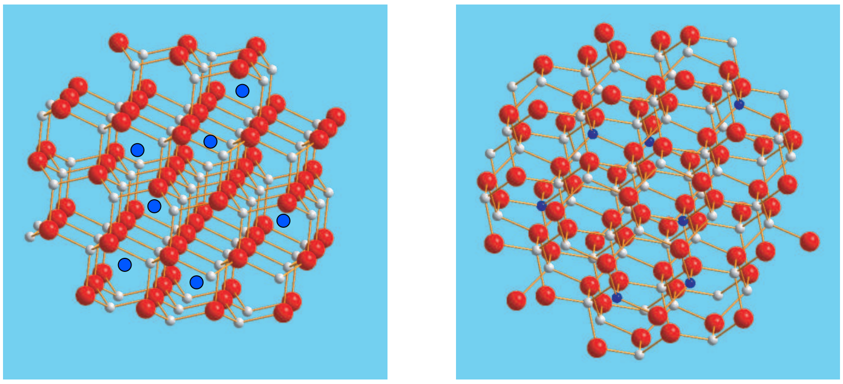

(a) interstitial (b) random substitutional

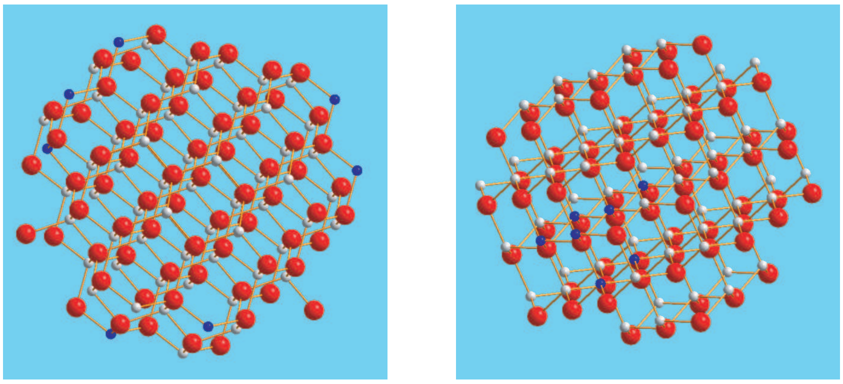

(c) surface segregation (d) phase segregation

Figure 1.3. Possible site distribution of 10% doping in a 2-nm nanoparticle

and inverse micelle to introduce rare earths divalent and trivalent ions in 12-16 semiconductor materials, according to their photoluminescence characterization, they did not succeed in the incorporation of the guest ion into the host lattice. These techniques have as a drawback the low crystallinity of the product and a wide size distribution.

Higher quality materials can be prepared by reactions at higher temperature ($>$ 573 K), but then the possibility of surface of phase segregation is substantially increased. Mikulec et al [20] introduced up to 1% molar of Mn in CdSe grown by a solvothermal procedure, but their experimental results indicate that Mn^{2+} ions reside mostly on or close to the surface of the nanocrystals.

More recently, Norris et al. reported using the same synthetic path to prepare doped nanocrystalline ZnSe:Mn [21]. Their characterization was not limited to photoluminescence studies, but they measured electron spin resonance (EPR) for the Mn^{2+} centers, and concluded from the splitting of the signal that the guest ion was substitutionally replacing Zn inside the host lattice.

While several researchers have probed doped nanocrytalline materials, a systematic study of the controlled displacement of core atoms by guest ions, coupled to analysis of the guest ion site, site symmetry, and valence state have yet to be carried out. Intentionally incorporating a defect ion by random ion displacement of the cation site in the core of a CdSe nanoparticle offers a convenient platform to probe the influence of quantum confinement on the interplay of magnetic and electronic degrees of freedom of the guest ion and host lattice. This study cannot rely in only one type of probe to verify or discard models of doping, given the complexity of the systems involved and the indirect nature of the structural characterization tools available.

1.3 Summary of Chapters

In this dissertation, Chapter 2 explains the synthetic route developed to obtain CdSe:Eu nanocrystals and the results of the preliminary characterization using inductively-coupled plasma atomic emission spectrometry (ICP-AES) for chemical analysis; the study of the morphology and size distribution of the nanocrystals based on transmission electron microscopy (TEM); the optical and vibrational (resonant Raman) spectral characteristics of these materials and the characterization of their mangetic properties using SQUID magnetometry. Chapter 3 shows the results of the powder x-ray diffraction (p-XRD) experiments and concludes that there is evidence of lattice contraction in these materials caused by the introduction of the dopant and of cationic vacancies. The characterization of the oxidation state of the dopant in these systems was first attempted by using x-ray photoelectron spectroscopy, and the results from this experiments are detailed in Chapter 4. Further insight into the oxidation process that occurs during the preparation of CdSe:Eu was sought by the application of ^{151}Eu-Mössbauer spectrometry to these samples. The results of these experiments are shown in Chapter 5. In the next two chapters, a full development of the study based on x-ray absorption spectrometry is exposed. Chapter 6 gives the general experimental and theoretical background for the technique and explains the results derived from the analysis of the near-edge region. Chapter 7 shows the analysis of the extended fine structure of the x-ray absorption, together with the results of the fitting of the spectra to theoretical models. The correlated results of all techniques applied to the study of nanocrystalline CdSe:Eu are summarized as concluding remarks in Chapter 8. Chapter 9 extends the XAFS characterization to nanocrystalline CdSe:Co, and establishes the comparison between a system with no charge imbalance and the defective Eu-doped structures. Chapter 10 shows the application of elastic neutron scattering to the characterization of ZnO:Mn nanocrystals. This model system was selected for convenience, but the results shown are extendable to the characterization of other magnetically doped compound semiconductors. Some suggestions about future developments of the work started with this project are outlined in Chapter 11 and the dissertation closes with general conclusions in Chapter 12. The details of XAFS data processing are collected in an appendix.

Chapter 2

Preparation and preliminary characterization of the materials

2.1 Synthetic route

To achieve random ion displacement of Eu ions into the core of CdSe, CdSe:Eu materials were prepared by a modification of a previously reported growth methodology [22], employing $Li_4[Cd_{10}Se_4(SPh)_{16}]$ as a single source precursor. This strategy has been shown to allow core doping of CdSe by Co(II) [23] and ZnSe by Mn(II) [21]. In a typical batch, 50 g hexadecylamine (HDA) were taken into a three-neck flask connected to a reflux condenser, and heated to 333 K for 8 h under nitrogen, to make sure that all air and water are driven away. To the degassed solvent, 2 g $Li_4[Cd_{10}Se_4(SPh)_{16}]$, prepared according to the procedure described by Dance et al. [24] and the appropriate amount of anhydrous $EuCl_2$ were combined using an airless transfer funnel loaded under nitrogen in a glove-box. Nanoparticle growth was initiated by raising the temperature to 490–510 K ($1 \text{ K} \cdot \text{min}^{-1}$)

and monitored by measuring the uv-vis absorption spectrum on an aliquot taken via septum/syringe and dissolved in chloroform to give a solution of absorbance ~ 0.1 at the maximum corresponding to the first exciton. Figure 2.1 shows how this maximum moves to longer wavelengths as the doped CdSe nanocrystal grows during the synthetic run.

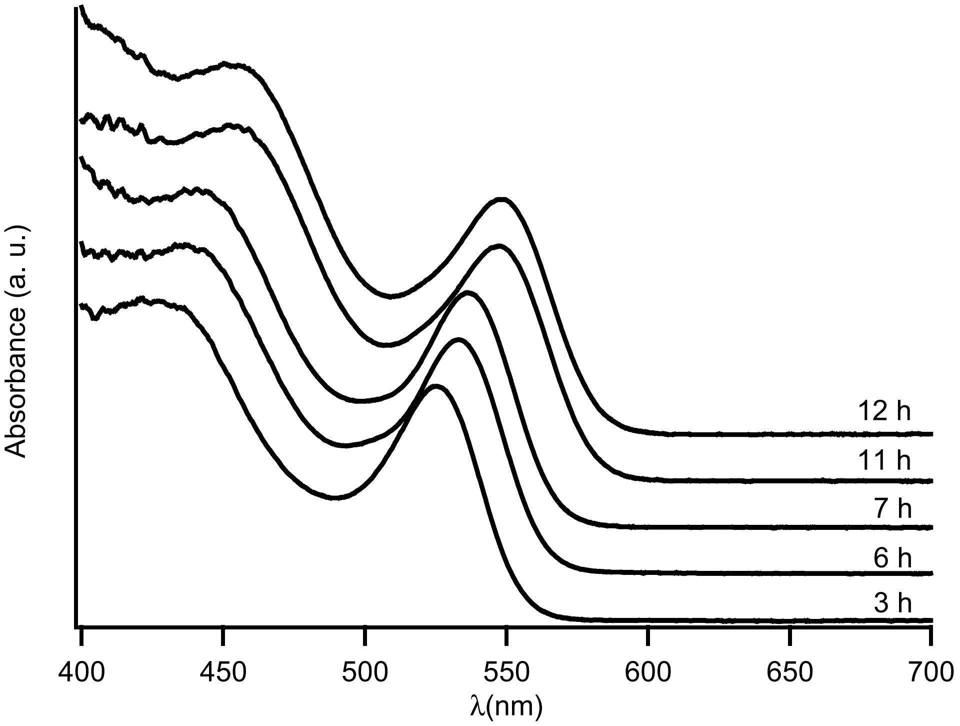

Figure 2.1. Absorption spectra to monitor nanoparticle growth of sample CdSe:Eu, x=0.132 in a 12 h run.

When the position of the maximum reached 550 nm, the reaction was cooled by 20 K and left overnight to narrow the size distribution by annealing the nanocrystals. To isolate the nanocrystals 15 mL portions of the reaction batch were taken via septum/syringe in 30 mL of anhydrous methanol. The crude nanocrystalline mass thus obtained was decanted, the supernatant discarded and the solids suspended in toluene, any undissolved residue was removed by centrifugation and the nanophase was reprecipitated in methanol and isolated by centrifugation. By adjusting the amounts of solvents used for dispersion and reprecipitation, we achieved size-selective precipitation of the nanoparticles, as shown in Figure 2.2 where the FWHM of the first exciton peak decreases from 30 nm to 21 nm in successive precipitation passes.

The cleaning-precipitation process was repeated three times under airless conditions, to make sure that the nanocrystals were completely clean and protected from oxidation. In previous preparative runs we determined that that the isolation of clean CdSe nanocrystals from the solvent where they are grown requires at least three passes, for only after the third step, the nanocrystal mass redispersed in toluene gives an optically clear solution where no further residue is collected after centrifugation. All synthetic batches were cleaned three times by solvent change/precipitation. Further manipulation of the nanocrystals in solution was avoided to minimize the chances of oxidation.

The final product was dried under vacuum for 3 h and collected in the form of a free-flowing powder. Varying the initial stoichiometry of the reaction allows control of the Eu concentration in the final materials.

2.2 Chemical analysis

The chemical analysis for all synthetic runs was conducted by digesting a weighed amount of sample in fuming nitric acid with gentle heating and taking up the moist salts to 100 mL volume with 2% nitric acid. The samples were measured by inductively-coupled plasma atomic emission spectrometry (ICP-AES)

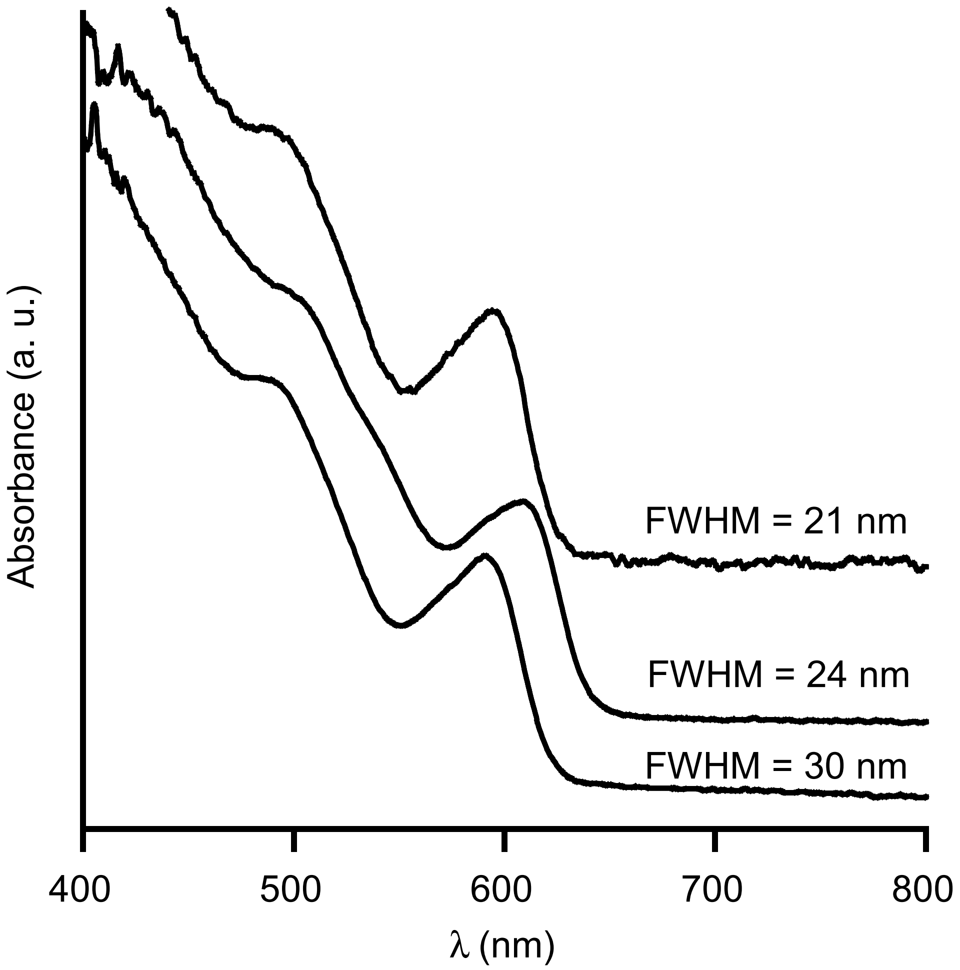

Figure 2.2. Effect of size-selective precipitation of a batch of doped CdSe:Eu nanocrystals x=0.030

in a Thermo- Jarrell Ash IRIS spectrometer. The calibration was achieved by a “two-standards” method, using a 100 μg·mL^{-1} solution prepared from concentrated standard solutions of the analytes (Cd, Eu) commercially available from High Purity Standards, and a blank solution. The analytical lines for each of the elements studied and the error of the determination expressed as percent relative standard deviation (%RSD) are listed in Table 2.1. Table 2.2 summarizes the results of the analysis. The weight percent of Eu was converted to mol fraction x, assuming that every two Eu(III) replace three Cd(II), so that the general formula is $Cd_{1+1.5x}Eu_{2-x}Se$, to account for the vacancy formation due to charge imbalance. Evidence for the III+ oxidation state assignment is provided on Chapter 6.

Table 2.1. Analytical ICP-AES lines

Element	Wavelength (nm)	RSD (%)
Cd	214.4	0.41
	226.5	0.36
Eu	381.9	0.70
	420.5	5.3

Table 2.2. Analytic results Eu-doped CdSe nanocrystals

Sample	Cd (wt/wt %)	Eu (wt/wt %)	Eu mole fraction in CdSe:Eu
1	58.0	0.00	0.000
2	58.2	5.00	0.030
3	47.6	10.3	0.054
4	48.9	21.7	0.132
5	51.3	41.3	0.206

2.3 Optical (absorption and photoluminescence) spectroscopic characterization

The optical absorption spectra of doped and undoped nanocrystals were collected in hexane solution for particles direct from the reaction batch using an Ocean Optics S2000 CCD fiber-optic spectrophotometer, resolution 0.5 nm at the short wavelength end, range 400–800 nm. The photoluminescence was measured in a Hitachi spectrofluorimeter, with an excitation wavelength of 500 nm, bandwidth for excitation and emission of 10 nm. The lifetime of the photoemission was measured by excitation with a nitrogen laser at 337 nm operating at 1 MHz and recording of the luminescence at 600 nm.

The results of the optical measurements are shown in Figures 2.3, 2.4 2.5, 2.8.

There is a slight change in the emission of the nanocrystals caused by the introduction of the dopant, observable as an increase in the asymmetry of the emission band. An attempt at peak deconvolution is shown in Figure 2.7.

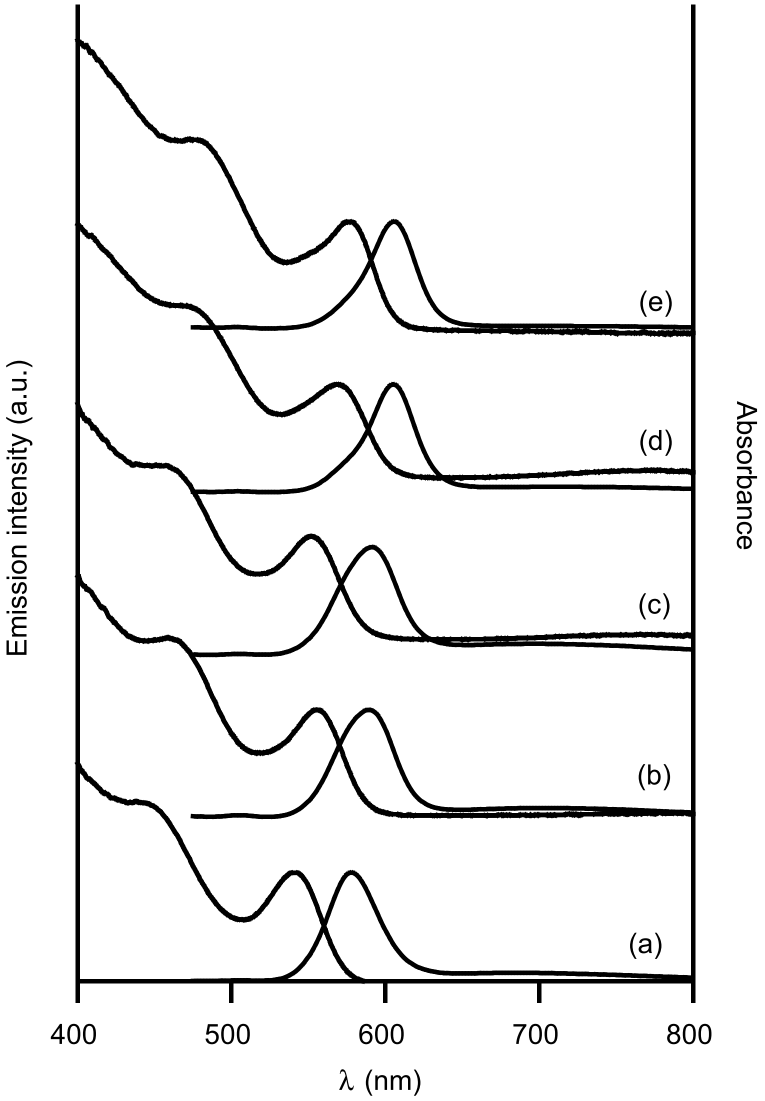

Figure 2.3. Absorption and emission spectroscopy of nanocrystalline CdSe:Eu (a) undoped CdSe (b) x = 0.003, (c) x = 0.030; (d) x = 0.082 , (e) x = 0.136

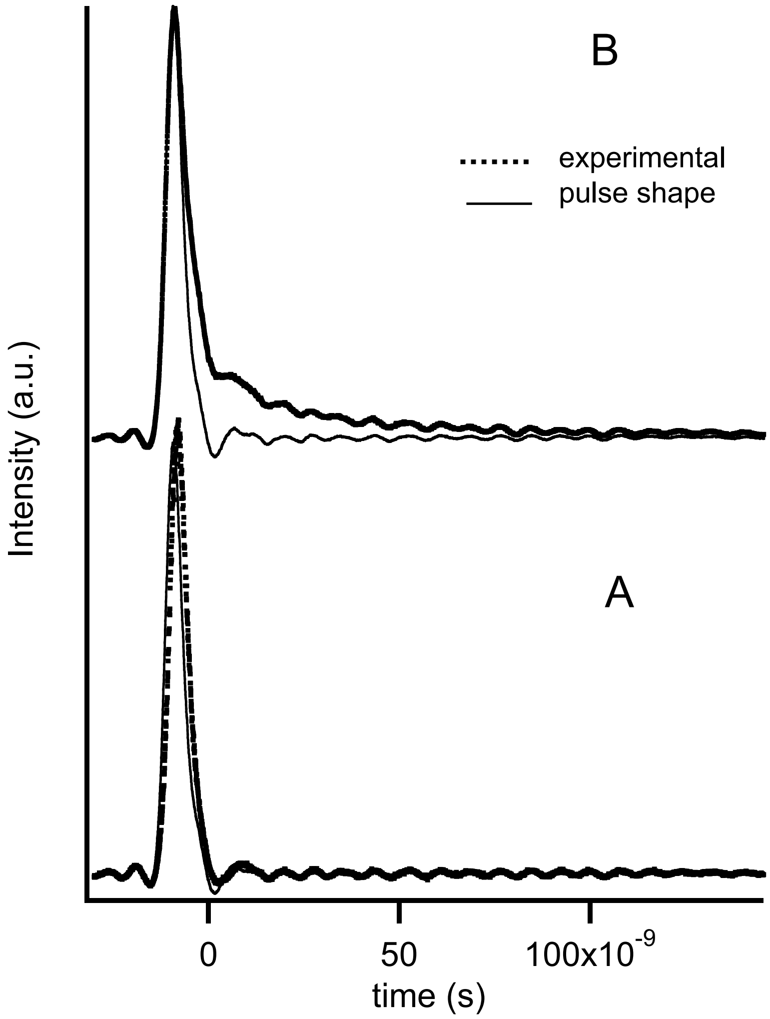

Figure 2.4. Measurement of the emission lifetime of nanocrystalline CdSe:Eu (A) undoped CdSe (B) x = 0.136

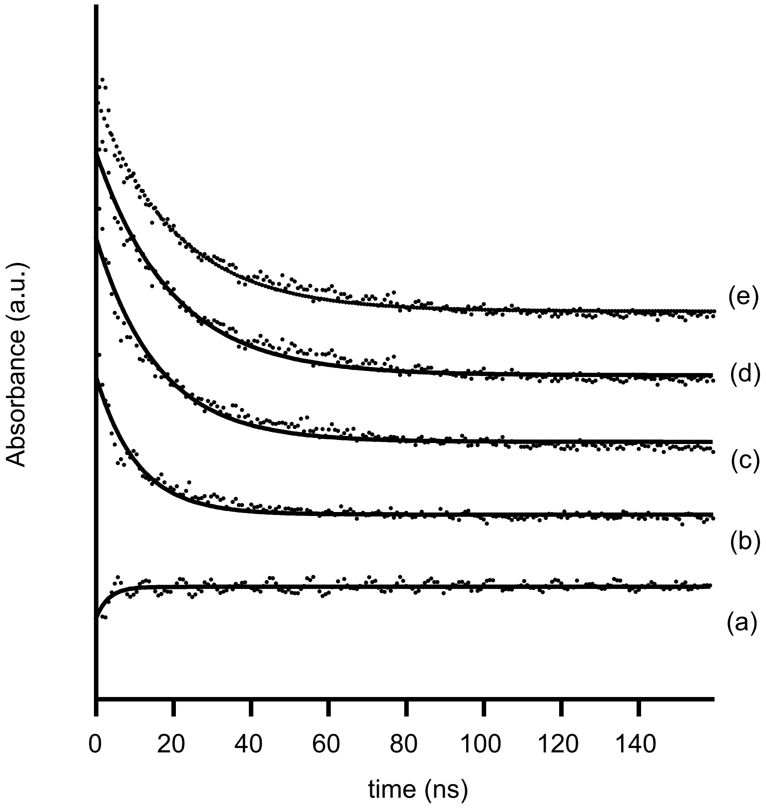

Figure 2.5. Fitting of the emission lifetime of nanocrystalline CdSe:Eu (a) undoped CdSe (b) x = 0.003, (c) x = 0.030; (d) x = 0.082 , (e) x = 0.136

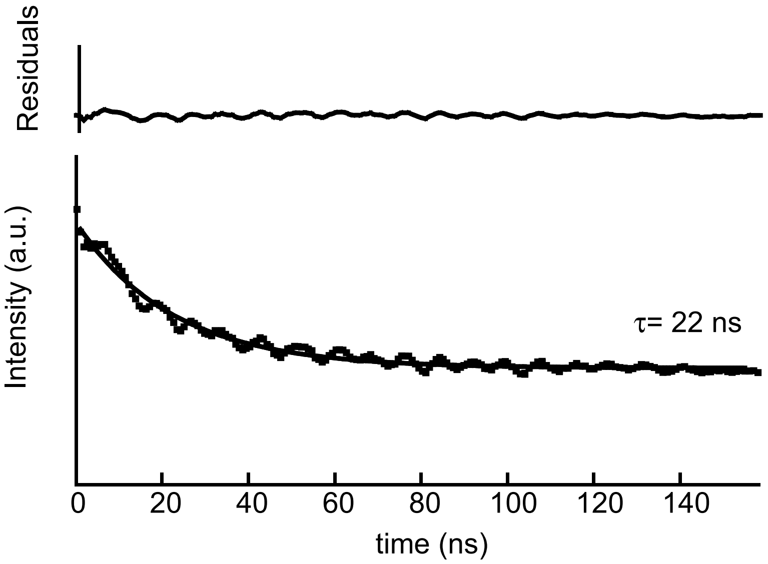

Figure 2.6. Fitting of the of the emission lifetime with a single exponential for the alloy sample CdSe:Eu x = 0.136

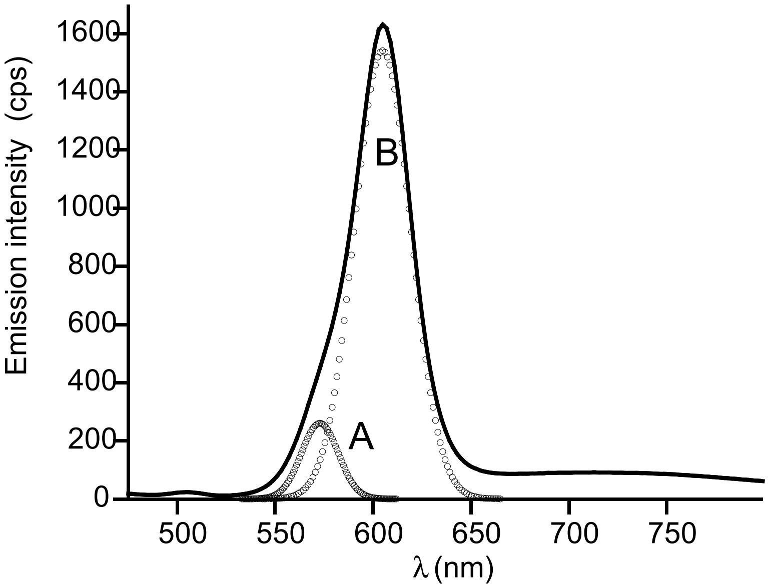

Figure 2.7. Deconvolution of the emission band in the spectrum of CdSe:Eu

Table 2.3. Peak areas obtained by fitting two peaks around the emission maxima of a series of CdSe:Eu alloys

x	A			B			Area A/B	χ^2
	Position (nm)	Width (nm)	Area (a.u.)	Position (nm)	Width (nm)	Area (a.u.)		
0.000	NA	NA	NA	579.44	23.20	37.15	NA	0.1291
0.001	NA	NA	NA	587.3	24.50	40.76	NA	0.1238
0.015	566.4	12.68	3.305	590.8	23.30	38.11	0.087	0.1786
0.039	572.9	13.39	3.791	604.9	20.43	34.40	0.111	0.0509
0.062	574.5	15.38	4.567	605.6	20.30	34.40	0.133	0.0117

The ratio of the areas of peaks A and B calculated for the series of doped samples is shown in Table 2.3. The possibility of measuring the asymmetry by this two-peak fit starts only at x=0.030 and above and the area of the small peak scales up with the concentration of the guest ion, which further suggests that its appearance is a consequence of the presence of the guest.

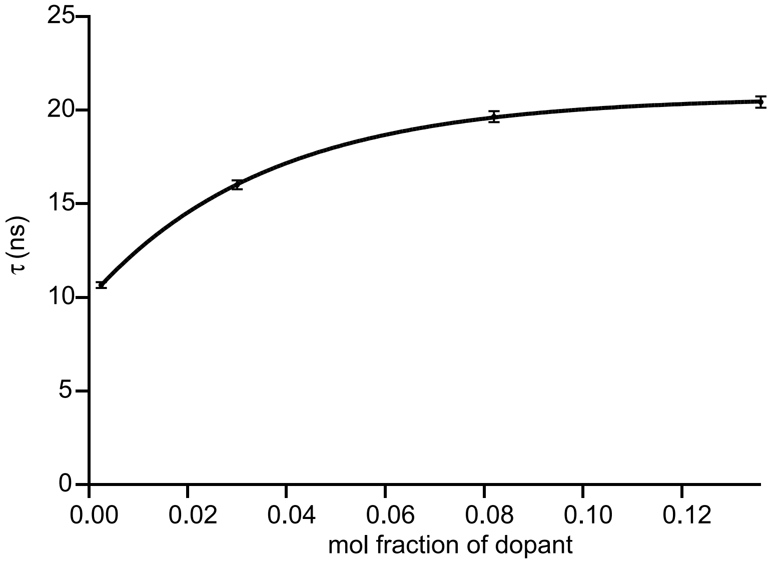

Figure 2.8. Emission lifetime of nanocrystalline CdSe:Eu as a function of the dopant concentration

The measurement of the lifetime also indicates the presence of a long-lived process in the doped samples. The magnitude of τ grows exponentially with the concentration, reaching a plateau at x = 0.08 and $\tau \sim 22$ ns, as shown in Figure 2.8. The luminescence in the undoped samples decays faster than can be measured ($\tau <$ 5 ns) by the experimental setup used. This process is still too short-lived to be attributed to the Eu^{3+} transitions that occur typically in the μs regime. Javier et al. [25] have identified this nanosecond event as a band edge exciton (BEE) decay.

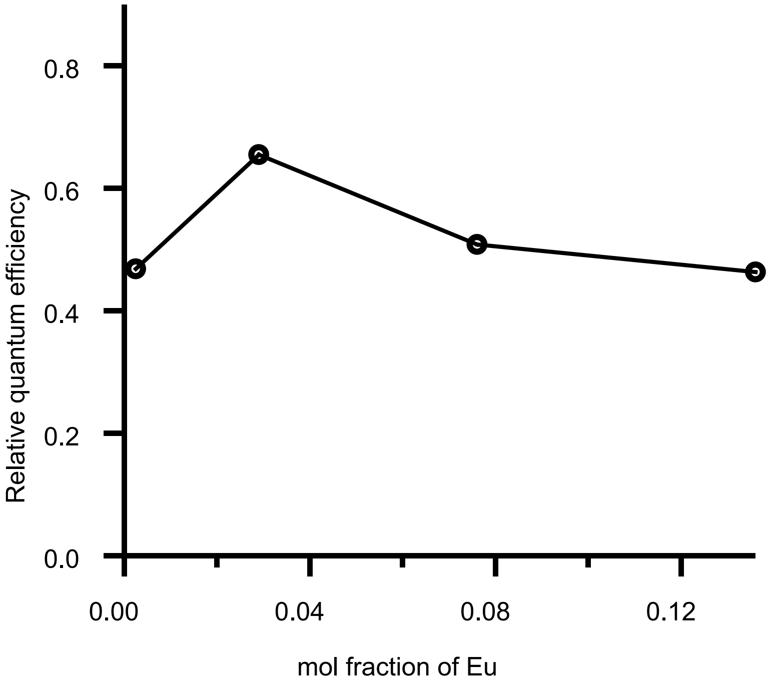

Figure 2.9. Relative quantum efficiency (undoped nc-CdSe = 1.00) of nanocrystalline CdSe:Eu as a function of the dopant concentration

The quantum efficiency of the nanocrystal luminescence for the doped samples was calculated relative to the emission measured from the undoped nc-CdSe synthesized under identical conditions. Its variation with the concentration of guest ion is shown on Figure 2.9. The presence of dopant in the nanoparticles decreases the overall quantum yield, but slightly increases the broad feature at longer wavelengths identified as “deep trap” emission in previous studies of this type of quantum dots [9].

The luminescence of both oxidation states of europium in other compound semiconductor nanocrystalline systems (Eu^{3+} in nc-PtS_2 [26], Eu^{2+}/Eu^{3+} [27, 28]) has been studied. In the work reported by Chen and coworkers [27, 28], nanocrystalline ZnS was doped with Eu^{2+} and the photoluminescence of the material studied as a function of the particle size and oxidation state of the guest ion. They found that emission from Eu^{2+} in that matrix appeared as a broad band centered at 530 nm corresponding to the intraion transition $4f^65d^1 \rightarrow 4f^7$. It disappeared when Eu^{2+} was oxidized to Eu^{3+}, in which case new sharp lines in the florescence appeared around 590, 612, and 695 nm corresponding to the transitions ${}^5D_0 \rightarrow {}^7F_1, {}^5D_0 \rightarrow {}^7F_2$, and ${}^5D_0 \rightarrow {}^7F_4$ respectively. The difference in shape of these transitions is related to the fact that the d^1 electron suffers a very strong electron-phonon coupling in the ZnS lattice, but this effect is practically irrelevant for the “core” f-electrons.

Given the size of our nanoparticles and the value of the energy gap for CdSe, we can expect that the emission from Eu^{2+} to be degenerate with the exciton recombination. We did not observe any of the sharp lines corresponding to Eu^{3+}. If it is present, its luminescence must be completely quenched by non-radiative relaxation of the excited ion to surface or defect states. No further information about the oxidation state of Eu can be derived from this experiment. Still the presence of Eu^{3+} guest ions does change the luminescence from the CdSe, most likely by promoting emission from impurity states induced by the Eu^{3+} inclusion.

A second measurement in a more sophisticated experimental setup was made in order to verify these findings. In this case, a streak camera was used to collect the fluorescence. The measurements were taken using the frequency doubled 1 MHz output of a cavity-dumped R6G dye laser. The dye laser was pumped with the frequency-doubled output of an actively-mode locked Nd:YAG laser. The pulses were about 15 ps in duration, $\sim$15 μW of 320 nm light. The resolution on the streak camera is about 0.5 nm, the temporal jitter is negligible. A Mathematica routine developed by Jennings [29] allows the extraction of the photoluminescence spectrum and the derivation of the lifetimes of the excited states by fitting a double exponential model

$$I = I_0 + A_1 \cdot \exp(-\frac{t}{\tau_1}) + A_2 \cdot \exp(-\frac{t}{\tau_2})$$

to the time-resolved cumulative spectra. The results of these measurements for a sample of nc CdSe:Eu with x=0.071 are shown in Figures 2.10 and 2.11, and the fitting results are listed in Table 2.4. There is an excellent agreement with the data previously measured for the slow event, which is an argument in further support of the two distinct radiation processes for the doped nanocrystal.

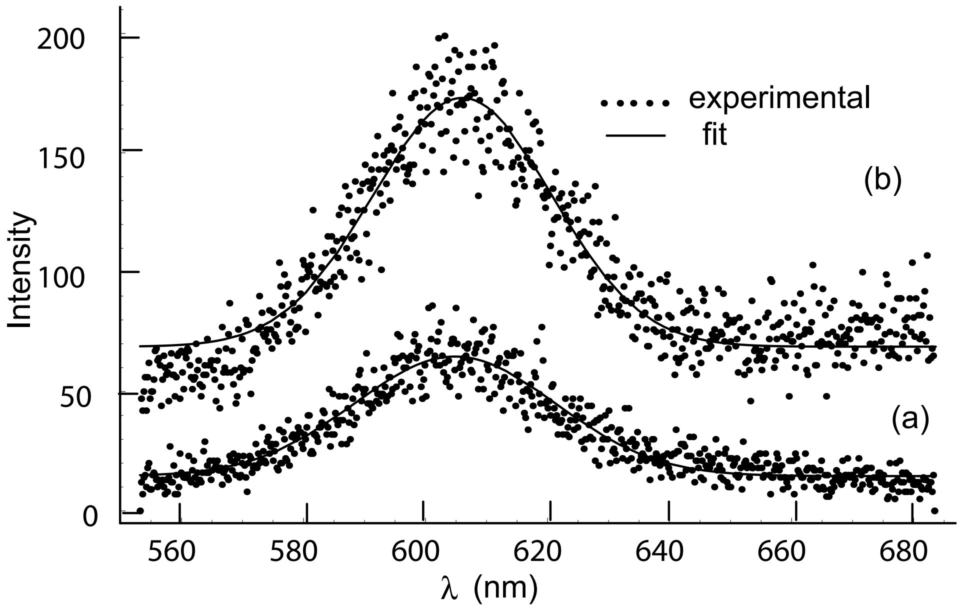

Peak Shift (nm)	1.22042
Error	0.841952
S/N	17

Figure 2.10. Photoluminescence measured in time-resolved system for nc CdSe:Eu, x=0.071 (a) pulse shape; (b) sample photoluminescence

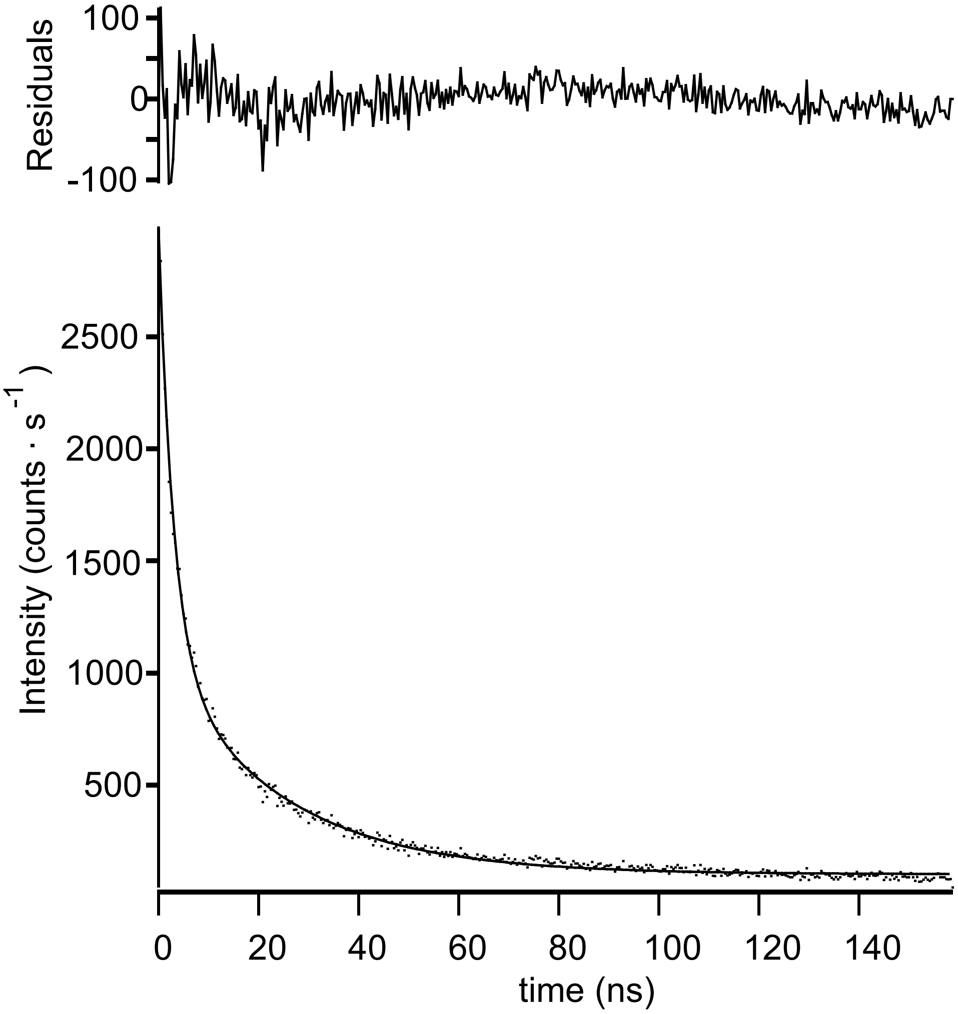

Figure 2.11. Fitting of the lifetime data by a biexponential decay curve for nc CdSe:Eu, x = 0.071

Table 2.4. Numerical results of fitting the lifetime data by a biexponential decay model for nc CdSe:Eu, x = 0.071

	Estimate	Standard error	95% confidence interval	
I_0	101.07	1.96234	97.2115	104.928
A_1	1913.98	19.5868	1875.47	1952.49
τ_1	3.04675	n/a	2.93163	3.17128
A_2	971.57	16.5873	938.955	1004.19
τ_2	24.0688	n/a	23.196	25.0099

2.4 Vibrational (resonant Raman) spectroscopy

The resonant Raman spectra of a series of nanocrystalline CdSe:Eu and of an undoped sample collected with an excitation wavelength of 488 nm of a 10 W Spectra-Physics 2200 Ar ion laser at 5 mW power, a 0.5 m ARC single spectrograph with a diffraction grating of 1800 lines·mm^{-1}, blaze at 500 nm, coupled with a Princeton Instruments CCD array of 512×512 pixels. A holographic notch filter (Kaiser Optical) was used to reject the excitation laser line. A 5-mg sample of the free flowing powder was ground with 2 g of dry KNO_3 and pressed into a 25.4 mm diameter pellet. The spectra were collected in backscattering configuration at 278 K. The spectra are shown in Figure 2.12.

The spectrum of the undoped sample is dominated by the nanocrystals photoluminescence, but still a clear Raman line is observable at 184.6 cm^{-1}. We can assign this vibration to the longitudinal (LO) phonon mode of the CdSe wurtzite-type lattice, as has been previously reported [30]. In the doped samples, the luminescence is totally quenched, as we described above, and besides the LO phonon and its second harmonic at 391.5 cm^{-1}, we can observe new prominent features appearing at 265 and 313 cm^{-1} that are not present in the spectra of the undoped sample. These new vibrations might be the result of reducing the symmetry of the lattice by the introduction of the dopant.

The Raman shift of the LO mode is red-shifted with an increase in the concentration of dopant, as shown in Figure 2.13, what can be interpreted as an effect of the average lattice contraction in the nanoparticles as a result of the increased concentration of the guest.

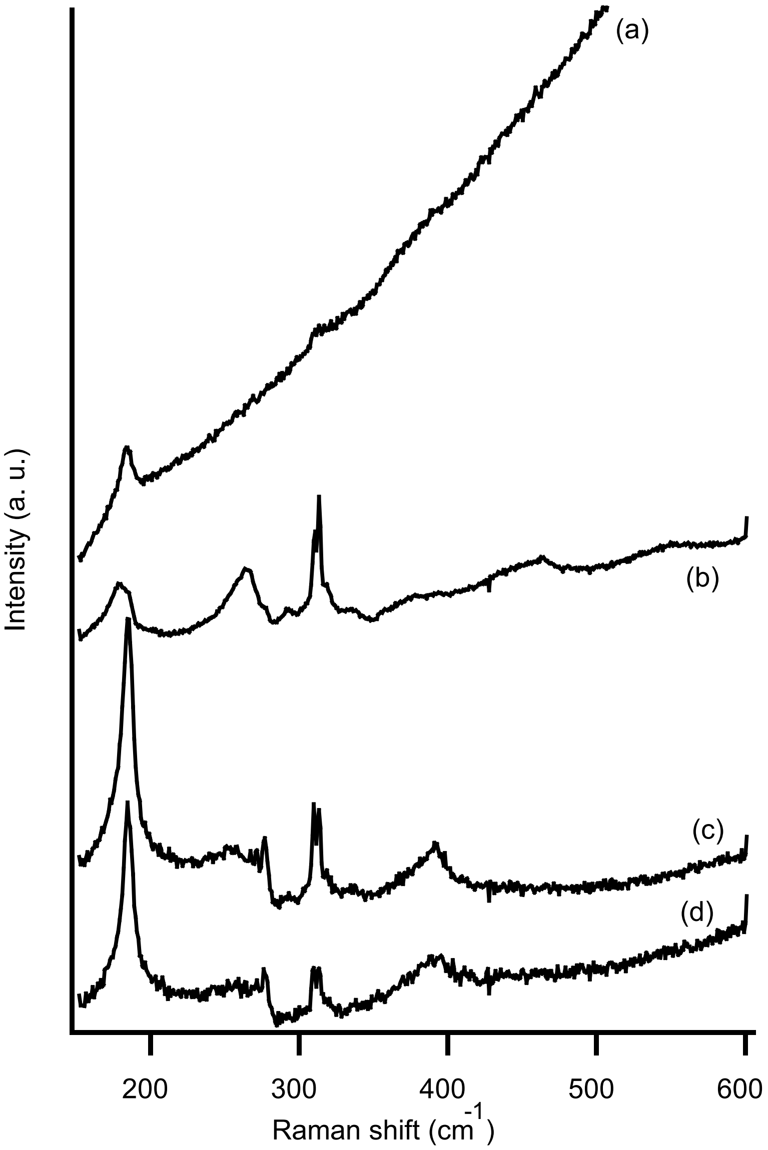

Figure 2.12. Raman spectra of: (a) undoped nc-CdSe; (b) CdSe:Eu x= 0.054, (c) CdSe:Eu x= 0.071, (d) CdSe:Eu x= 0.206 in solid KNO_3 at 298 K

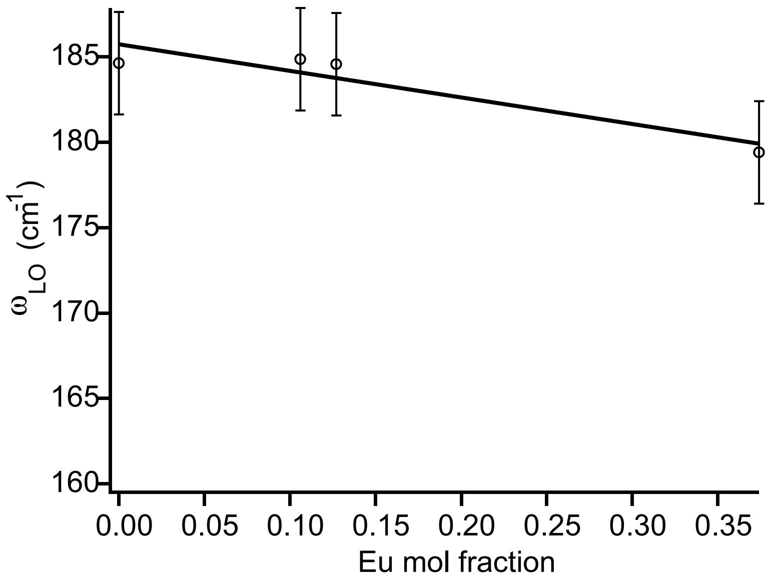

Figure 2.13. Variation of the energy of the LO mode as a function of concentration for nc CdSe:Eu in solid KNO_3 at 298 K

2.5 High-resolution TEM

Micrographs of the samples were obtained on a JEOL 2010 microscope operated at 200 kV in bright field mode. A dilute hexane solution of the nanocrystals was placed on a carbon grid, the excess solution wicked off and the grid was let to dry on air. The size determination and the estimation of the size distribution are based on statistical analysis of up to 100 measurements in each micrograph, as shown in Figure 2.14.

A detail of a single crystallite looking down the $\langle 100 \rangle$ axis is shown in Figure 2.15, together with a model of the nanoparticle simulated with the lattice parameters found from powder-XRD. There is good agreement between the interplanar distance measured in the micrograph (338 pm) and the distance estimated in the simulation (350 pm).

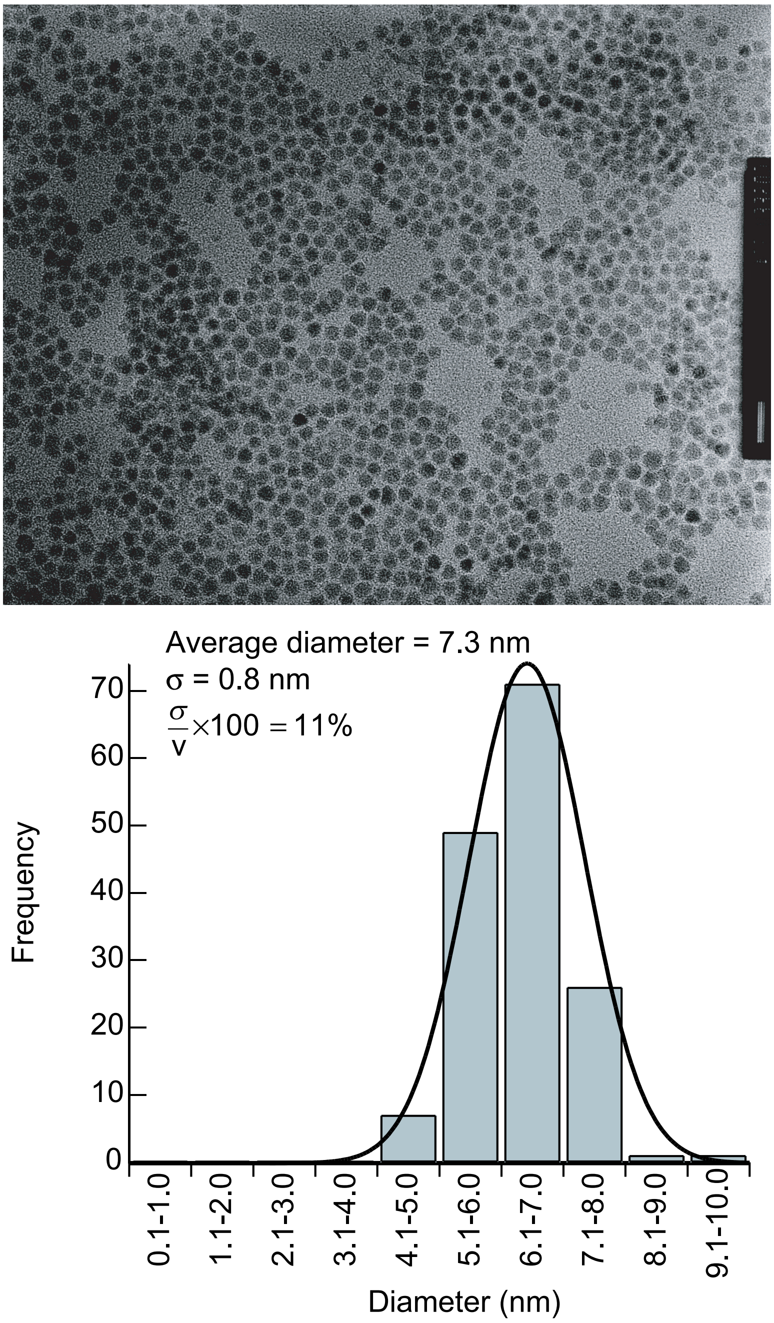

Figure 2.14. TEM micrograph of nanocrystalline CdSe:Eu x = 0.206

As shown in Table 2.5 the size measured from the TEM micrographs and that calculated from the Scherrer broadening in the powder XRD (see Section 3.1) are also in good agreement.

Table 2.5. Comparison of nanocrystal size determination

Sample	diameter by TEM (nm)	Diameter by XRD (nm)
CdSe:Eu x = 0.054	5.6	4.9
CdSe:Eu x = 0.206	7.3	6.9

2.6 SQUID Magnetometry

The direct current magnetic susceptibility of the doped samples was measured in the temperature range between 1.8 and 300 K using a Quantum Design Magnetic Properties Measuring System (MPMS model 1802) provided with a superconducting quantum interference device (SQUID) at magnetic fields up to 7 T.

The temperature dependence of the molar magnetic susceptibility (χ_M) for nanocrystalline CdSe:Eu x = 0.206 and x=0.062 are shown in Figures 2.16 and 2.17.

For CdSe:Eu x = 0.206, the mass of sample used was 0.0680 g, containing 8.37×10^{-5} mol of Eu. The χ_M value measured at 254 K ± 0.5 K of 3.55×10^{-8} $\mathrm{m}^3\cdot$ mol^{-1} corresponds to a magnetic moment of 2.22×10^{-23} $\mathrm{A}\cdot\mathrm{m}^2$ μ given by the equation [31]

$$\mu = \sqrt{\frac{\chi_M \cdot 3 \cdot k_B \cdot T}{\mu_0 \cdot N}}$$

where k_B is Boltzmann constant, N is Avogadro constant and μ_0 is the permeability of vacuum. This value expressed in Bohr magnetons is 2.40 (1 Bohr magneton = 9.27×10^{-24} $\mathrm{A}\cdot\mathrm{m}^2$). But for Eu^{2+}, we have 7 unpaired electrons, giving S = 7/2 and L = 0. If we calculate the corresponding magnetic moment, based on the equation

$$\mu = g\sqrt{S(S+1) + \frac{1}{4}L(L+1)}$$

where g = 2.0023 is the gyromagnetic ratio and the result is expressed in Bohr magnetons , we get μ = 7.94 Bohr magnetons. We can calculate the relative amounts Eu^{2+} and Eu^{3+}, by considering that even if Eu^{3+} theoretically is non-magnetic, the lower excited levels of the ground state manifold are close enough so that at temperatures between 200 – 300 K, they become populated, giving an effective number of magnetons of approximately 3.4 [32]. Since the mol fractions of Eu^{2+} and Eu^{3+} add up to one, we can write

$$(1 - x_{Eu^{3+}}) * 7.94 + (x_{Eu^{3+}}) * 3.40 = 2.40$$

and calculate the mol fraction of Eu^{3+} as 0.88, i.e., 88 % of the Eu atoms are oxidized to Eu^{3+}.

The same calculations applied to nanocrystalline CdSe:Eu x=0.062 alloy gave a magnetic moment equal to 1.23×10^{-8} A·m^2 for a sample containing 9.15×10^{-6} mol of Eu, giving a magnetic moment of 3.02 Bohr magnetons and a 92 % of Eu atom as Eu^{3+}.

These values are in good agreement with the residual amounts (less than 10%) of Eu^{2+} that were detected in later experiments using Mössbauer and XAFS.

The temperature dependence of the susceptibility is shown as a $1/\chi$ vs. T plot in Figures 2.18 and 2.19. The material obeys Curie-Weiss law

$$\chi_M = \frac{C}{T - \Theta_C}$$

down to approximately 70 K and has a Curie temperature of Θ_C = -119.6 K.

The slope of the straight portion of this curve gives an estimate of Curie constant C = 1.3843×10^{-5} K, which can be used to derive the number of atoms of spin magnetic moment S present in the sample, applying the expression derived from the Langevin theory of paramagnetism

$$C = \frac{Ng^2 J(J+1)\mu_0 \mu_B^2}{3k_B}$$

where the symbols have the meaning explained above in this section and assuming a sample volume of 1×10^{-8} m^3 we get the equivalent of 1.35×10^{-4} mol Eu in the sample, where the value from chemical analysis is 1.85×10^{-4} mol Eu. The difference is explained by the partial oxidation of Eu^{2+} to Eu^{3+} and by the practical limitations regarding the estimation of the sample volume.

In the study nanocrystalline ZnS:Eu, Tsujuii and coworkers [33] recently found a qualitatively very similar magnetic behavior caused by the presence of both oxidation states, but they did not report the value of Θ_C or C found in their experiment.

As a result of the magnetic measurements we have been able to establish that significant oxidation must have occurred in our samples and also we have been able to estimate quantitatively the extent of the oxidation process.

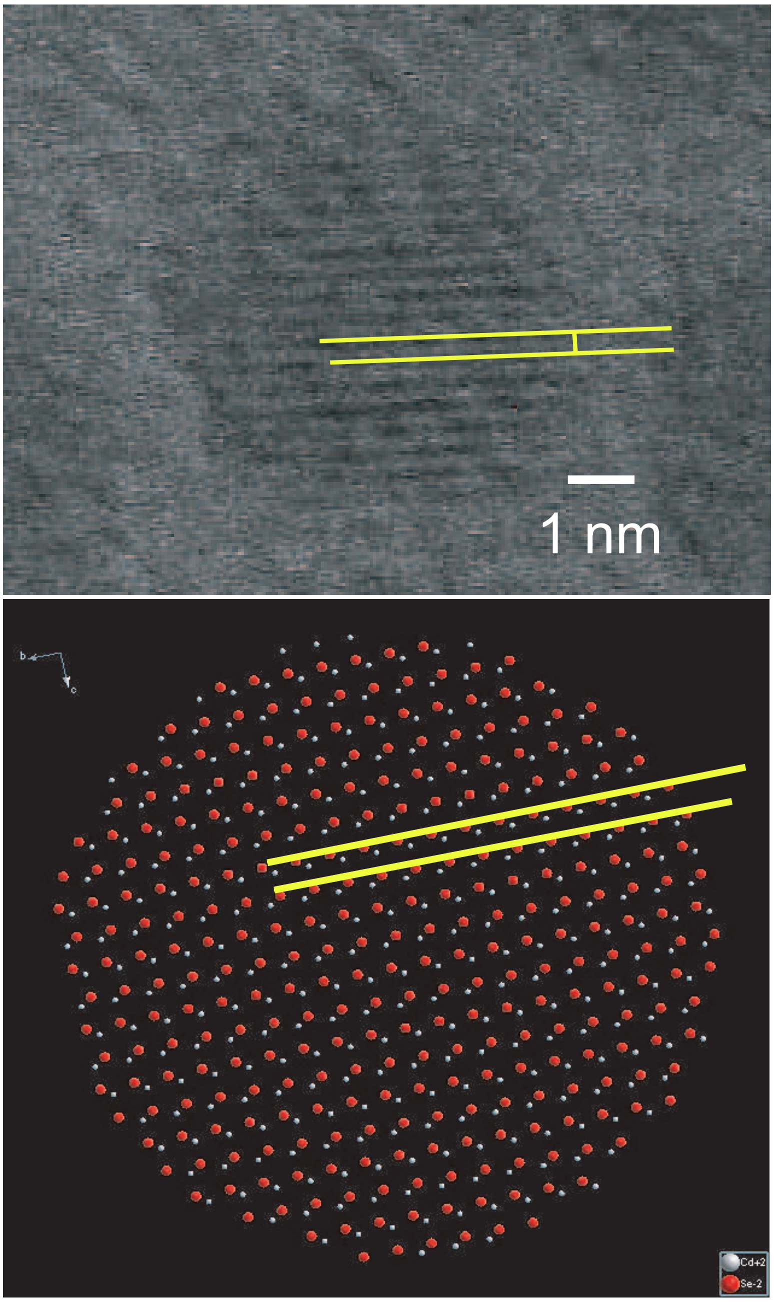

Figure 2.15. Details of a single CdSe:Eu x = 0.206 crystallite and model of the nanoparticle

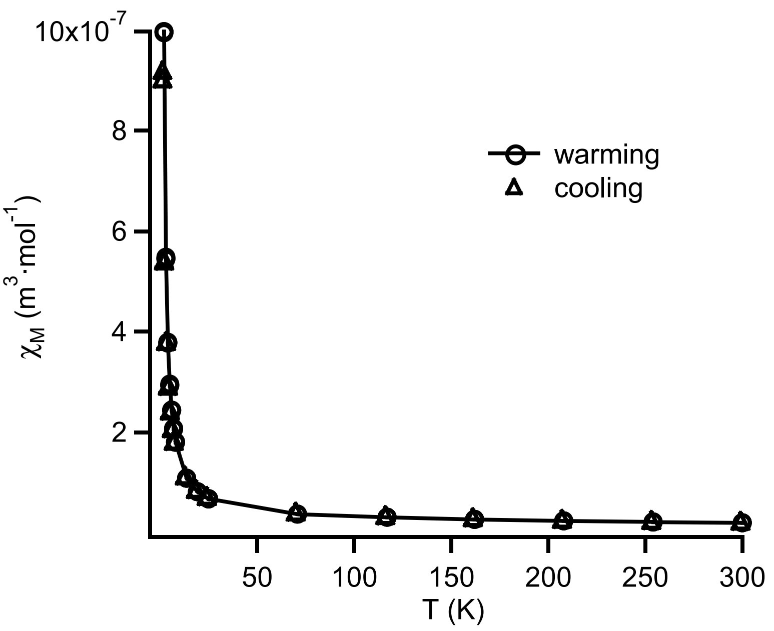

Figure 2.16. Magnetometry of nanocrystalline CdSe:Eu x = 0.206

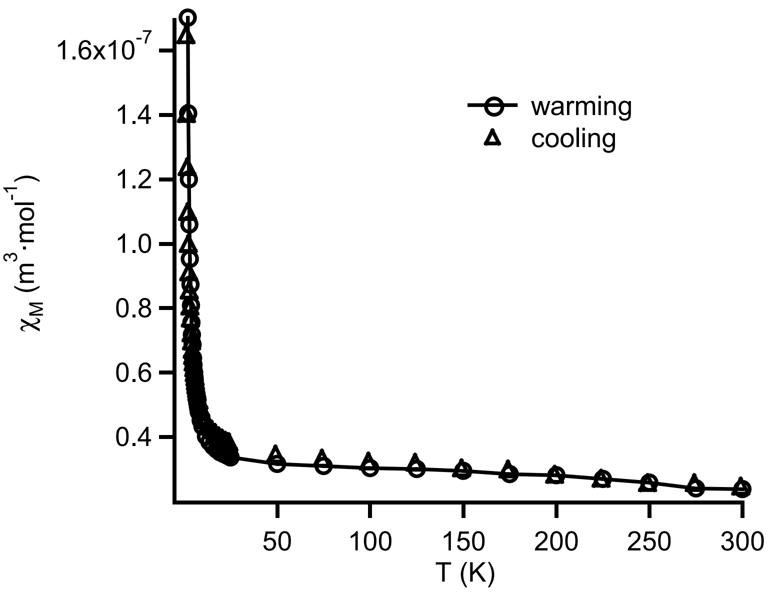

Figure 2.17. Magnetometry of nanocrystalline CdSe:Eu x = 0.062

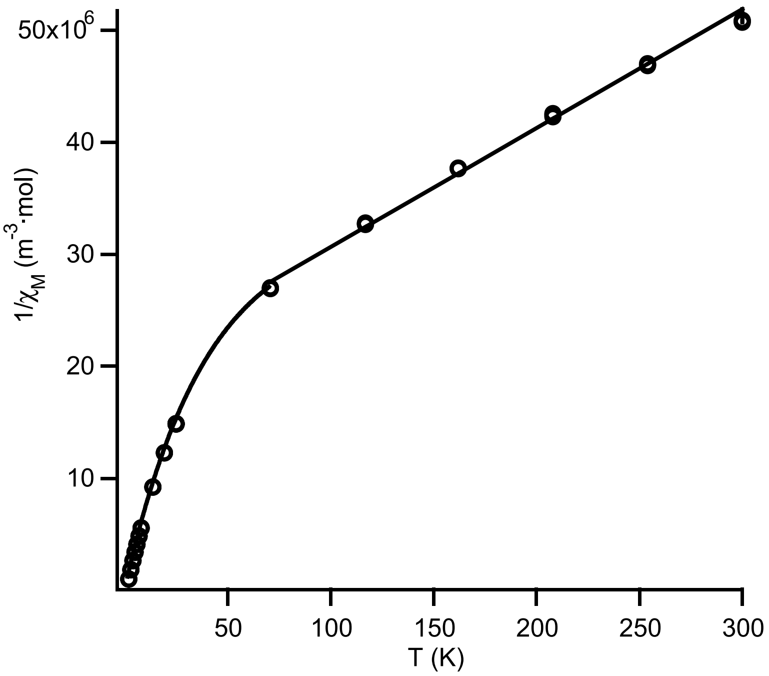

Figure 2.18. Inverse susceptibility as a function of temperature for CdSe:Eu x = 0.206

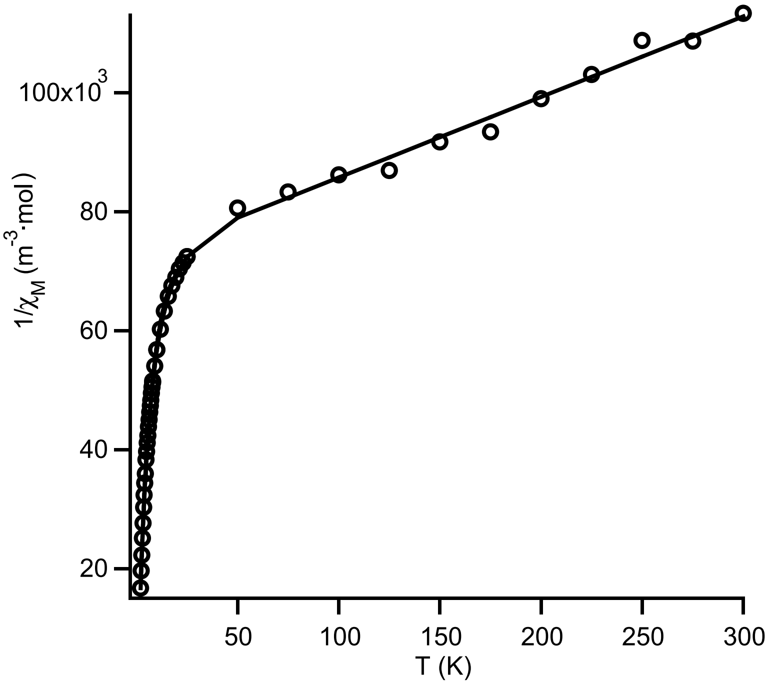

Figure 2.19. Inverse susceptibility as a function of temperature for CdSe:Eu x = 0.062

Chapter 3

Phase characterization of the doped nanocrystalls

3.1 Powder x-ray diffraction

The incorporation of even a small amount of dopant into the guest crystal has generally a measurable effect on the lattice parameters, since the guest can be regarded as point defects that will invariably affect the long-range order present in the crystal. Powder x-ray diffraction provides an efficient probe for study doping in nanomaterials. The crystallinity of the nanoparticles is somewhere between a bulk crystal and a disordered solid, and for that reason, the peaks corresponding to different family of planes in the nanocrystal appear fairly broadened in the diffractogram. This effect is known as Scherrer broadening and allows us to estimate the diameters of the nanoparticles by measuring the FWHM of the reflections and applying Scherrer's formula [34]:

$$\mathrm{L} = \frac{K\lambda}{B\ \sin\ \theta}$$

where K is the Scherrer constant,

$$K = 2\sqrt{\frac{ln\ 2}{\pi}} = 0.93947$$

L is the diameter of the nanoparticle, B is one-half of the breadth of the diffracted beam (in radians), λ is the wavelength, and θ the Bragg angle. The calculated values agree well with the size of the nanoparticles measured by TEM, as shown previously on Table 2.5. For example, in the case of CdSe:Eu x = 0.206, based on the $\langle 110 \rangle$ reflection centered at 2θ 43.2$^{\mathrm{o}}$ we get B = 0.0223577 radian, L = 6.9 nm, for a TEM average of 7.3 nm. These two estimations of the particle size are based in different physical principles and sample the measured parameter in very different ways. TEM sizes are derived from manually measuring a 2-dimensional projection of several hundred individual crystallites and the size distribution of the sample is reflected in the relative standard deviation of the results (in this case $\sim$ 10 % The diffraction measurement averages over a large number of nanoparticles ($\sim$ Avogadro's number) and the broadening effect appears as a contribution of both the finite particle size and the distribution of sizes and shapes of the individual crystallites. For the level of uncertainty associated with these estimations, caused by both experimental error and the natural distribution of sizes in the samples, the difference found is not significant.

To measure the lattice parameters, samples of $\sim$ 0.2 g of the nanomaterials as free-flowing powders were placed on the stage of a Bruker AXS D8 diffractometer and their diffractograms recorded between $2\theta = 10 - 60^{\mathrm{o}}$ using unfiltered Cu- K$_\alpha$ radiation. Silicon powder was added as an internal standard.

Nanocrystalline CdSe typically adopts a wurtzite-type structure, although a pressure-induced phase transition to the NaCl lattice has been observed [27]. Figure 3.1 shows a series of powder diffractograms exhibiting wurtzite-type structure at all doping levels.

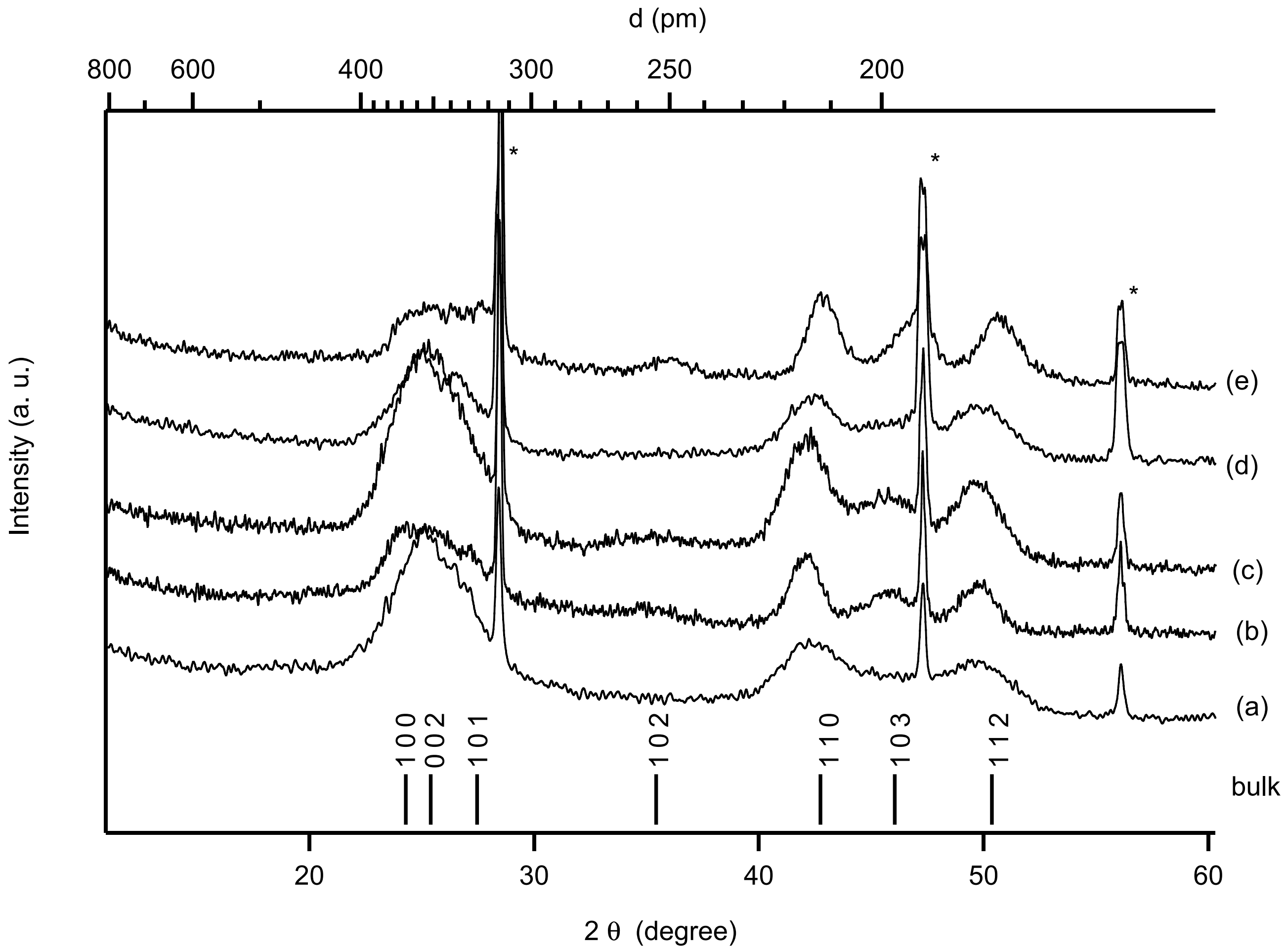

Figure 3.1. Powder diffractograms of CdSe:Eu alloys: (a) undoped CdSe; (b) x = 0.030; (c) x = 0.054; (d) 0.132; (e) x = 0.206. The peaks marked “*” correspond to the Si internal standard

The intensity of the individual reflections in the region $2\theta = 20 - 30^o$, <100>, <002> and <101>is different from what would be observed in a bulk wurtzite-type sample of CdSe, reflecting the variation in the coherent diffraction length in different directions that happens as a consequence of non-spherical shape of the nanocrystals.

The intensity and broadening of the <103> reflection has been observed to be particularly sensitive to the presence of stacking faults along the <102> direction [9]. We effectively observe an increase in the intensity of this peak as the concentration of dopant is increased, what might suggest the reduction of this type of defect in the particles with higher guest ion concentration.

The crystallinity of the samples can be also confirmed by inspection of the TEM. Figure 2.14 shows a representative image of an individual CdSe:Eu x = 0.206 nanocrystal looking down the <100> direction that exhibits lattice fringes consistent with the assignment of a highly crystalline wurtzite structure. The observation of wurtzite geometry is surprising, since pure Eu-Se exhibits either a cubic NaCl-type structure for EuSe with Eu in the 2+ oxidation state or an orthorhombic Sc_2S_3-type structure, which constitutes a superstructure of the NaCl-type lattice, for Eu_2Se_3 with Eu in the 3+ oxidation state. Tetrahedral site occupation for f-elements is rarely observed, since the octahedral environment around the Eu ion tends to stabilize the f-element crystal field. This would suggest significant strain may arise in the lattice around the Eu ions, and may limit the stability of Eu ions that migrate to the nanomaterial surface.

If Eu^{3+} is present, that will also induce the presence of Cd vacancies to accommodate for the charge imbalance (2 Eu^{3+} are equivalent to 3 Cd^{2+}), that can further distort the lattice by generation of glide plane defects. In order to achieve

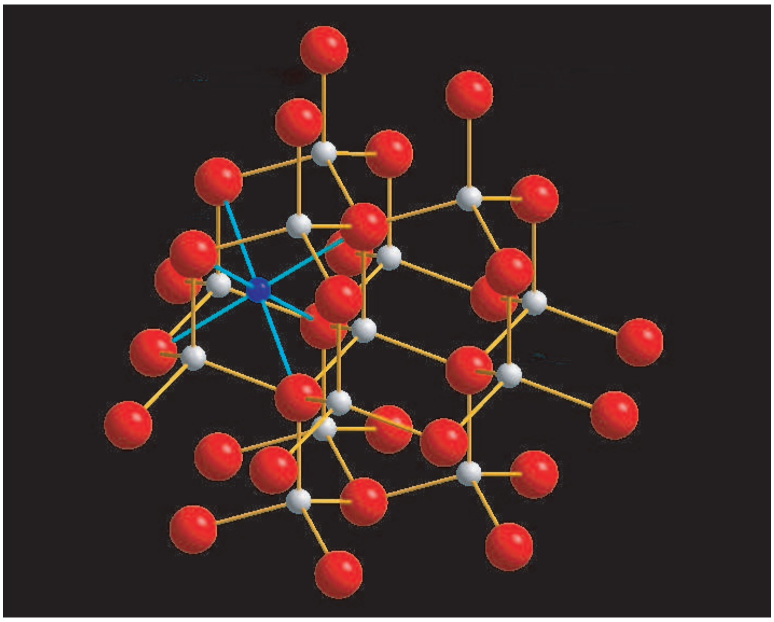

Figure 3.2. Schematic representation of Eu atom sitting on an octahedral hole in the wurtzite-type CdSe lattice.

coordination N = 6, Eu(III) can sit in an octahedral site, as shown schematically in Figure 3.2.

The substantial defectiveness of the crystalline lattice introduced by the presence of the guest ion is furthermore evidenced by the great distortion of the relative intensities of the Bragg reflections when compared to the undoped materials. In Figure 3.1 it is evident that the relative intensity of the three reflections corresponding to the largest interplanar distances drops very significantly as the concentration of guest ion is increased. In later chapters we will discuss that this loss of long-range order is congruent with the model proposed to explain the structure of the CdSe:Eu alloys.

3.2 Substitutional doping: Vegard's Law behavior

The introduction of cationic defects iinto the Cd sites of the wurtzite-type CdSe lattice, causes a measurable change in the lattice parameters. This allows the use of a Vegards law analysis, an empirical law that relates the statistical substitution of a guest into the host lattice with the experimentally observed degree of lattice change with increasing defect concentration. Statistical substitution into a lattice site is predicted to lead to a lattice contraction for smaller ions and vacancies, and a lattice expansion for larger ions.

In order to measure accurately the lattice parameters in the nanocrytalline samples, the diffractograms were shifted so that the Si (220) reflection appears at $2\theta = 47.30$ degree and the broad (110) and (112) reflections were fitted with a Gaussian function from which their position and width were derived. Two examples of the fitting are shown on Figure 3.3. The shapes and FWHM of the diffraction peaks suggests that for these samples, grown under identical conditions, the presence of dopant contributes to a higher crystallinity of the quantum dots.

The lattice parameters were then calculated using the Bragg equation

$$d = \frac{\lambda}{2sin\theta}$$

with $\lambda = 154.089$ pm for Cu-K$_\alpha$ radiation, and the formula for the hexagonal crystal system [35]:

$$\frac{1}{d_{hkl}^2} = \frac{4\,(h^2 + hk + k^2)}{3a^2} + \frac{l^2}{c^2}$$

The (100) and (002) reflections in these materials appear too broadened and unresolved, and for that reason they were not fitted or used in the calculation of the parameters, in spite of the fact that there is a significant advantage in

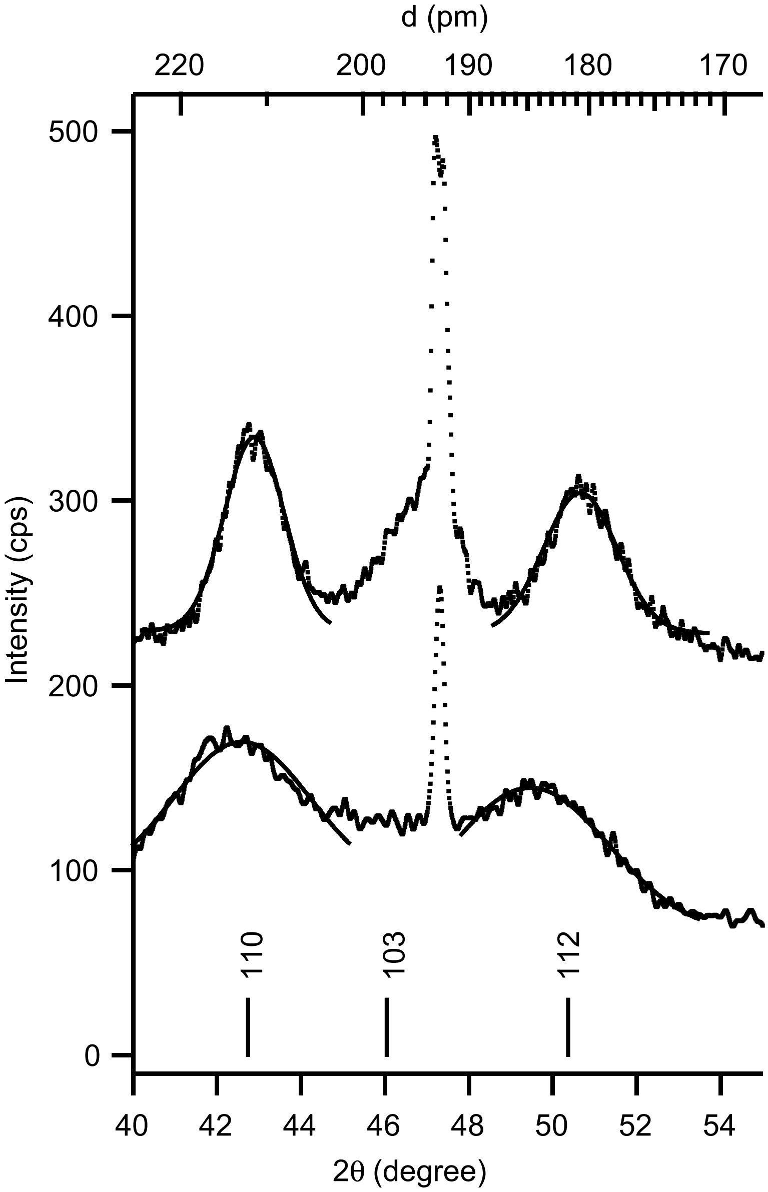

Figure 3.3. Details of the fitting of reflections (110) and (112) for two nanocrystalline samples: (a) undoped nc-CdSe, (b) CdSe:Eu for x=0.206

using such reflections, for the measurement of their shift allows the independent determination of the parameters [a for (100) and c for (002)], whereas the shifts of the reflections more amenable for fitting and calculation are dependent on the change of both parameters.

To check the accuracy of this lattice parameter determination, we ran a simulation based on the Rietveld method of the diffractogram corresponding to the sample with x=0.054, using EXPGUI [36] interface to the GSAS suite of programs [37]. Because of the much lower signal-to-noise ratio present in nanocrystalline samples, it is not feasible to perform a full Rietveld refinement. The result of the fitting are shown in Figure 3.4 and in the parameters derived are compared with some of the values calculated by simple Gaussian fitting in Table 3.1.

Table 3.1. Parameters derived from Rietveld refinement of the powder diffractogram for CdSe:Eu x = 0.054

Cell parameters	Rietveld	Gaussian
a (pm)	422.4	428.1
c (pm)	711.0	714.4
Nanocrystallite size (nm)	6.2 ±0.9	5.7±0.9

The peak profile parameters were floated in the fit and a pseudo-Voigt function profile was used, and tested with different values of the Lorentzian broadening X, defined as a function of the uncertainty in the interplanar distance calculated for the reflections:

$$X = \frac{\Delta d}{d^2}$$

The best fit was obtained for X = 137, from which the size of the crystallites can be calculated by the formula [37]

$$p = \frac{18000K\lambda}{\pi X}$$

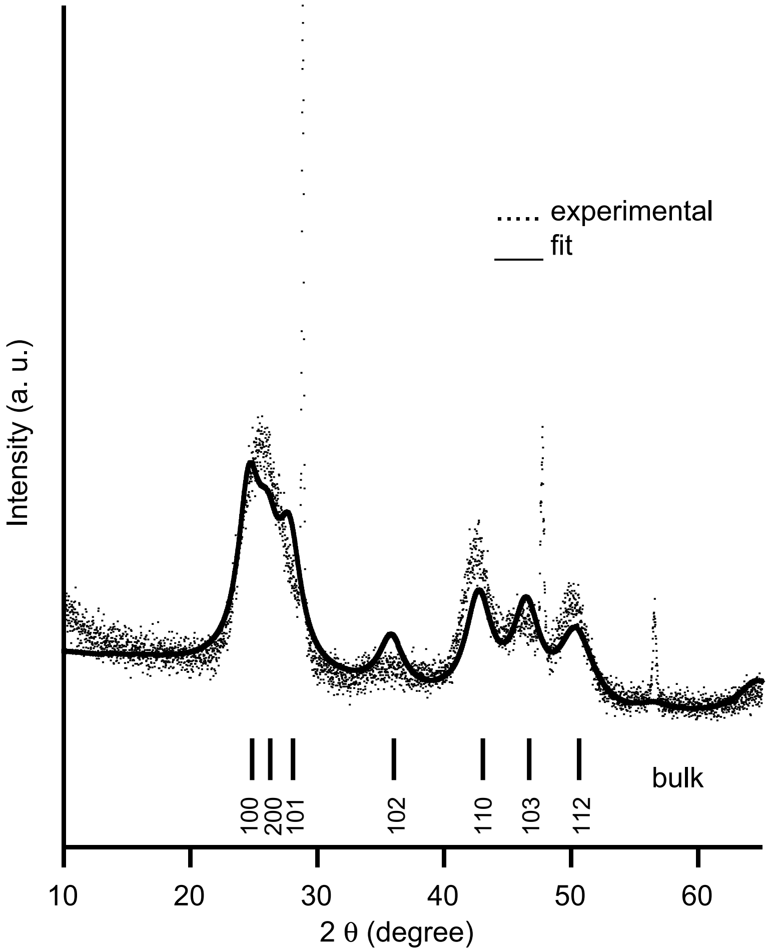

Figure 3.4. Rietveld refinement of the powder diffractogram for CdSe:Eu x = 0.054

where K and λ have the same meaning and value shown in the explanation of Scherrer broadening in Section 3.1. The results of the fit are shown on Table 3.1, and compared with the results derived for the crystallite size by TEM.

The very large Scherrer broadening observable in these samples and their lowered long-range order diminish the usefulness of such an approach, even if the parameters derived are in good agreement with those calculated by simple fitting of the Gaussian shapes to the Bragg reflections.

The shift in the lattice parameter a in Figure 1B shows a lattice contraction of approximately 6 % as the Eu ion concentration in the doped material increases from 0.030 to 0.206 mole fraction. This is clearly seen as a movement of the (110) reflection toward higher 2θ in the powder diffractogram shown in Figure 3.1. The observation of a linear contraction with increasing Eu concentration is in accord with the predictions for Vegards law behavior, suggesting a distribution of defects that occurs at the lattice sites situated both in the core and on the surface through a purely statistical process, and not isolation of the defect ion only at the surface sites through an ion-migration pathway, as previously observed. [38, 39].

Prediction of strain and site occupation of a guest ion in a host lattice requires comparison of the ionic radii in similar coordination environments. This presents a problem for estimation of the lattice change for substitution of the Cd center by the Eu guest ion in a wurtzite lattice, since the coordination environment of Eu(III) is mostly octahedral. are not reported. Lattice mismatch and variance in coordination number have been seen for Mn(II) doping of bulk crystals of II-VI materials, where doping levels in excess of 40% have been observed with a smaller lattice contraction than predicted [40]. An indirect estimation of the lattice mismatch for the Eu ion can be achieved by comparison of the standard ionic radii for the Eu and Cd ions in a NaCl lattice, in which each element is six coordinate. According to the standard reported data for ionic radii [41], the effective ionic radius for Eu(II) is larger than Cd(II) (117 pm vs 95 pm) and an expansion of the lattice should be expected by substitution; however, replacement of Cd(II) by Eu(III) (95 pm vs 95 pm) would leave the lattice unchanged. The observation of a 6% lattice contraction in the XRD data with increasing concentration suggests that Eu(II) is not likely to be the substituent ion, due to the observation of lattice contraction. The difference in contraction relative to the ionic radii arises from the coordination difference between the empirically compared NaCl and experimentally observed wurtzite crystalline lattice and vacancies in the lattice which contract the average spacing of the ensemble. To further analyze the shift; the oxidation state of the Eu must be identified.

A plot of the *a* and *c* parameters of the crystalline lattices vs. the level of doping derived from ICP-AE [Figure 3.5B] shows a linear dependency, confirming random ion substitutional doping with an ion of radius smaller than that of Cd^{2+}. This is an indication that the doping species might be Eu^{3+} rather than Eu^{2+}, based on the standard values of ionic radius reported for these ions (According to the standard reported data for ionic radii [41], the effective ionic radius for $Eu^{2+}=$ 117 pm, $Eu^{3+}=$ 95 pm, Cd^{2+} = 95 pm). [41]. Since the table values for Eu^{3+} and Cd^{2+} = 95 pm are the same, we could expect no change in the lattice parameters on substitution. The observed change can be explained taking into account that Eu goes preferentially to the octahedral holes, and that simultaneously Cd vacancies are created for charge compensation. These combined effects bring about the observed distortion of the unit cell. Preliminary studies by x-ray absorption (XAFS) verified that the oxidation state of europium in our material was 3+ and

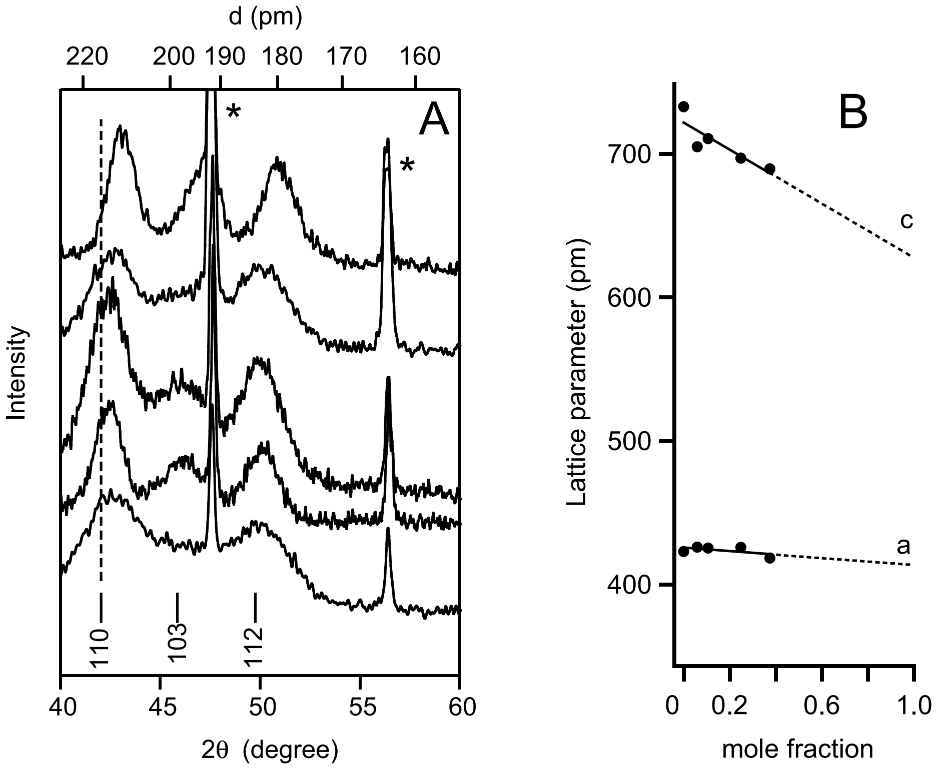

Figure 3.5. (A) Variation in the position of the p-XRD reflections for a series of CdSe:Eu nanocrystals. The vertical line along the abscisa corresponding to the (110) reflection is a guide for the eye. The intense crystalline reflections marked * correspond to the Si internal standard used for d-spacing calibration. The bars right above the abscissa axis indicate the position and Miller indices of bulk CdSe reflections. (a) undoped CdSe; (b) x = 0.030; (c) x = 0.054; (d) 0.132; (e) x = 0.206. (B) The variation of the lattice parameters *a* and *c* derived from the shifts shown in (A)

the more detailed study by Mössbauer spectrometry and XAFS give satisfactory account about the oxidation state and the presence of defective lattice in these materials.

Chapter 4

Chemical composition and oxidation state of the doped nanocrystals by XPS

4.1 Introduction

The changes introduced by doping ions in nanocrystalline materials are necessarily related to the nature and local structure of the impurity centers. The remarkable influence in the physical properties of the quantum dot can be sought in the lowering of the symmetry of the crystalline system, distortions in the crystal field of the host lattice, and strong mixing (hybridization) of the electronic states of the guest ion and the host lattice.

An important set of tools for the characterization of the local structure and chemical environment around the guest ions has been the so called core electron spectroscopies. They allow the investigation of the nature of the electronic states closest to atomic cores as opposed to the study of the valence electronic states.

In the XPS experiment, the sample is irradiated with a beam of monochromatic x-rays, most commonly Mg K_α at 1253.6 eV or Al K_α at 1486.7 eV from an x-ray tube source. If the energy of the photons ($h\nu$) is high enough, core electrons in the material of interest will be ejected into the vacuum. The outgoing electrons are collected and sent into an energy analyzer that sorts the electron pulses according to their kinetic energy E_k, so that the binding energy of the core state E_B can be estimated as

$$E_B = h\nu - E_k$$

The technique is element-specific, because the energy of the core levels are dependent on the element in the solid. In addition the shifting of this energy as a function of the chemical environment of the atoms can provide chemical information.

The magnitude of the chemical shift is large compared to the average line width of the x-rays ($\sim$ 5 eV), rendering XPS a useful tool for chemical analysis. The direction of the chemical shift can be understood in electrostatic terms. For example, when an atom is oxidized, the electron cloud around the nucleus will feel a larger positive charge at the nucleus, and that will shift the binding energies towards larger values.

The difference in electronegativity of the atoms participating in chemical bonding can also have an important influence on the position of the XPS peaks. For example, it is possible to distinguish between Se bonded to Cd and Se bonded to O by measuring the position of the Se 3d level, given the large electronegativity difference between Cd and O ($\Delta\chi = 1.75$), whereas it is not possible to establish an experimental difference between CdO and CdSe by measuring the Cd 3d spectra, because of the small difference in electronegativity between O and Se ($\Delta\chi = 0.89$) [42].

Even if x-rays can penetrate solids to a depth of several thousand atomic planes, the escape probabilities of a photoelectron decrease greatly with the distance it needs to travel inside the solid. At an energy of 50 eV the mean path of an escaping electron is of the order of 1 nm. In other words, XPS is a surface-sensitive techniques, even if for small nanocrystals (< 10 nm), for energies up to 10 times larger, we can assume that the whole of the nanocrystal is probed. This includes escape of the photoelectron from the nanocrystal and through the capping layer around it.

In the study of nanocrystalline systems, XPS has proven to be a valuable tool. Bowen Katari and coworkers[43] fixed CdSe nanocrsytals to a gold surface and followed the effect on the surface of the particles created by changes in the capping ligands, solvent used for precipitation and air exposure by XPS. In the nanocrsytals as prepared, the Se atoms appeared unbounded, while the Cd atoms were bonded to the capping trioctylphospine. When exposed to air, most of the Se was converted to SeO_2, treatment with pyridine stripped the surface of capping ligands and pyridine itself was removed in the high vacuum. After pyridine treatment both Cd and Se were oxidized by air.

Hines and Guyot-Sionnest [39] established the presence of a 0.6-nm shell of ZnS around a 3-nm CdSe core in the nanoparticles they prepared. The particles TOPO-capped particles were analyzed without stripping. Evidence of the core-shell arrangement was derived from the fact that the amount of Zn observed was three times larger than the amount of Cd.

4.2 Experimental

The samples for XPS were prepared by pressing a small amount of the free-flowing powder against adhesive graphite tape. The XPS was collected in a Kratos Axis Ultra with an efficient charge balancing system and a monochromated Al source of 1486.6 eV.

4.3 Results and discussion

The survey spectra of undoped and doped nanocrystalline CdSe are shown in Figure 4.1, and the details of the region where the main lines from Eu 3d appear are depicted in Figure 4.2.

Identification of the oxidation state of the Eu ion in the doped lattice can be achieved by inspection of the X-ray photoelectron spectra (XPS) in Figure 4.2, which shows contributions from Cd, and Eu. The energy of the transitions for the $3d_{5/2}$ and $3d_{3/2}$ of Eu between 1120 and 1180 eV allows assignment of the Eu valence as Eu(III) in the CdSe:Eu alloy samples by comparison to a bulk sample of Eu_2O_3. Eu(II) lines are found to shift to lower energy in the XPS. The Cd_{MNN} lines and the Se 3p lines at 1109 and 162 eV are observed to be invariant with doping. This suggests that the Cd(II) and Se sites are largely unperturbed by the presence of the Eu guest ion in the lattice, which is consistent with the idea of Eu sitting in octahedral holes in the wurtzite-type lattice. Similar observations have been made in transition metal ion doping of bulk lattices of CdSe and ZnSe [44].

The narrowing of the line width for the Cd$_{MNN}$ lines with doping apparent in Figure 4.2 is indicative of lower crystalline disorder (strain) in the doped sample, relative to the undoped material, potentially due to the pinning of the strain at the defect site.

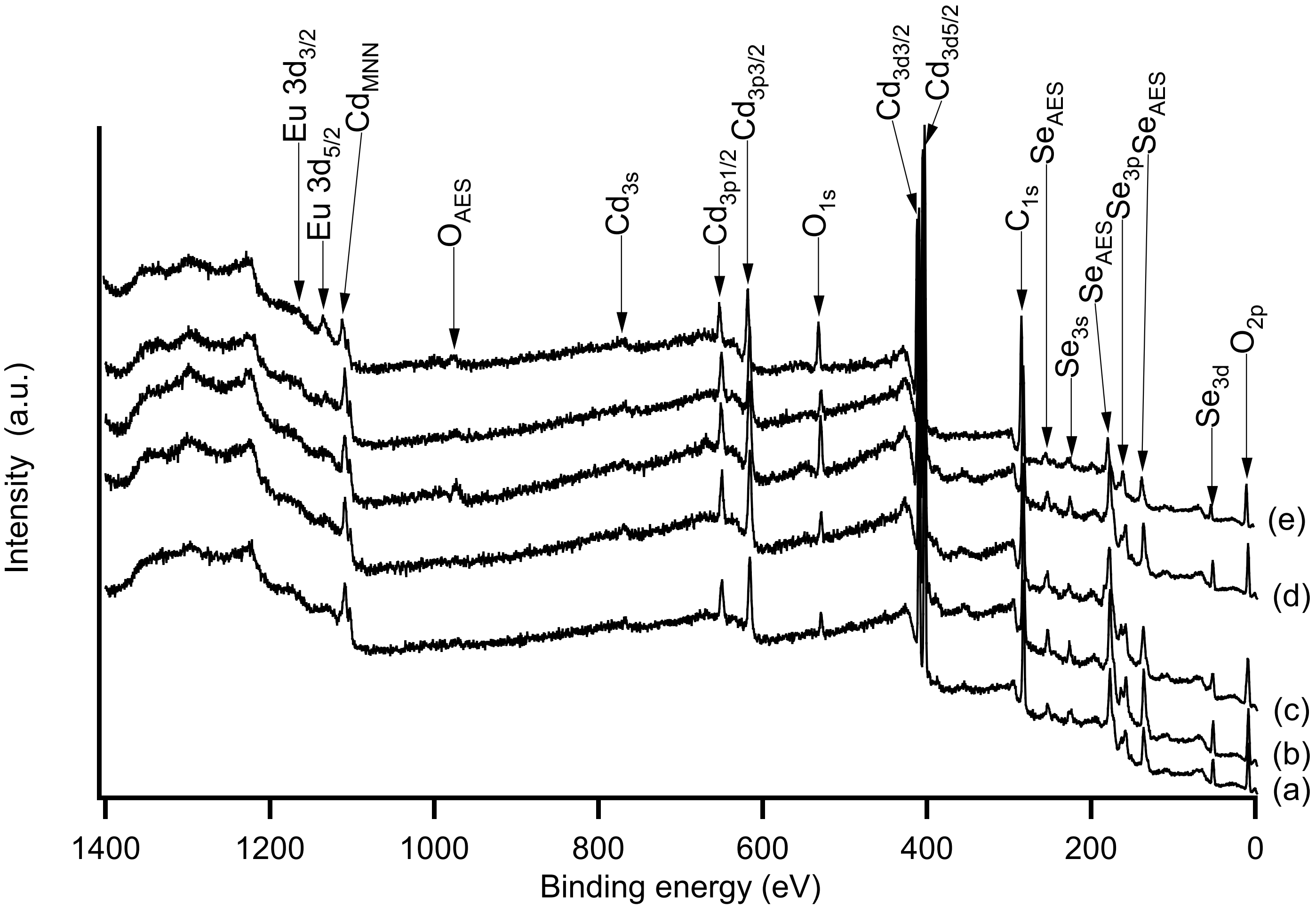

Figure 4.1. Survey XPS spectra of nanocrystalline undoped and CdSe:Eu alloy (a) undoped CdSe; (b) x = 0.030; (c) x = 0.054; (d) 0.132; (e) x = 0.206

The intensity of the XPS transitions can be integrated to get a semiquantitative estimation of the concentration of the sample components. The intensity of the C 1s transition can be used as an "internal standard". Figure 4.3 shows a plot of the areas of Eu 3d$_{5/2}$, Cd 3d$_{5/2}$ and Se 3d relative to C 1s. The error of the estimation is $\sim 20\%$, but even at that relatively high level, the quantitation allows to appreciate the increase in the Eu and the decrease in the Cd peaks as the concentration of guest ion increases, while the intensity of the selenium peak stays practically constant.

The XPS experiments allowed us the assessment of the oxidation state of Eu and the semiquantitative determination of the different components in the samples. But the usefulness of the technique is limited by the weakness of the signal and the large relative error in the measurements, and therefore the full characterization of our material requires the application of more powerful analytical tools, as detailed in the coming chapters.

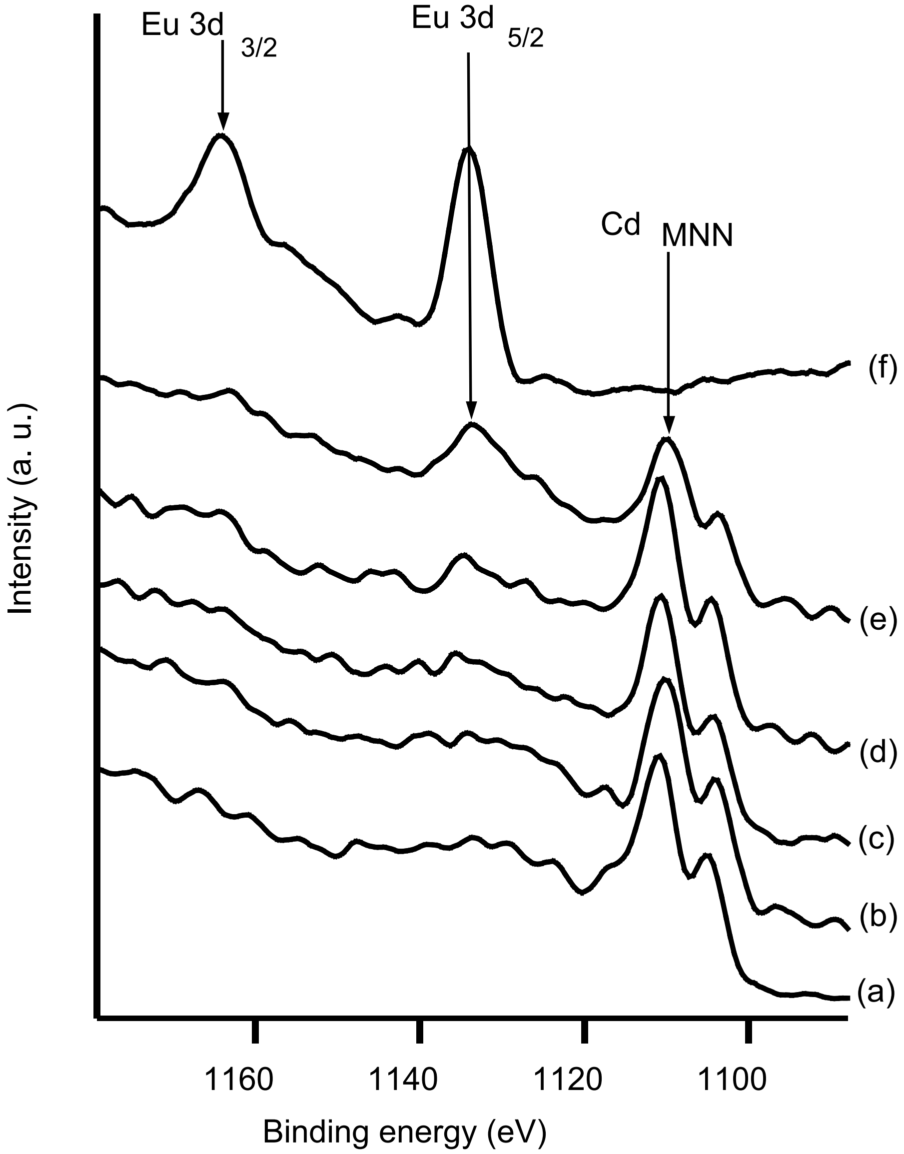

Figure 4.2. Detail of XPS of Eu-doped CdSe:Eu and standard compounds, : (a) undoped CdSe; (b) x = 0.030, (c) x = 0.054, (d) x = 0.132,(e) x = 0.206

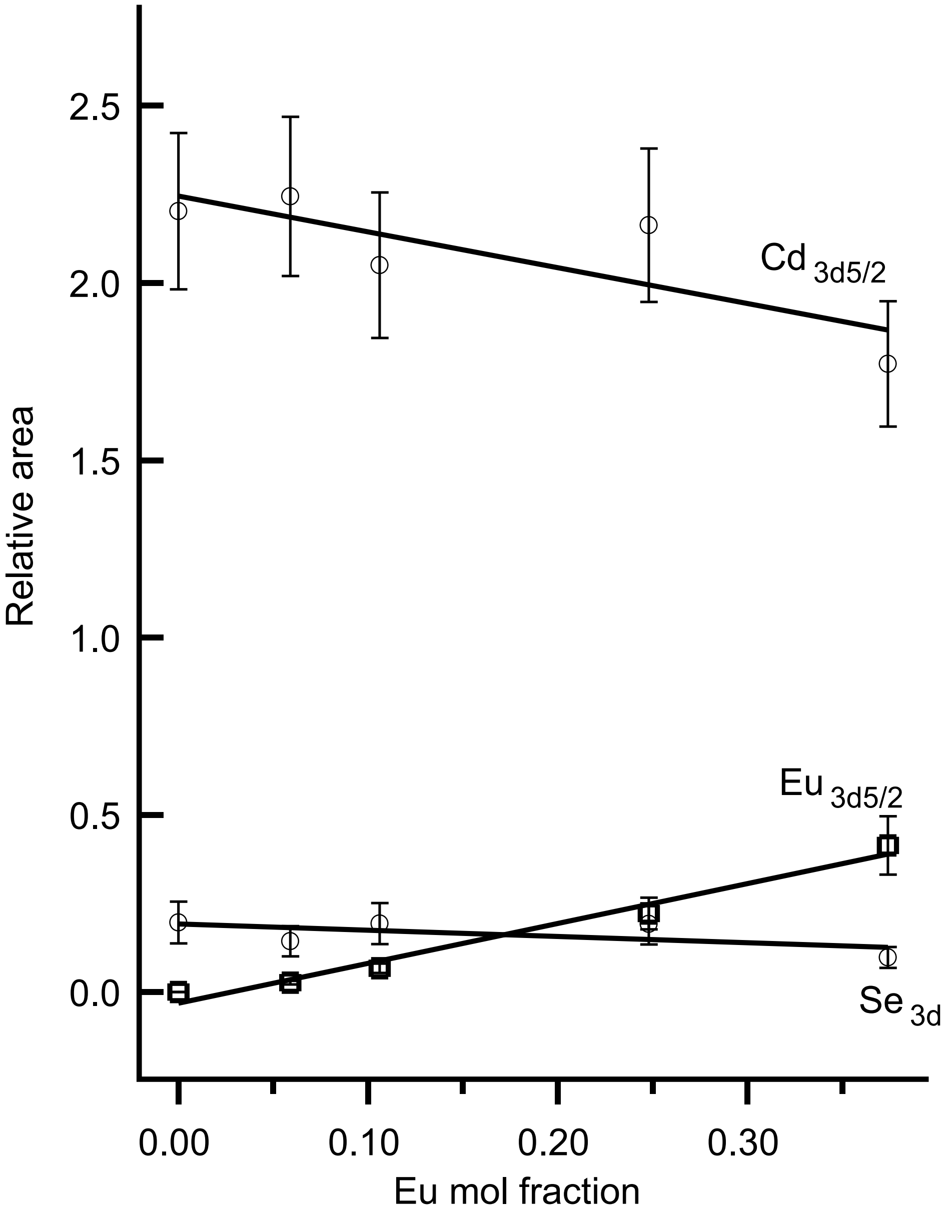

Figure 4.3. Semiquantitative estimation of the concentration of constituent elements in the CdSe:Eu samples

Chapter 5

Mössbauer (γ-resonance absorption) spectroscopy

5.1 Introduction

In Mössbauer (γ-resonance absorption) spectroscopy, the separation between the energy levels of atomic nuclei ($10^6 - 10^{10}$ eV) corresponds to the emission or absorption of a γ radiation quantum ($\lambda \sim 10^{-12} - 10^{-16}$ m). If the absorbing atom is in the condensed phase, an important fraction of the absorption events will happen without nuclear recoil (Mössbauer effect). To study this process, a suitable source of energy finely tuned to that of the nucleus of interest must be found. A significant body of experimental work has accumulated around the study of the Mössbauer effect in ^{151}Eu. The corresponding energy source is γ-active ^{151}Sm. The energy diagram is shown on Figure 5.1.

5.2 Experimental

In order to establish with certainty in which step of the preparation the oxidation of europium takes place, the samples intended for the Mössbauer study were prepared and isolated as described in Section 2.1. They were kept all the time under dry nitrogen. Their chemical composition was established by ICP-AES, as detailed in Section 2.2. The Mössbauer spectra were collected by measuring the absorption of the ^{151}Eu-transition at 21.53 keV with a 130 MBq ^{151}SmF$_3$ source (2 % of the total source activity). They were diluted with finely divided quartz ($\sim$ 75 μm) and sealed into a clear PVC container. The measurements were conducted in an Oxford Instrument liquid helium bath cryostat, at temperatures of 4.2, 77 and 300 K, regulated to $\pm$0.5 K in transmission geometry. The thickness and dilution of the samples were adjusted in order to get approximately 10 mg of Eu $\cdot$ cm^{-2} to the γ radiation.

5.3 Results and discussion

The Mössbauer spectra of the doped samples and of standard europium compounds are shown in Figure 5.2. The isomer shift δ and FWHM of the transition Γ derived from the fitting of the experimental data are summarized in Table 5.1. These results indicate that more than 95–98 % of the europium present in the doped materials is in oxidation state 3+, even if it was introduced in the reaction vessel as anhydrous EuCl$_2$ and the whole synthetic procedure and cleanup of the nanocrystals was carried out under nitrogen. The sample with the highest doping level (curve c in Figure 5.2) shows around 2–5 % of residual Eu(II). This is consistent with the residual magnetism found in the SQUID magnetometry measurements and attributed to the presence of a small amount of Eu(II) in the material.

An earlier experiment trying to dope cadmium selenide using $EuCl_3$ turned out unsuccessful. It seems reasonable that in the presence of easily reducible species such as Cd^{2+}, the europium ions readily oxidize and by reacting in that way, they get involved in the formation of the add-species participating in the growth of the nanoparticles. This may be driven by the energetic favorability of Eu sitting in an octahedral site inducing a $Cd^{2+} \rightarrow Cd^0$ reduction and subsequent vacancy formation.

Table 5.1. Isomer shift δ and FWHM $\mathit{\Gamma}$ derived from fitting the Mössbauer experimental data.

CdSe:Eu Eu mole fraction	δ (mm s^{-1})	$\mathit{\Gamma}$ (mm s^{-1})
0.004	0.675	2.632
0.006	0.727	2.806
0.037	0.694	2.819
0.041	0.651	2.817
0.055	0.680	2.882
Eu_2O_3	0.994	2.300
EuSe	-11.86	2.670

Given the ease of interconversion between the two oxidation states of europium, we investigated the Mössbauer spectrum of CdSe:Eu x=0.055 at 4 K. The resulting spectrum in Figure 5.3 gives evidence of the residual character of this Eu^{2+} and shows that practically no variation in the ratio Eu^{3+}/Eu^{2+} with the decrease in temperature.

The absence of asymmetry in the Lorentzian shape of the ^{151}Eu Mössbauer transition proves that Eu sits in a site of high symmetry, i. e., that at least a 3- or 4-fold axis passes through the atom center [45], but it does not allow further conclusions about the exact nature of the local environment around the impurity Eu^{3+} ion.

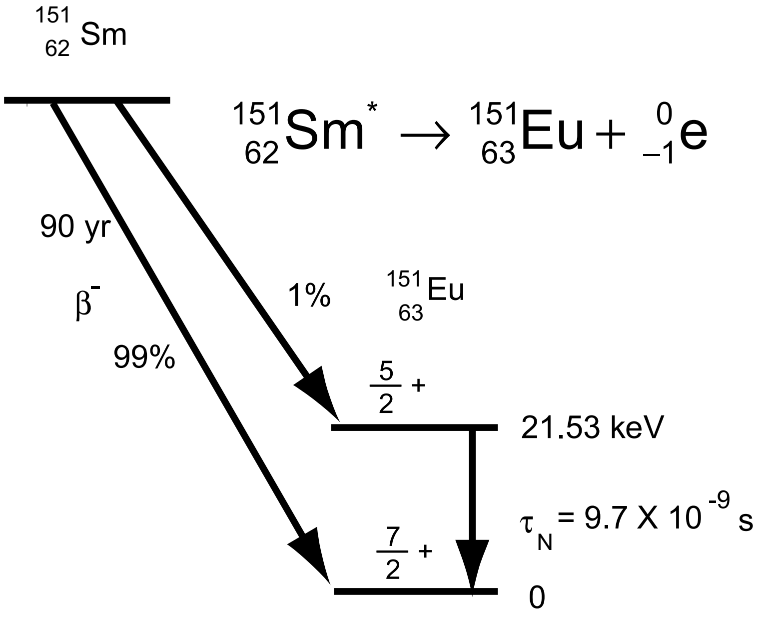

Figure 5.1. Energy levels involved in the nuclear transitions of ^{151}Eu and ^{151}Sm used for the collection of Mössbauer spectral data

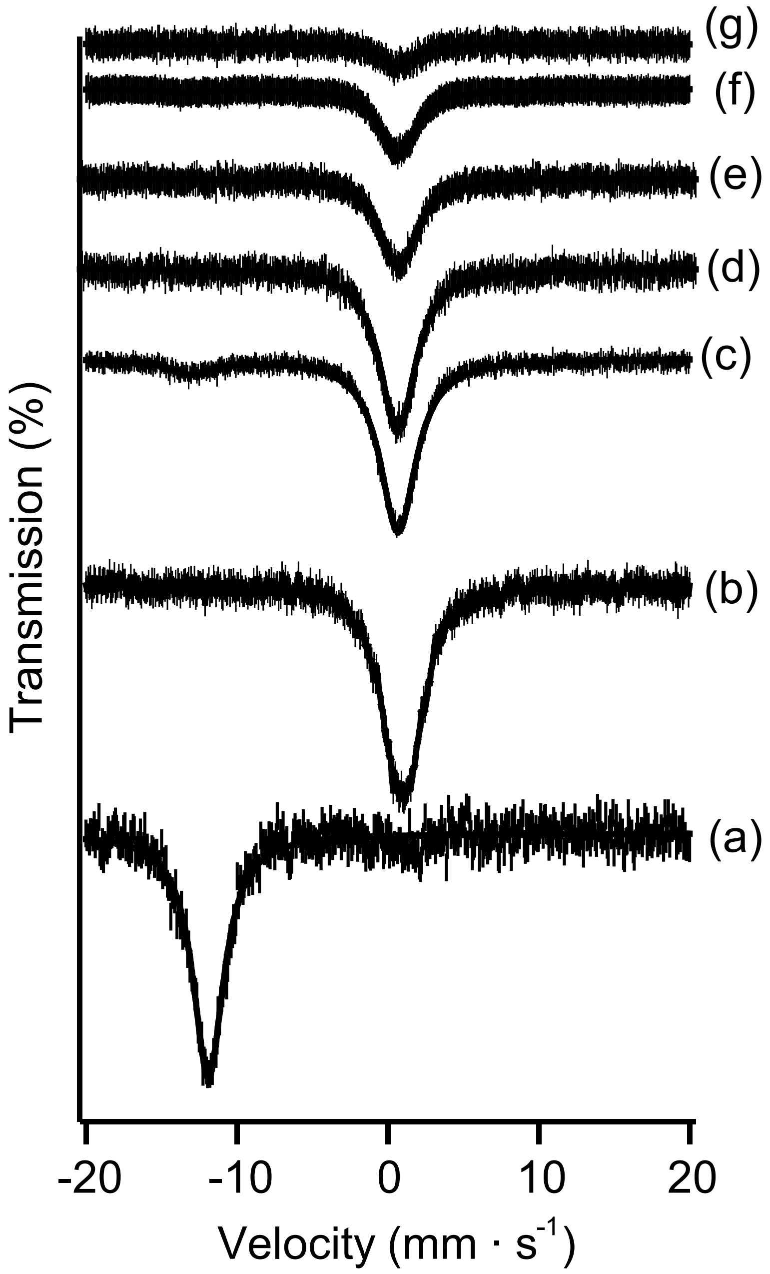

Figure 5.2. Mössbauer spectra of standard Eu compounds and CdSe:Eu: (a) EuSe; (b) Eu_2O_3; (c) CdSE:Eu x = 0.055; (d) x = 0.041; (e) x = 0.037; (f) x = 0.006; (g) x = 0.004

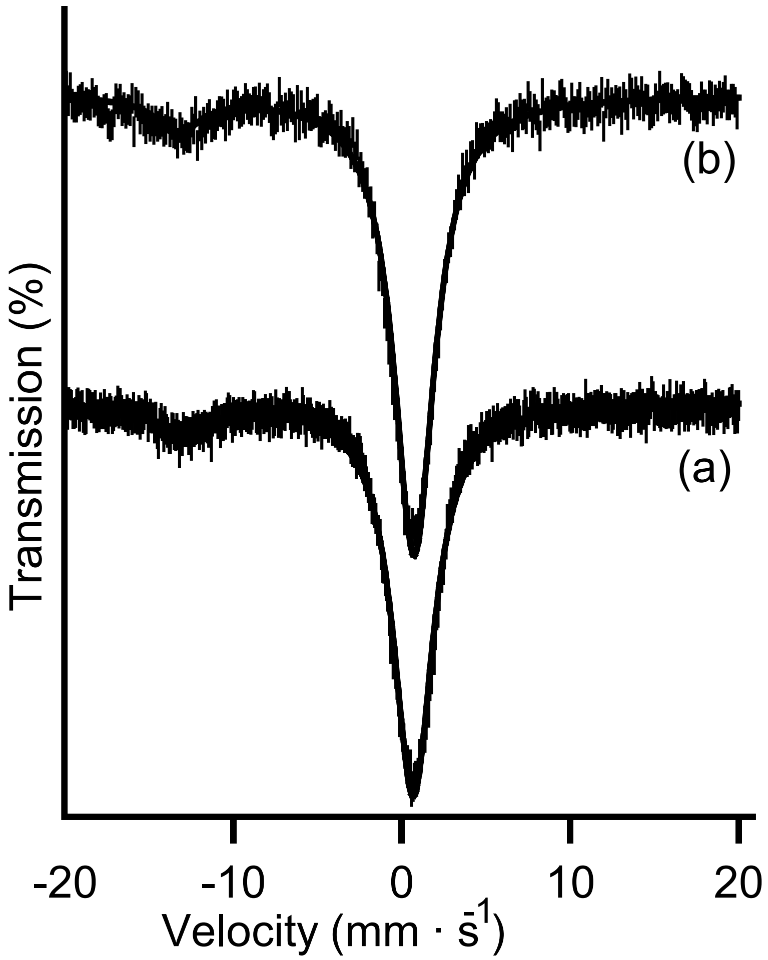

Figure 5.3. Mössbauer spectra of CdSe:Eu x=0.055: (a) T=77 K; (b)T=4 K

Chapter 6

XANES: Near-edge X-Ray Absorption

6.1 Introduction

X-Ray Absorption Spectroscopy (XAFS) is based on the measurement of the oscillations of the x-ray absorption coefficient up to 1000 eV past the absorption edge corresponding to the photoionization of a core electron of the absorbing element. These oscillations are observed only for condensed phase samples and can be explained by considering the final state of the ionized photoelectron as the result of the interference of the outgoing electron wave and the backscattered wave from the atoms surrounding the absorber, as shown in Figure 6.1. Some of the most important characteristics of this phenomenon turn it into a most powerful analytical tool for the problem at hand:

- It is element-specific. By using a suitable combination of monochromator and detector we can tune the measurement to the specific energy corresponding to the edges of the elements of interest, with practically no interference from the accompanying elements.

- It probes the short-range ordering around the absorber. Given the relatively short mean path of the photoelectron inside the condensed matter sample, the backscattered wave will originate only from the atoms in the first few coordination shells around the absorber. This allows the study of amorphous and low crystallinity (nanocrystalline) solids, in the size regime where the scattering techniques requiring long-range order start to fail.
- It is an extremely sensitive probe, when using solid-state fluorescence detectors, it allows to get information about atomic arrangements that would go undetected for most other structural techniques.

Figure 6.2 shows a typical XAFS spectrum, in this case based on the measurement of the cobalt K-edge at 7709 eV of a thin cobalt metal foil. The spectrum is conventionally divided in three distinct regions: the pre-edge, going back to around 200 eV, to the onset of the absorption edge, marked by an inflection point in the plot of μ(E) vs. E; the near-edge absorption region (XANES), extending from the onset of the absorption edge up to 30–50 eV above edge and the extended fine-structure absorption region from 30–50 up to 1000 eV past the edge.

Even if the division between this regions is not strictly fixed, the type of information that can be most likely extracted from data analysis is different in both cases. XANES carries mostly information about the chemical state (oxidation state, orbital mixing and spacing around the central atom), whereas the EXAFS region carries the information about the nature and number of backscatterers and their average distance.

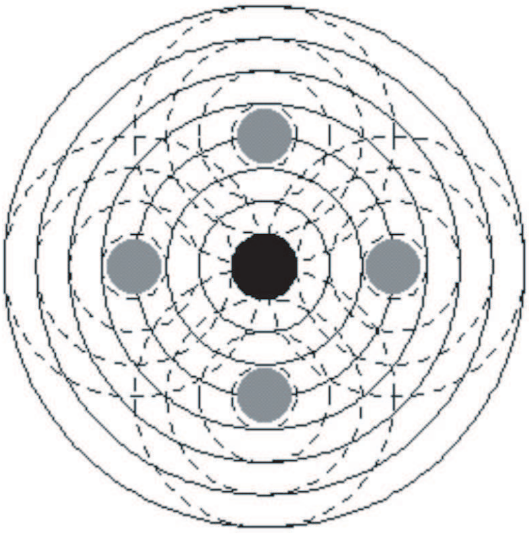

Figure 6.1. Final states as interference pattern between outgoing and backscattered waves (adapted from Reference [1]).

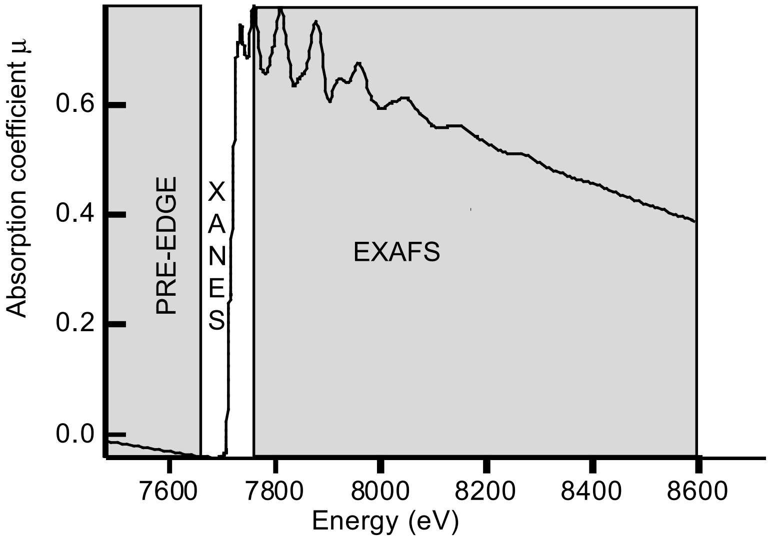

Figure 6.2. Regions of the XAFS spectrum

To extract this information, the raw data must be transformed according to well established procedures [46, 47], which include:

- averaging of 3 - 5 data sets for each sample, to minimize the effects of instrumental noise
- energy calibration by shifting the energy scale according to the position of the absorption edge in the spectrum of a sample of the pure element being measured, collected simultaneously with the analytical sample
- background removal, with a constant slope line in the pre-edge region and a cubic spline with five nodes in the region from 600 - 1000 eV past the edge
- changing from energy space to k-space, using the expression

  $$k = \sqrt{\frac{2m}{\hbar^2}(E - E_0)}$$

  where m is the mass of the electron, E is the photon energy and E_0 is the energy threshold of the edge
- normalizing the modulation in the absorption to the absorption of the free atoms $\mu_0(E)$, to obtain the EXAFS function:

  $$\chi(E) = \frac{\mu(E) - \mu_0 E}{\mu_0(E)}$$
- taking the real part of the Fourier transform of the EXAFS function, that shows peaks at distances corresponding to the succesive coordination shells around the absorbing atom

The EXAFS function can be calculated from first principles and fitted to the experimental data in order to derive the nature and number of the backscatterers and their distance from the absorbing center. Details of this procedure are given in Chapter 7.

XAFS is a signal-limited technique, the measured variations of the absorption coefficient are of the order of 1% and for this reason it is crucial to achieve a high signal-to-noise ratio. The so called “bench-top XAFS” requires extremely long data collection times (of the order of weeks for the early work on this technique). The introduction and world-wide availability of synchrotron radiation has transformed XAFS into frequently used tool for structural chemistry.

The characteristics listed for XAFS make it a technique ideally suited for the study of the local environment of impurity ions in semiconductor matrices, and it has been reported as an efficient probe since the earliest work in doped nanocrystalline semiconductors. Soo and coworkers [48] used XAFS to establish the coordination number of Mn^{2+} in ZnS:Mn, to show that no Mn clusters were formed as the guest ion was introduced in the nanocrystalline semiconductor lattice and that the interatomic distances between Mn and the neighboring S atoms were consistent with substitutional doping. They established the oxidation state of Mn as close but below 2+ and noticed its dependence on the nanocrystallite size.

More recently, Rockenberger et al. [49] applied XANES and EXAFS to the study of local structure in nanocrystalline SnO_2:Sb and found core substitution of Sn by Sb even at high levels of doping as well as the oxidation state change of Sb(III) to Sb(V) during the synthetic process.

In this chapter the results of the analysis of the XANES data collected at the Eu-L_3 and Cd, Se K-edges are presented. The following chapter is devoted to the results obtained in the same edges analyzing the EXAFS region.

6.2 Experimental part

Both XANES and EXAFS regions were recorded in fluorescence and transmission modes at beam line 7-3 of Stanford Synchrotron Radiation Laboratory (SSRL). The experimental settings used at this station are summarized in Table 6.1.

Table 6.1. Experimental settings of beamline 7-3 at SSRL

Source:	8-pole, 1.8-Tesla Wiggler ID Side Station
Storage ring current:	25 – 49 mA
Monochromator:	Parallel crystal geometry, Si(220) Downward reflecting
Energy range:	2400 — 35 000 eV
Energy resolution ΔE/E:	$\sim 10^{-4}$
Horizontal angular acceptance:	1.0 mrad
Spot size (FWHM):	2.0 mm x 20.0 mm
Absorption:	546 μm Be 2.7 m He 12.5 μm C
Instrumentation:	Detectors:30-element Ge Detector Array Liquid He Cryostat ion chambers (3) current amplifiers (3) sample positioners (2)
Interior hutch dimensions:	1.5 m long x 2.1 m high x 0.8 m wide

The experimental setup is schematically represented in Figure 6.3. The monochromator was 50% detuned to avoid the passage of higher harmonics. Cadmium and selenium, as pure elements, were used for energy calibration to measure their K edges at 26711 eV and 12658 eV respectively. The europium L_3 edge at 6977 eV was calibrated against the K edge of iron at 7112 eV. The XAFS data was collected a 30-element Ge detector and the measurements were conducted at room

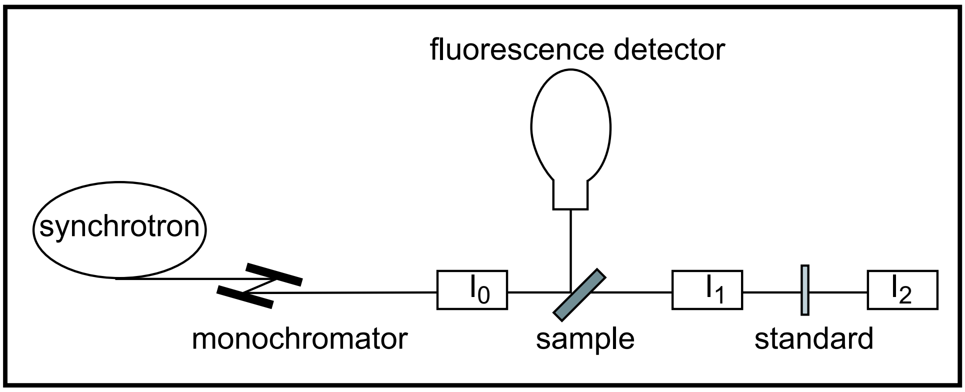

Figure 6.3. Schematics of experimental setup at SSRL beam 7-3

temperature (298 K) and at 10 K inside a continuous flow liquid helium cryostat. The powdered sample was sandwiched in Kapton tape. We collected at least five runs per sample and the data collected were averaged and energy-shifted using the standard package EXAFSPAK [50]. Further data manipulations were carried out using IFEFFIT with the Athena front-end [51, 52].

6.3 Europium

Based on XPS, Mössbauer, SQUID magnetometry, powder XRD as well as preliminary XANES data [53] the oxidation state of europium in our materials is most likely 3+. We had considered the formation of Eu^{3+} as a post-oxidation process, given the high density of defects that would be introduced by the substitution of Cd^{2+} by Eu^{3+} in the wurtzite-type lattice of CdSe. However, by the introduction of Cd^{2+} vacancies to accommodate the Eu(III) ion, the Eu(III) can sit on an *Oh* interstitial site, limiting the inherent strain of doping.

We prepared a new series of doped nanocrystals with total prevention of atmospheric oxidation to eliminate the possibility of post-oxidation process. The

XANES data for the Eu-L_3 edge of three of these samples are shown on Figure 6.4, along with the spectra of two model compounds corresponding to the 2+ and 3+ oxidation states of Eu.

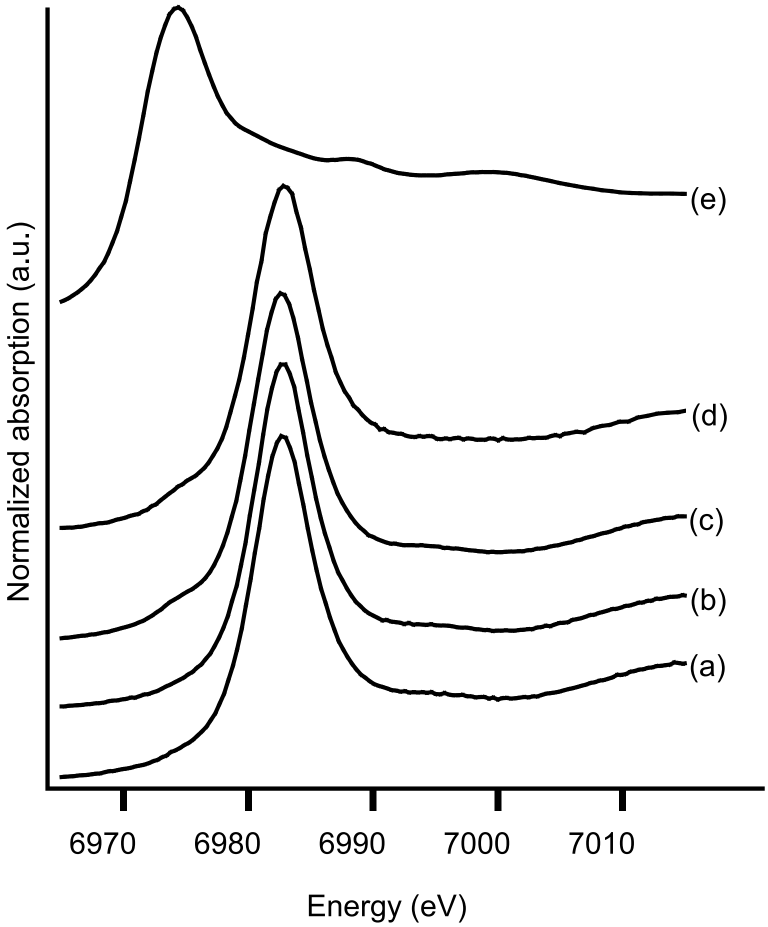

Figure 6.4. XANES Eu-L_3 edge of CdSe:Eu synthesized from $EuCl_2$ and kept under nitrogen at all times: (a) CdSe:Eu x = 0.002; (b) CdSe:Eu x = 0.032; (c)CdSe:Eu x = 0.063; (d) Eu_2O_3, (e) EuSe

Together with the Mössbauer results shown in the previous section, this figure gives conclusive assessment about the fact that Eu is found in oxidation state 3+ in our materials. Since the last synthetic runs were conducted in the absence of air, it seems reasonable to assume that the oxidation happens during the reaction of cluster decomposition and nanocrystal formation. Given the species present in the reaction pot, the most likely reaction appears to be: $2\mathrm{Eu}^{2+} + \mathrm{Cd}^{2+} \rightarrow 2\mathrm{Eu}^{3+} + \mathrm{Cd(s)}$. Under standard conditions, this reaction has a positive and small $\Delta\mathrm{G} = 9.65\ \mathrm{kJ} \cdot \mathrm{mol}^{-1}$, but since there is a tenfold excess of Cd^{2+} over the concentration of Eu^{2+}, it seems reasonable to expect a reversal of the spontaneous course of the reaction towards the products shown in this equation. This reaction would have no influence on the yield of product, because cadmium is found in great excess of the stoichiometric quantity needed to react with the selenium present in the reaction pot. The charge balance of the nanoparticles is then apparently split between the defect formation involving Cd vacancies (2 Eu^{3+} substitute 3 Cd^{2+}) that distort the lattice and introduce long-range disorder, as will be pointed out later in the analysis of the EXAFS results, and also by the presence of excess thiophenolate ions that occupy the surface of the nanocrystals as has been recently found in work done in our group [54].

6.4 Cadmium and Selenium in CdSe:Eu

In Figure 6.7 the XANES of Cd and Se K-edges are shown. The spectra of undoped nanocrystalline CdSe is shown also for comparison. A remarkable feature of these spectra is the much larger change in the area of the XANES feature nearest to the selenium edge, that scales with the concentration of the guest ion, while the Cd edge XANES is much less sensitive to the concentration of europium. In Figures 6.7B and 6.7A the XANES curves have been overlayed for easier comparison. They have been normalized to the step in the absorption

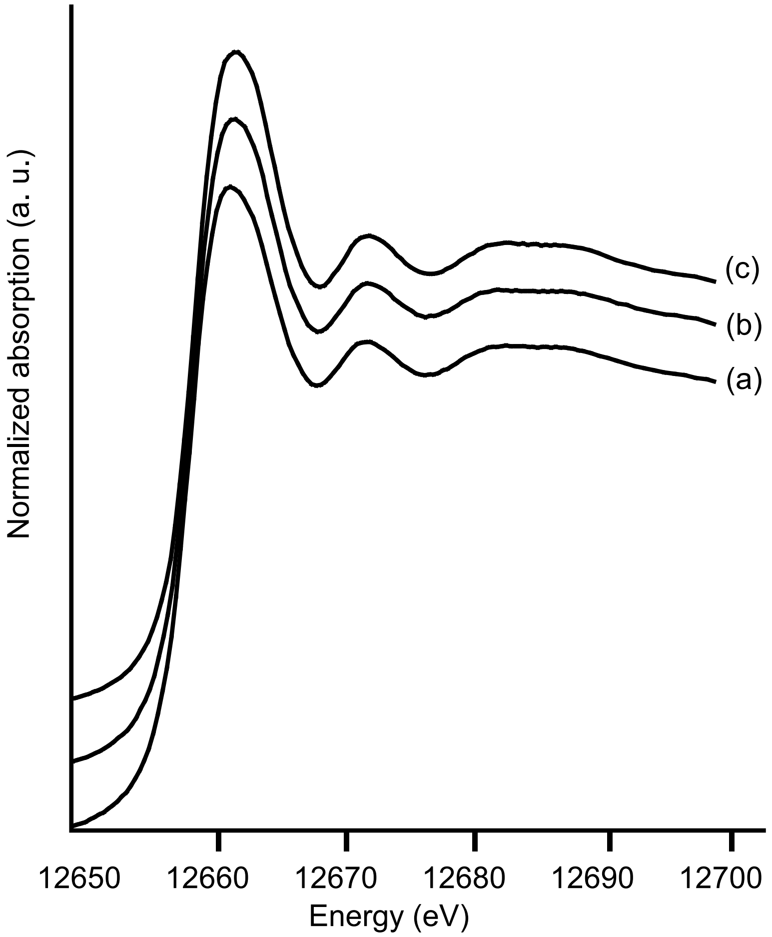

Figure 6.5. Se K-edge XANES of CdSe:Ee : (a) nc-CdSe; (b) CdSe:Eu x = 0.054; (b)CdSe:Eu x = 0.132

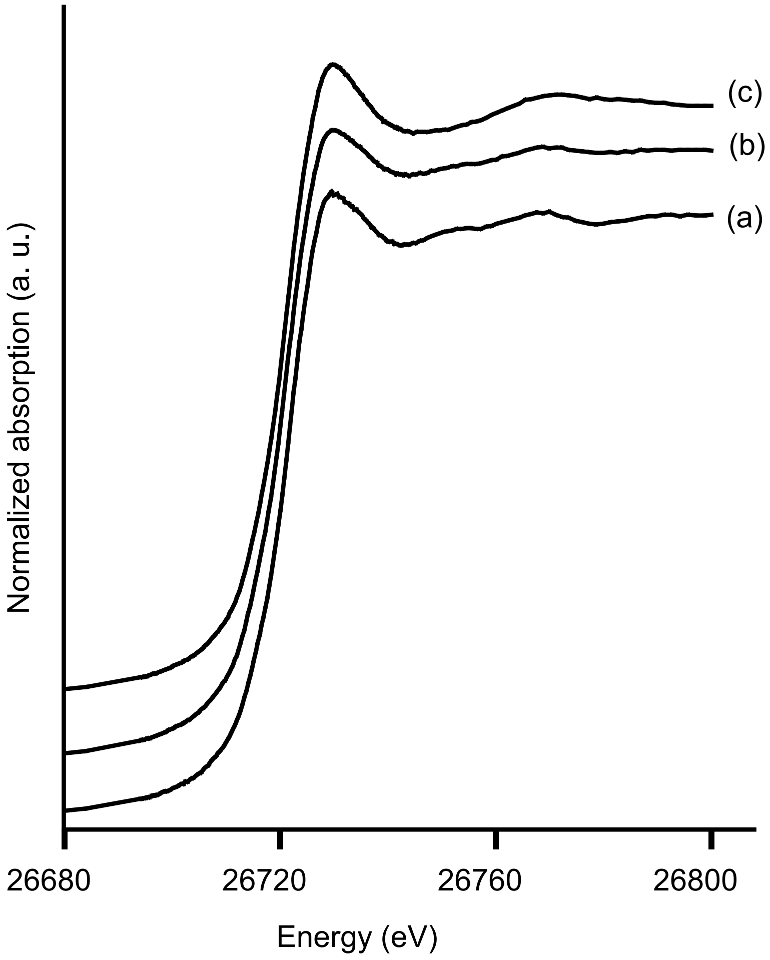

Figure 6.6. XANES of Cd K-edge CdSe:Eu (a) nc-CdSe; (b) CdSe:Eu x = 0.054; (b) CdSe:Eu x = 0.132

edge, so that the details of the changes in the features of the edge become evident. The percent change in the height of the prominent feature in the spectrum has been plotted against the molar concentration of europium in the nanocrystals in Figure 6.8.

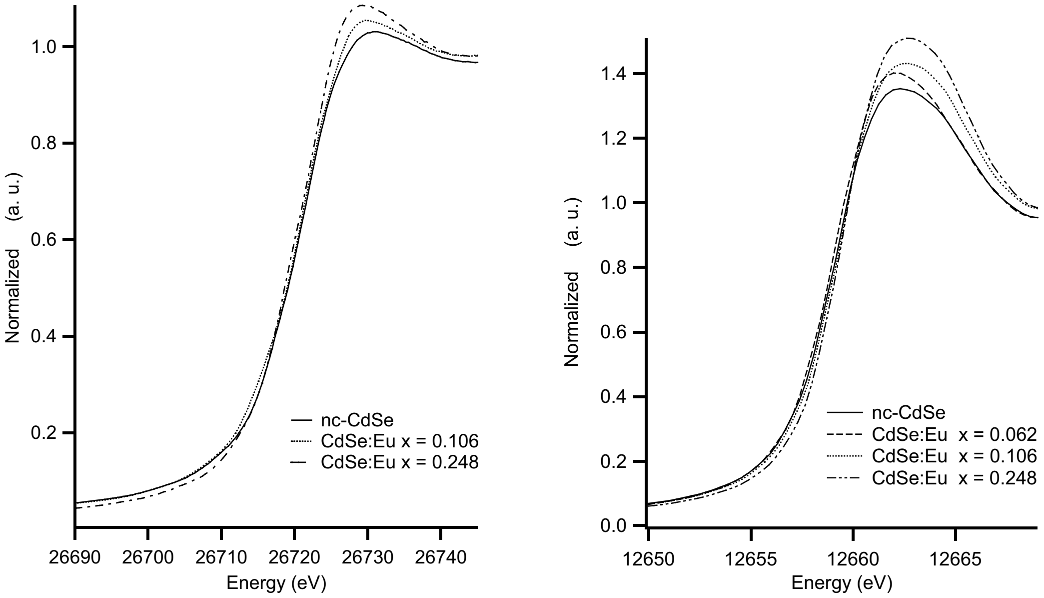

Figure 6.7. Detail of XANES spectra of CdSe:Eu (A) Cd K-edge; (B) Se K-edge

They show a linear increase of the height as a function of the concentration of the dopant. The slope of the line corresponding to Se is almost five times larger than that corresponding to Cd. This would be expected, for Eu is coordinated by Se and interacts strongly with the first shell. The variation in the selenium XANES can be attributed to a local change of the electron density on the selenium centers brought about by the introduction of the Eu(III) on an interstitial O_h hole. In the case of Cd, we do not see such a displacement change, which is to be expected because the environment around the Cd ions is only altered in the second coordination shell when the nanocrystals are doped and therefore unoccupied Cd states are practically unaffected by the presence of guests cation in the

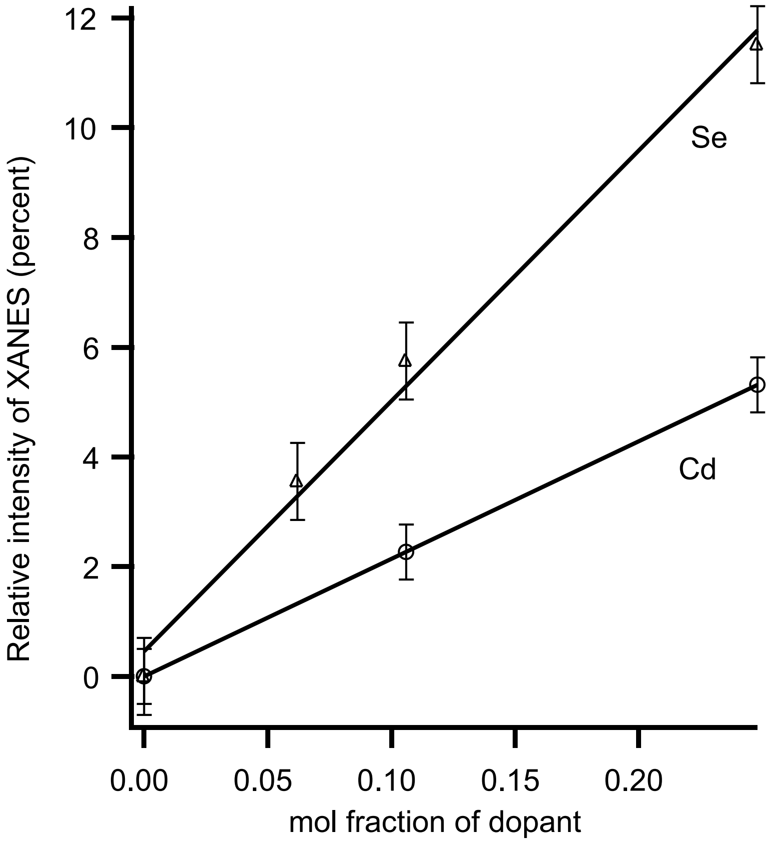

Figure 6.8. Percent change in the main feature of XANES region for Cd (a) and Se (b) K-edges vs. the molar concentration of Eu

lattice. These changes in the features of XANES depending on the local environment around the absorbing ion have been reported for other elements. Yoon and coworkers [55, 56] applied a similar normalization to observe the changes in the Co K-edge XANES brought about by concentration of Li^+ and the introduction of Al^{3+} in a matrix of $LiCoO_2$, and they argument about the usefulness of this approach to characterize the change in the density of states distribution around the absorber ion. The effect of the strong modulation of the edge shape by the densitiy of states distribution has been described by Sobczak et al. [57] in the study of Pd XANES, and used to study the catalytic activity of Pd as a dopant in polyaniline.

To gain better insight into the local lattice effects, the projected local density of states on the selenium atom were calculated using FEFF8. The results of the calculation for a 2 nm undoped system, shown in Figure 6.9, in which the four cadmium atoms around the absorbing selenium replaced by europium atoms are shown in Figure 6.10, where a significant difference in area but not in position is shown in the p and d orbitals of Se above and below the Fermi level. The K-edge absorption measures mostly the promotion of a 1s electron into empty p orbitals. The change in the XANES is consistent with the change in the density of p states. This supports a local lattice effect brought about by the introduction of Eu. In any case, the calculated change is larger than what can be observed experimentally, because the high concentration of Eu around the central Se absorbing atom in the model is an extreme and unlikely case in the actual nanocrystal.

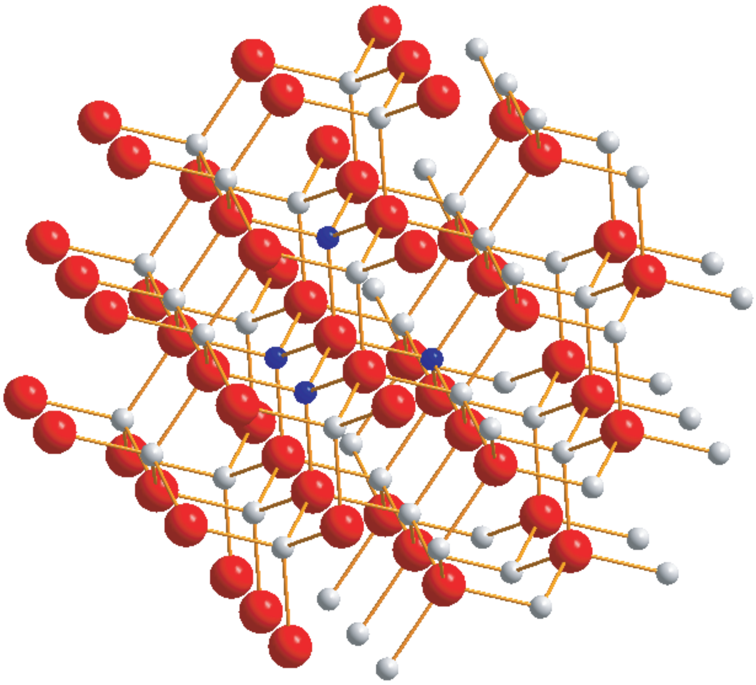

Figure 6.9. Model for FEFF8 calculation of Se DOS. The blue spheres represent Eu guest ions

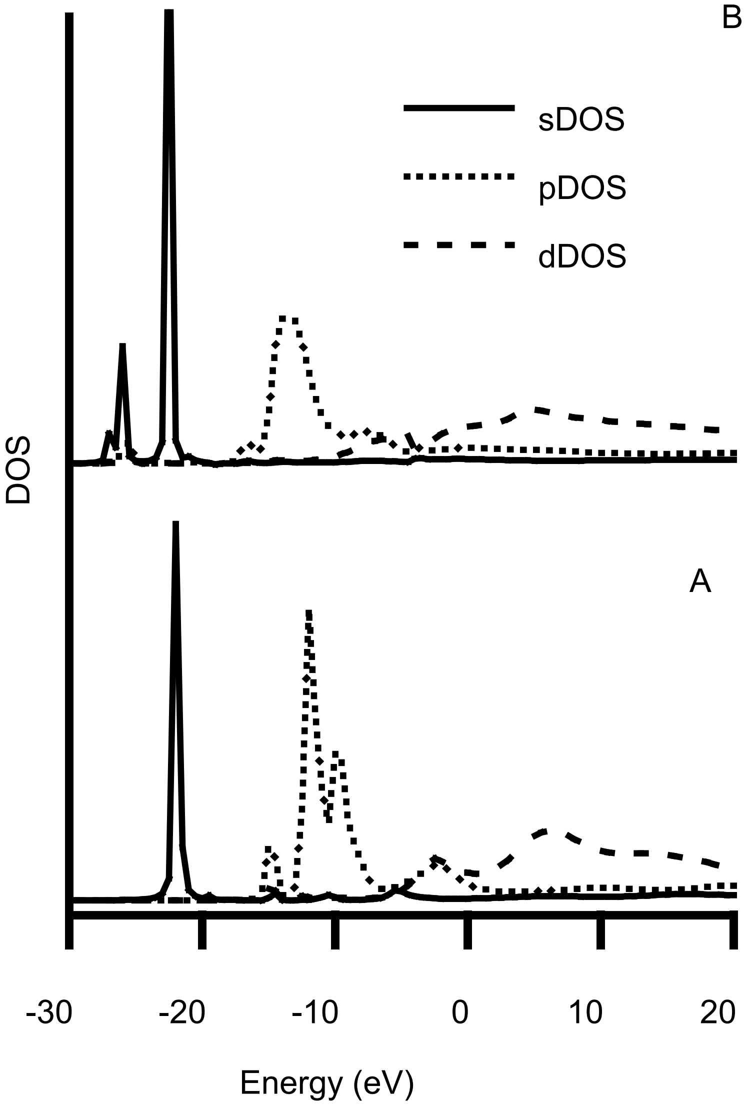

Figure 6.10. Se projected DOS: A) undoped CdSe B) CdSe with all four Cd substituted for Eu around the central absorbing atom.

Chapter 7

EXAFS:

Extended X-Ray Absorption Fine Structure Spectroscopy

7.1 Introduction

7.2 Europium

The measurement of Eu-L_3 edge EXAFS at 300 K were presented in our previous paper [53]. We compared the distance measured between Eu and the selenium atoms in the first coordination shell in the doped samples (ranging between 218 –227 pm) and compared it with the distance calculated by the ab-initio code FEFF 7 for a theoretical model in which an Eu atom was placed substituent of the central Cd atom in a 2 nm cluster (224 pm). There was an excellent agreement, ruling out the possibility of Eu forming a segregated phase either as EuSe (d_{Eu-Se} = 309 pm) or as Eu_2Se_3 that crystallizes in an orthorhombic structure of Sc_2S_3 type belonging to space group $F\ d\ d\ d$ with interatomic distances above 250 pm [58].

In Figure 7.1 the Eu-L_3 edge EXAFS of a new series of CdSe:Eu nanocrystals collected at 4 K are shown. The top panel shows χ(k) weighted by k^3 in the k interval 0.02–0.11 pm^{-1}. The bottom panel shows the magnitude of the Fourier transform in the same k range using a Kaiser-Bessel window of dk = 4. The figure also shows the results of the fitting of the the first coordination shell using a theoretical standard calculated by FEFF8 following the approach proposed by Ravel et al. [59, 60], in which a series of multiple scattering paths are calculated from a theoretical structure described in terms of the crystallographic coordinates of its atoms. The fitting was done in R-space using the code *IFFEFIT*. This program calculates the EXAFS as a sum of the contribution of different backscattering paths j, using the expression:

$$\chi(k) = \sum_j N_j \cdot S_0^2 \cdot F_j(k) \cdot \exp\left(-2\sigma_j^2 k^2\right) \cdot \exp\left(-\frac{2R_j}{\lambda_j(k)}\right) \cdot \frac{\sin[2kR_j + \phi_{ij}(k)]}{kR_j^2}\ , \quad (7.1)$$

in which S_0^2 is the amplitude reduction factor to account for the damping of the electron wave caused by many-body processes; F(k) is the amplitude function and $\phi_{ij}(k)$ the phase function calculated for each path by *FEFF*; σ_j^2 is the Debye-Weller factor that relates to the uncertainty in position caused by thermal vibrations; λ is the photoelectron mean path and R_j the uncorrected distance between the absorber and the backscatterer.

The model constructed places a europium atom in an octahedral hole of an undistorted CdSe lattice, cadmium vacancies are generated next to the Eu atom.

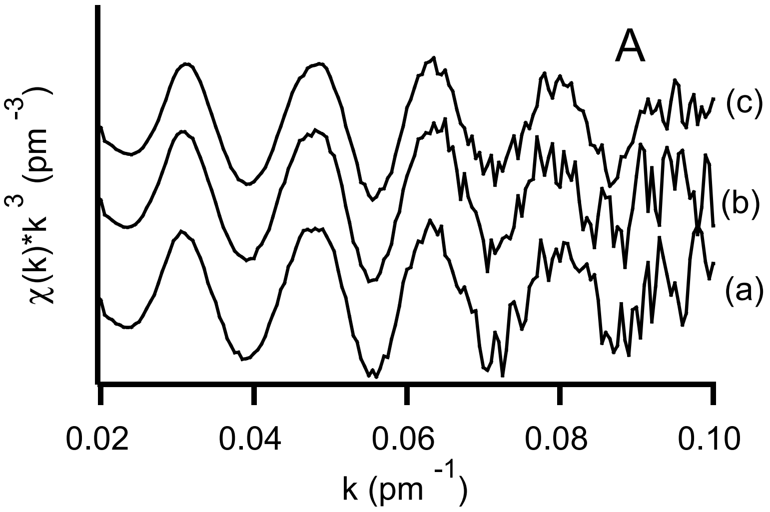

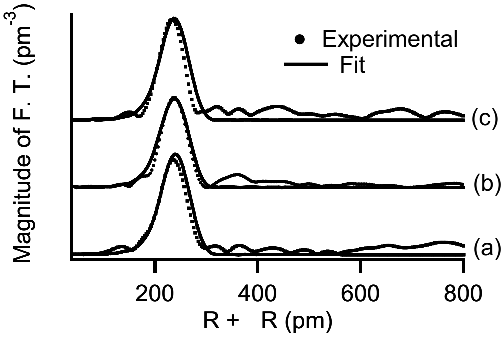

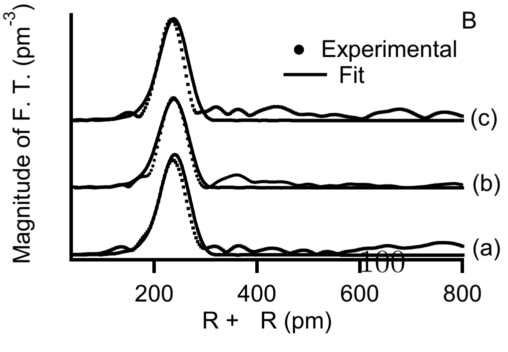

Figure 7.1. Eu-L_3 EXAFS spectra of nc-CdSe:Eu (A) $k^3 \cdot \chi$ vs k; (B) F.T. vs R, experimental and fit(a) CdSe:Eu x = 0.002 ; (b) CdSe:Eu x = 0.032; (c) CdSe:Eu x = 0.062

in the center of a cadmium selenide nanocrystal. The main parameters to extract from the fit are the radial distance of the first shell (R) and the coordination number around the europium atom (N). Due to the very strong correlation between N and the amplitude reduction factor (S_0^2), we fixed the latter at 0.90, which allows to estimate N within ± 10%. The Debye-Weller factor for this series was determined by running a sample of bulk europium (II) selenide, which crystalline structure and europium coordination are known. The fitting of that model compound gave a σ^2 of 99 pm^2 for the Eu-Se shell. We used this value in the fitting of all the doped samples. The results of the fitting are listed on Table 7.1. An estimate of the goodness-of-fit is given by the R-factor calculated by IFEFFIT as described in Reference [52].

The proposed interstitial doping and the XRD measurements point towards a locally distorted crystal lattice around the dopant ion to coordinate an average of six selenium atoms at distances around 60 pm shorter than expected in the undistorted lattice. This is consistent with our model that allows Eu to sit on an O_h hole in the wurtzite lattice. As a consequence, we must have relatively high disorder around the dopant. The Eu EXAFS also supports this assumption since this is the only way we can account for the fact that the Cd and Se data collected at 4 K show clearly the second coordination shell which is almost completely absent in the Eu spectra.

Table 7.1. Fitting parameters for Eu-L_3 EXAFS for Eu-doped nc-CdSe

Sample	R (pm)	N	σ^2(pm^{-2})	E_0 (eV)	R factor
CdSe:Eu x = 0.002	235±3	6.2	99	-0.39	0.6447
CdSe:Eu x = 0.032	238±4	6.0	99	-5.26	0.6056
CdSe:Eu x = 0.062	237±2	5.8	99	-3.78	0.6344

7.3 Cadmium and selenium in CdSe:Eu

In a preliminary XAS data acquisition run we established that at room temperature there was only the possibility of measuring the effect of backscattering from the first coordination shell around the absorbing ions in our materials. This limitation has been reported by other researchers as well [61] and is linked to the relative lack of long range order in the nanocrystals, or in other words, to the fact that nanocrystals can be considered somewhat as a transition between glass-like disorder and crystalline order. Therefore, in order to study the Eu-doped nanocrystallites in greater detail, we conducted a run having our samples cooled down to 4.2 K. The resulting EXAFS spectra for Se-K edge are shown in Figure 7.2.

The fitting of the doped samples and of an undoped reference were carried out in in R-space using again theoretical standards calculated by FEFF8. In order to model the doped system, all the cadmium atoms around the central Se were substituted for europium. Even if this particular configuration is very unlikely at the dopant levels studied, it gives an acceptable starting point in order to consider the change in the electronic environment around the anions brought about by doping. During the fitting of the selenium EXAFS for a sample having approximately 20 mol % Eu, we assumed a coordination shell with a ratio N_{Cd}:N_{Eu} of 3:1 and floated the amplitude reduction factor. In the case of a sample with 10 at % Eu, the ratio was 3.6:0.4. The reported coordination number was back calculated from the fitted S_0^2 by fixing its value at 0.90.

The parameters derived from the fitting are summarized in Table 7.2. The Debye-Weller factor was estimated in each case from the analysis of pure EuSe and

Table 7.2. Fitting parameters for Se-K edges EXAFS for Eu-doped nc-CdSe

Sample	Shell	R (pm)	N	σ^2(pm^{-2})	E$_0$ (eV)	R factor
CdSe	Se-Cd	262±0.2	4.0	17.76	5.12	0.0172
	Se-Se	424 ±0.2	12.0	88.98	-4.3	
CdSe:Eu x = 0.054	Se-Cd/Eu	260±0.1	2.8/0.3	17.76/99	-5.26	0.0337
	Se-Se	427 ±0.1	10.6	88.98	-1.36	
CdSe:Eu x = 0.132	Se-Cd/Eu	261±0.1	3.0/1.0	17.76/99	2.09	0.0367
	Se-Se	427 ±0.1	9.4	88.98	-1.12	

of undoped CdSe and were transferred to the calculations of the doped samples.

The EXAFS data collected for Cd-K edge is shown in Figure 7.3 and the fitting results are collected in Table 7.3. As stated previously in the XANES section, the local environment around the cadmium ions is not affected by the doping in the systems, which futher confirms the doping model proposed for these materials. The EXAFS of the doped and undoped nanocrystals could be fitted with practically the same parameters. The data collection at the Cd K-edge happens at the upper limit of wavelength available from the monochromator at the station used, and therefore it is noisier that the data collected for europium and selenium. When analyzing Cd we ran also a sample of bulk CdSe. It is clear from the analysis of the Cd EXAFS that the level of disorder in the nanocrystals is remarkable, since in the bulk sample the second coordination shell around Cd, composed of 12 Cd atoms shows as a very distinct maximum in the radial function, whereas in the nanocrystals the signal is greately diminished, more so in the doped that in the undoped sample.

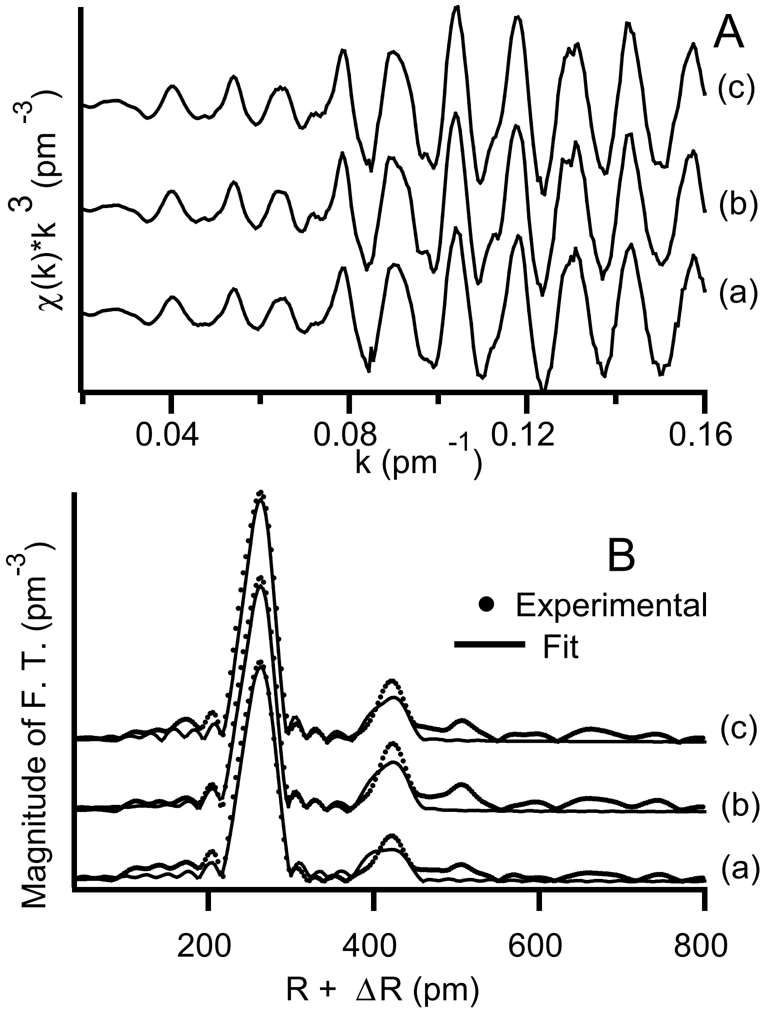

Figure 7.2. Se K EXAFS spectra of nc-CdSe:Eu (A) $k^2 \cdot \chi$ vs k; (B) F.T. vs R (a) CdSe:Eu x = 0.002; (b) CdSe:Eu x =0.032; (c) CdSe:Eu x =0.062

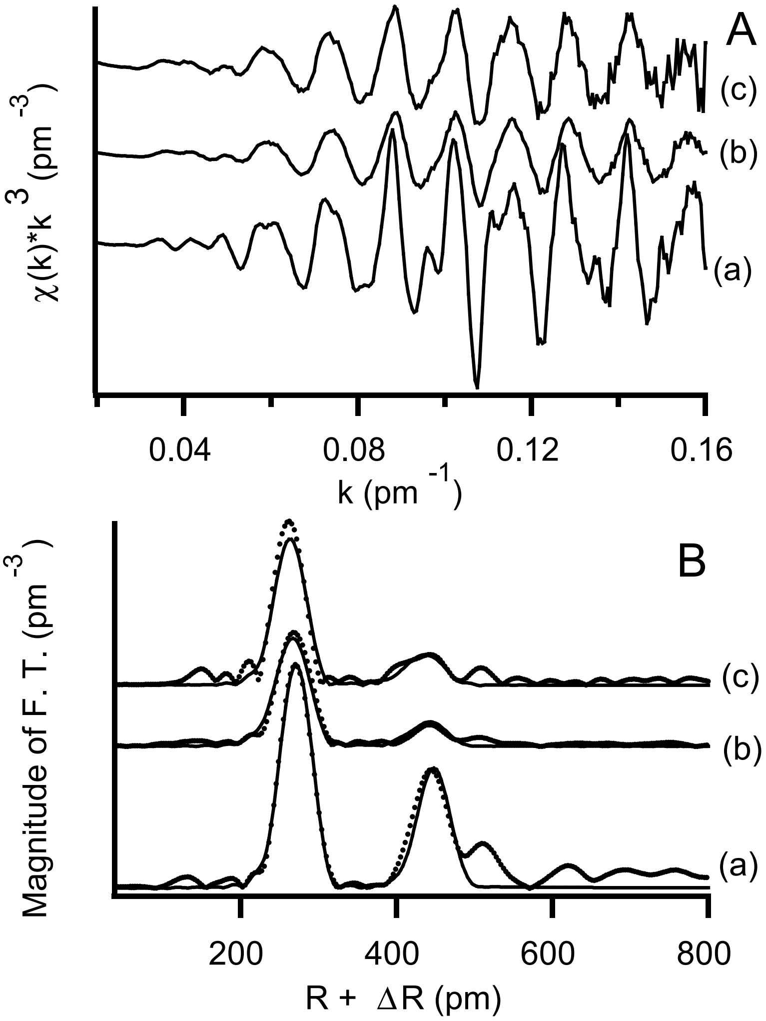

Figure 7.3. Cd K EXAFS spectra of nc-CdSe:Eu (A) $k^2 \cdot \chi$ vs k; (B) F.T. vs R (a) CdSe:Eu x = 0.002; (b) CdSe:Eu x = 0.03; (c) CdSe:Eu x = 0.062

Table 7.3. Fitting parameters for Cd-K edge EXAFS for Eu-doped nc-CdSe

Sample	Shell	R (pm)	N	σ^2(pm^{-2})	E_0 (eV)	R factor
CdSe $_{\text{bulk}}$	Cd-Se	264±0.1	4.0	23.36	1.8	0.0420
	Cd-Cd	448 ±0.1	12.0	34.51	-24.3	
CdSe $_{\text{nanocryst.}}$	Cd-Se	262±0.1	4.0	59.89	0.12	0.0813
	Cd-Cd	457 ±0.1	12.0	98.00	-43.6	
CdSe:Eu x = 0.132	Cd-Se	262±0.1	3.0	25.24	-1.2	0.0112
	Cd-Cd/Eu	419 ±0.1	10.8/0.2	11.00	5.2	

Chapter 8

Eu:CdSe: Conclusive remarks for Chapters 2 to 7

The results of applying XAFS and Mössbauer spectrometry to the study of europium doped cadmium selenide nanocrystals provides evidence of the europium guest ions sitting on sites of high symmetry as well as of an increase in the coordination around the cation that is not compatible with substitutional doping on the cadmium sites, and in consequence, a model with Eu sitting on octahedral holes of a distorted wurtzite-type cadmium selenide lattice is proposed. The disordered environment around the absorbing atom is shown by the decrease in the hight of the signal corresponding to the second coordination shell in the pseudo-RDF obtained by Fourier-transforming the EXAFS signal. Since the TEM and XRD data shown here and elsewhere show the conservation of the overall crystallinity in the nanoparticles, we conclude that the disorder is localized around the dopant. Another conclusion of this study is the understanding of the incorporation of europium into the crystalline lattice of the growing nanocrystals via an oxidative addition, since we did not succeed when trying to introduce Eu(III) directly into the reaction mixture but have proven to have Eu(III) as a dopant even if our starting material contained Eu(II) and the whole synthetic and characterization processes were carried out with exclusion of air.

Nanocrystalline semiconductors have not been characterized to date using the traditional x-ray and neutron diffraction techniques, and therefore we must rely on indirect evidence to establish the structure of these compounds. One way to get an insight into these materials is by measuring the luminescence originating from the dopant ion and to deduce the geometry of the site based on the crystal field splittings found. But for the case of these particular nanocrystals we have found almost total quenching of the luminescence, which renders the technique unusable in this case. Another important characterization tool capable of establishing the symmetry around the europium ions are magnetic measurements, but they are limited to the magnetic ion Eu^{2+} (ground state $^8S_{7/2}$) and yield practically no information from the magnetically silent Eu^{3+} (ground state $^7F_0$).

In the resonance Raman spectra of CdSe:Eu there are prominent features appearing at 265 and 290 cm^{-1} that are not present in the spectra of the undoped sample [62]. These new vibrations might be the result of reducing the symmetry of the lattice by the introduction of the dopant.

Chapter 9

Characterization of nanocrystalline CdSe:Co

By applying XAFS to a system composed of nanocrystalline CdSe with Co as a guest ion we gained the possibility of comparing the disorder in this system with respect to the Eu doped one. The fact that Co has an identical charge compared to Cd in this material would suggest that the presence of the guest would have a lower impact in the structural parameters of the nanoparticles. Also since the XANES in the K-edge of Co is quite rich in distinct features, we can gain better insight into the changes in the electronic structure brought about by doping in these systems.

The details of the preparation and characterization of CdSe:Co have been published elsewhere by Hanif et al. [23], therefore no experimental description on the synthesis and characterization by other techniques of these samples are given here. I will only develop the details of the analysis of the XAFS spectra.

9.1 XANES

The experimental conditions for these measurements are the same as described in Section 6.2

The analysis of the structure of the x-ray absorption spectrum around the Co K-edge at 7709 eV reveals interesting aspects about the interaction of the dopant and matrix orbitals based on the energy and availability of the unoccupied electronic states that receive the ionized 1s electron.

In Figure 9.1 the details of the XANES region for samples of cobalt metal, cobalt selenide and CdSe:Co nanocrystalline alloys collected at 300 K are shown. The doped samples differ in the treatment of the surface of the nanocrystals after the synthesis (for details see [63]). In the spectrum of CoSe there are three very distinct features in the XANES region, labelled in the figure as A, B and C. As can be observed, the development of this feature is better in the doped nanocrystals as compared to pure CoSe. The transition shown by the A feature has been assigned to the transition of the ionized electron up to the unoccupied d-like orbitals in the conduction band of the semiconductor [64].The experimental evidence shown in this figure suggests that there is better mixing of the Co p orbitals with the empty d orbitals of selenium. This fact is related to the different crystal structure of CoSe (NiAs-type structure) and CdSe (wurtzite-type) structure.

9.2 EXAFS

The results of the EXAFS collected at 4.2 K corresponding to three different levels of doping in CdSe:Co for the Co K-edge are presented in Figure 9.2. The

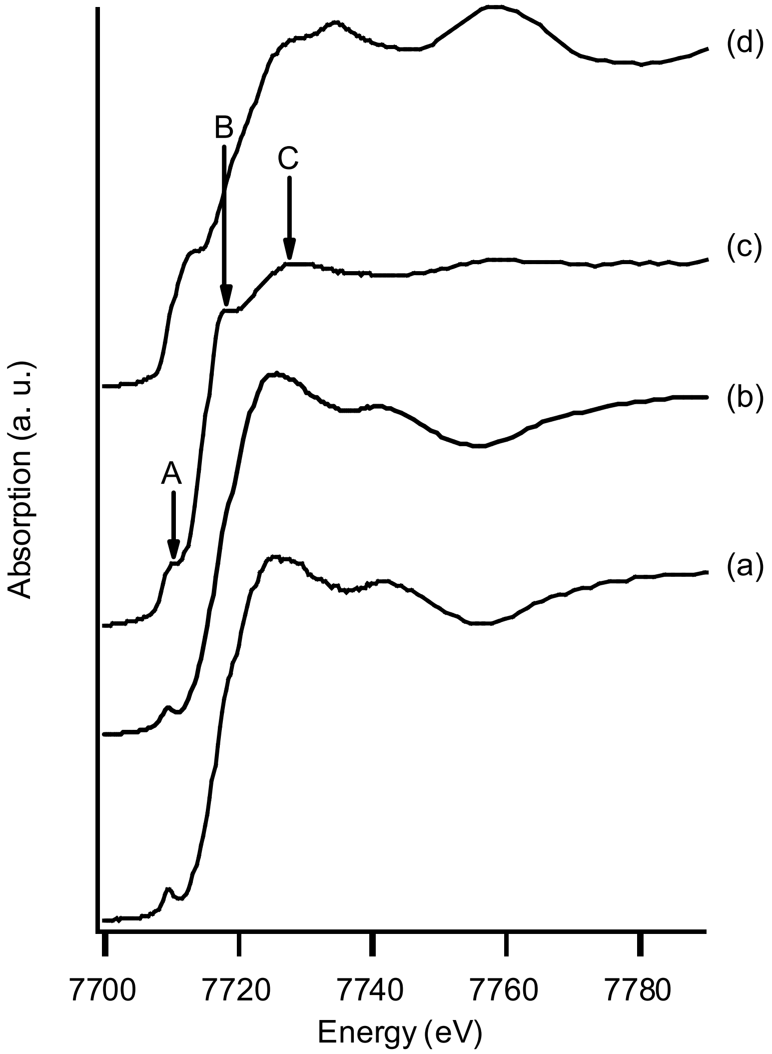

Figure 9.1. XANES of Co compounds and CdSe:Co alloys: (a) unstripped CdSe:Co x = 0.05; (b) stripped CdSe:Co x = 0.05; (c) bulk CoSe; (d) Co metal foil

data handling and modelling approach details have been described previously for the Eu system. The results of fitting the experimental curves to the FEFF8-generated paths are summarized in Table 9.1.

In this case we can immediately see from inspection of the table, that the coordination around Co is much closer to 4 than in the case of Eu, which is expected given the ease of Co^{2+} substitution a T_d site. As previously reported [23], a lattice contraction is observed, which corroborates the random substitutional model in which the smaller Co^{2+} (r_{Co} = 72 pm) replaces the larger Cd^{2+} (r_{Cd} = 95 pm) ion [41], giving an average Co-Se distance of 244 pm, compared to an average Cd-Se of 262 pm for the undoped samples.

The possibility of phase segregation is also ruled out by these results, since in the crystal structure of CoSe, belonging to space group *P 6 3/m m c*, each Co is surrounded by 6 Se at 248 pm.

The presence of second and third coordination shells in the spectra of these doped samples points out to a higher degree of crystallinity than what was found for the europium doped systems, an expected consequence of the charge balance present in the case of Co.

Table 9.1. Fitting parameters for Co K-edge EXAFS for Co-doped nc-CdSe

Sample	R (pm)	N	σ^2(pm^{-2})	E_0 (eV)	R factor
CdSe:Co 200 mg dopant	244.2±3	5.1	104	-19.1	0.092
CdSe:Co 400 mg dopant	244.9±4	4.8	104	-19.0	0.080
CdSe:Co 700 mg	244.9±2	4.2	104	-18.8	0.091

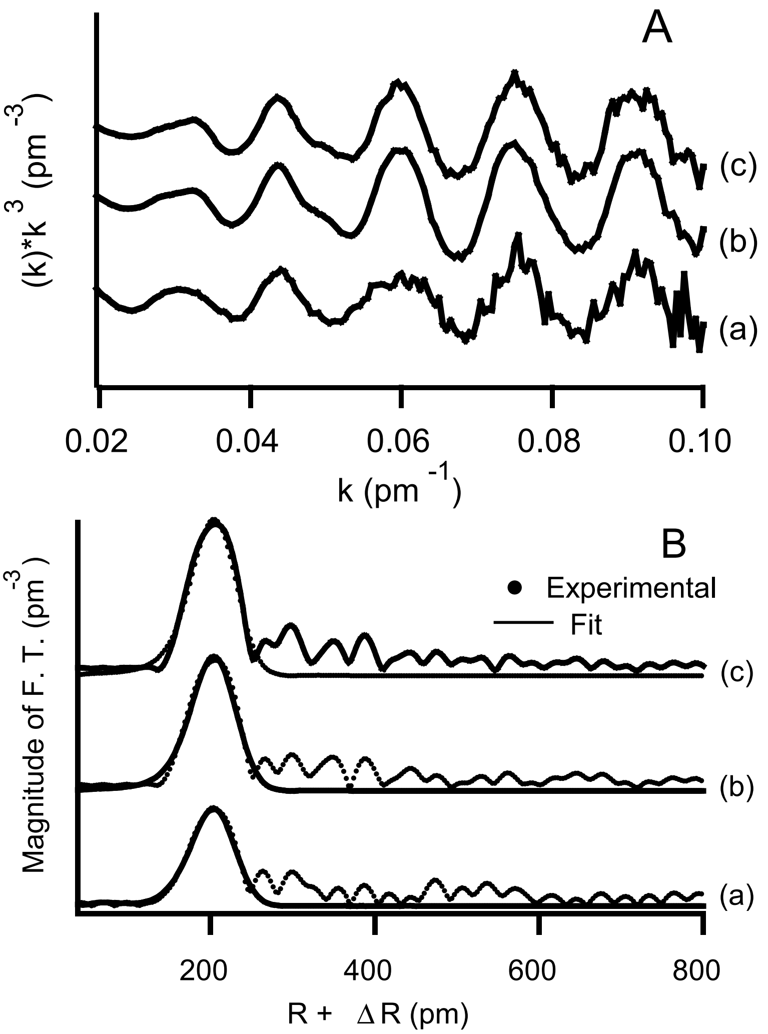

Figure 9.2. Co K-edge EXAFS spectra of nc-CdSe:Co (A) $k^3 \cdot \chi$ vs k; (B) F.T. vs R, experimental and fit(a) CdSe:Co 200 mg dopant ; (b) CdSe:Co 400 mg dopant; (c) CdSe:Co 700 mg dopant

9.3 Conclusions

The application of XAFS to the CdSe:Co system has furthered our understanding of this material, and by comparison to the Eu doped samples, we have clearly shown that the differences caused by the change in the charge and size of the guest ion can be closely traced using this technique.

Chapter 10

Neutron scattering characterization of Mn:ZnO

10.1 Introduction

The most efficient characterization of novel materials can be accomplished only by the combined utilization of local probes (XAFS, Mössbauer spectroscopy), sensitive to the short-range order present in the material and scattering techniques, which provide information about the spatial correlations. A specific type of materials that ultimately require this combined approach are nanocrystals alloys. These materials have been the object of intense research for many years because of their potential application in magneto-optical devices, as well as in the new developments of spintronics. At the nanoscale, the introduction of magnetic impurities in these semiconductors allows further tunability of their magnetic characteristics.

In work previously reported by our group [23] the interesting magnetic behavior of doped nanocrystalline semiconductors has been described. They showed the existence of an increase in the superexchange between Co^{2+} dopant ions in the nc-Co:CdSe confined system arising from changes in the nature of coupling in these size-restricted materials. These nanocrystals undergo a paramagnetic to spin-glass antiferromagnetic transition at temperatures between $2 - 4$ K, one order of magnitude higher than what is observed in the bulk, suggesting an enhanced long-range order of the Co distribution in the nanocrystals.

Nanocrystalline systems are polycrystalline, where the large ratio of surface to volume determines the optical, electric, and magnetic properties. Since the size of the single crystalline domains is commensurate with the length scale of some interactions, it is of great scientific and practical interest to investigate the influence of the high state of division in the magnetic properties of these materials. For example, in some cases magnetic coupling can happen only if the atoms with unpaired electrons reside in the same crystallite (magnetic domain), while in other cases a specific nanoparticle spatial arrange can allow mangetic interaction across the particle boundaries. The presence of a capping layer around the nanocrystals suggest that the greatest contribution should be intraparticle, but the experimental corroboration of this fact is needed.

The magnetic characteristics of the doped nanocrystlline materials are strongly dependent on the local environment around the magnetic impurity atoms. One important difference when comparing to bulk doped materials is the much greater proportion of atoms that are on the surface of the particles. In Figure 10.1 the proportion of surface to core atoms is plotted as a function of the nanoparticles size, assuming a spherical particle of wurtzite-type CdSe. The calculated values

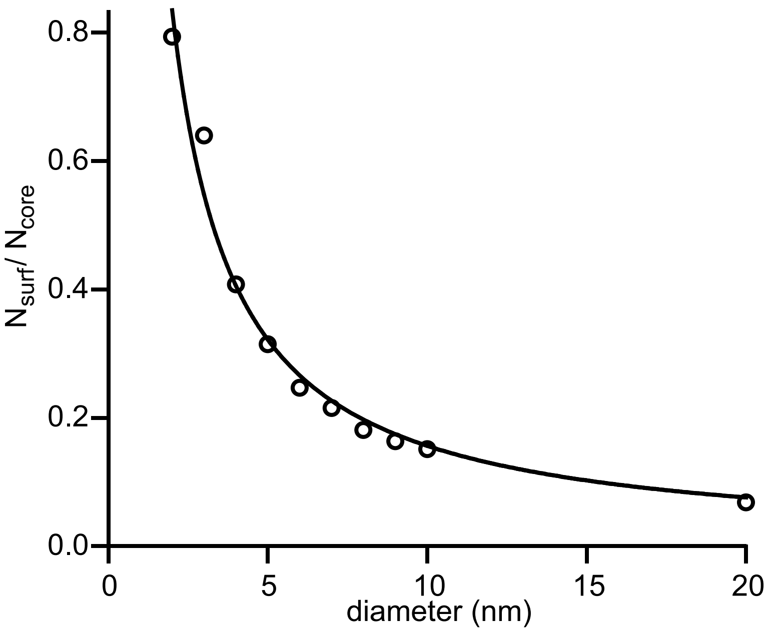

Figure 10.1. Proportion of atoms on the surface over atoms in the core for a spherical CdSe nanoparticle as a function of the particle diameter

can be fitted by the equation

$$\frac{N_{surf}}{N_{core}} = 1.7183 * d^{-1.041}$$

that shows the expected dependence on the inverse of the diameter.

It thus becomes important to establish if the dopant is distributed as an interstitial or substitutional defect in the core of the particle, segregated as a ternary (magnetic stripe) phase or segregated on the surface of the nanoparticles.

Neutron scattering constitutes a fundamental and widely used probe for magnetic structural studies in condensed phase. Thermal neutrons have a wavelength of the same order of interplanar distances in solids, and therefore neutron diffraction provide the same kind of information that can be obtained by x-ray diffraction. But neutrons have intrinsic magnetic moment and therefore they can interact with the magnetic moment generated by the electron clouds and the nuclei of the sample.

Recent developments in instrumentation and software allow for the simultaneous recording and use of the both the Bragg reflections and the diffuse scattering in a powder neutron diffractometer [2] in order to produce pair distribution functions (PDFs) that provide insight into the local structure of the materials, since the PDFs are mostly sensitive to the short-range order present.

A limitation of neutrons as an analytical probe is the limited flux available, therefore the sample volume required is considerably larger than what is required for synchrotron x-ray studies. Also the usefulness of the experiment is limited by the fact that some nuclei are very strong neutron absorbers. In most of this thesis we have used nanocrystalline CdSe as the material of choice, but due to the fact that Cd is a very strong neutron absorber, for the application of powder neutron diffraction we switched to nanocrystalline ZnO, doped with Co and Mn, to allow the neutron measurement.

10.2 Experimental

Two sets of magnetically doped nanocrystalline ZnO were prepared in ethanol solution according to the method developed by Radovanovic and coworkers [65]. In brief, 50 mL of 0.15 mol·L^{-1} LiOH in ethanol is added to 50 mL of a solution containing 0.1 mol·L^{-1} $Zn(CH_3COO)_2$ and 0.005 mol·L^{-1} $Co(CH_3COO)_2$ or $Mn(CH_3COO)_2$ in ethanol at 273 K. The temperature is raised to 298 K and the samples are allowed to grow in a water bath at that temperature for 5 days. The resulting nanocrystals were washed by repeated precipitation with heptane and resuspended in ethanol to form a clear colloidal solutions. The growth of the nanocrystals was monitored by visible absorption spectrometry. The nanocrystals were vacuum-dried and the free- flowing powder was chemically analyzed for Zn and concentration of dopant by ICP-AES, following the method detailed in Section 2.2. The analysis results are shown in Table 10.1.

Table 10.1. Analytic results magnetically doped ZnO nanocrystals

Sample	Zn (wt/wt %)	dopant (wt/wt %)	Proposed composition
1	80.33	0.00	ZnO
2	56.57	6.55	$Zn_{0.943}Co_{0.056}O$
3	60.19	2.88	$Zn_{0.975}Co_{0.025}O$
4	72.72	0.81	$Zn_{0.994}Co_{0.006}O$
5	63.73	3.69	$Zn_{0.968}Mn_{0.032}O$
6	66.89	2.39	$Zn_{0.980}Mn_{0.020}O$
7	70.12	0.62	$Zn_{0.995}Mn_{0.005}O$

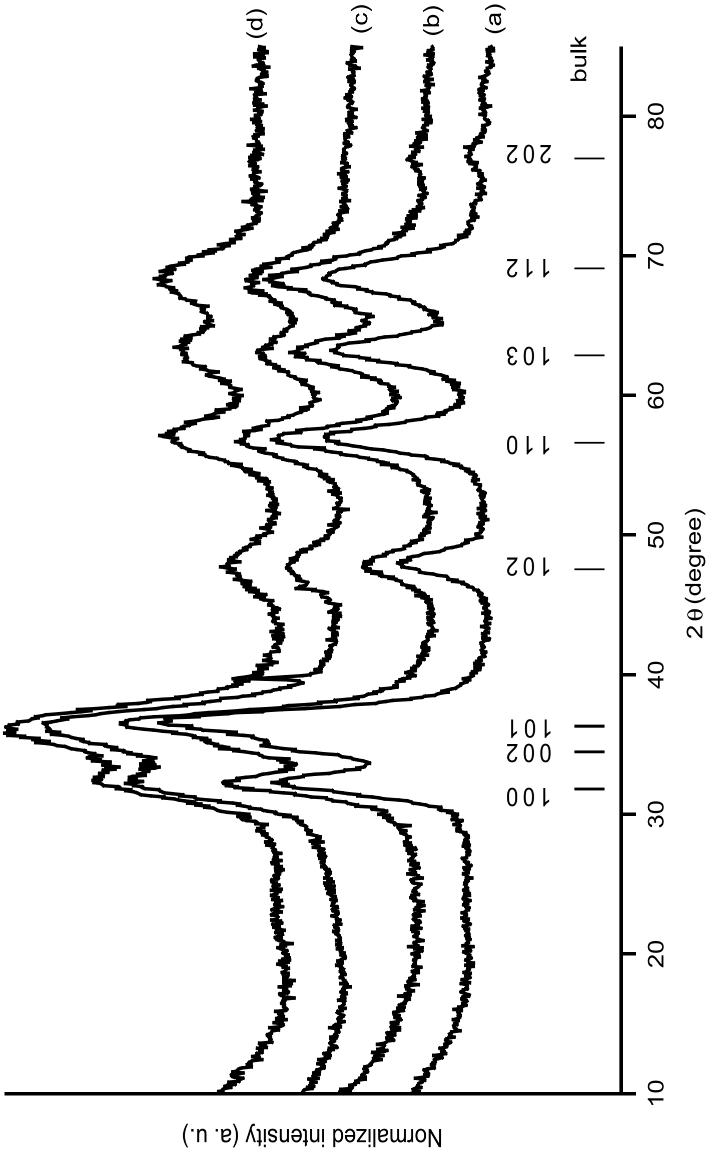
Normalized intensity (a. u.)
2θ (degree)
10
20
30
40
50
60
70
80
100
002
101
102
110
103
112
202
bulk
(a)
(b)
(c)
(d)

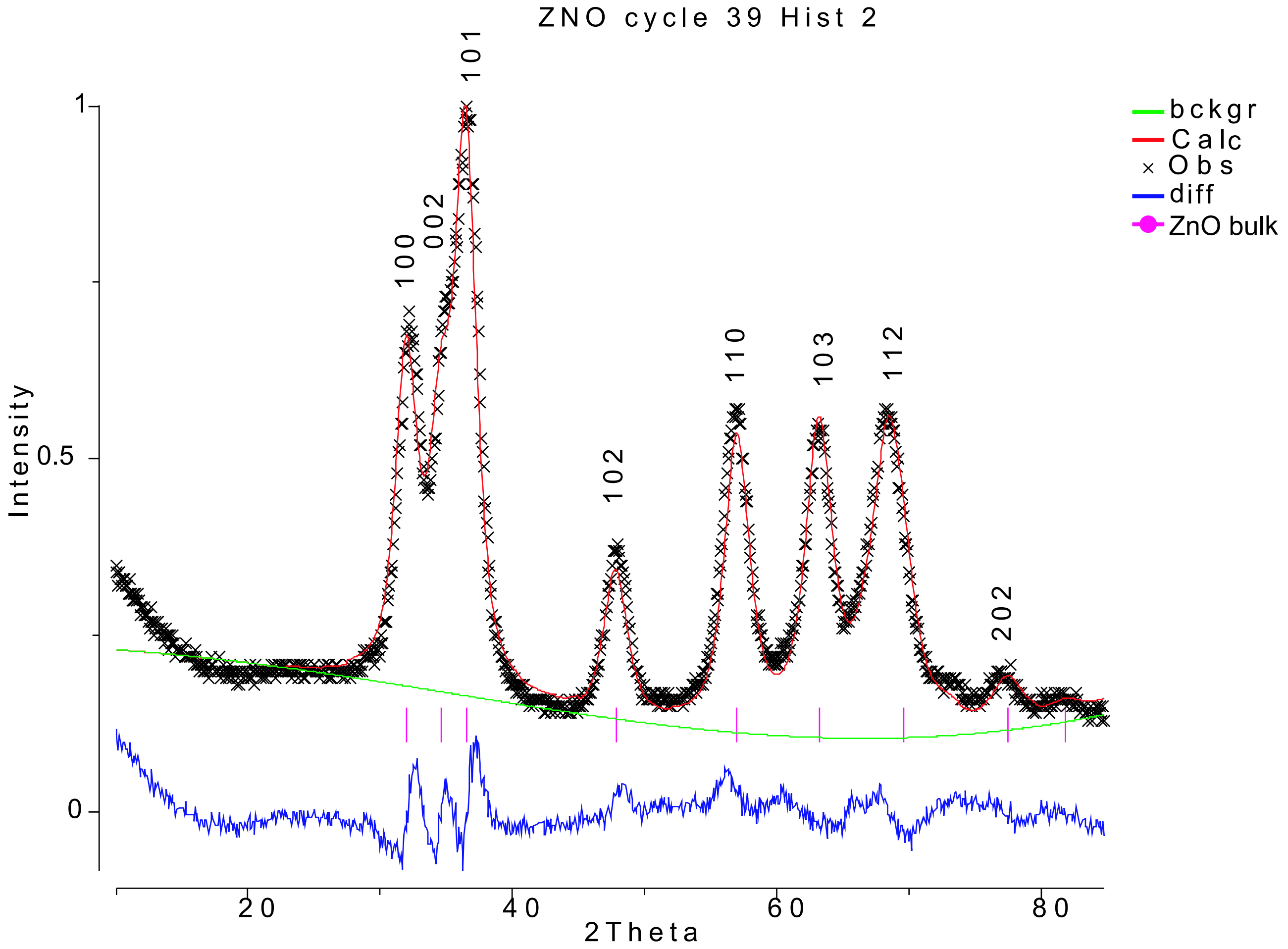

Figure 10.3. Rietveld refinement for nc-ZnO

The crystallinity and size distribution of the doped ZnO nanocrystals was estimated by powder XRD. The diffractograms shown in Figure 10.2 show the characteristic pattern of wurtzite-type crystal structure. The average size of the crystallites estimated from the Scherrer broadening, as explained in Section 3.1 is shown below in Table 10.3. The results of the limited simulation that can be achieved using traditional Rietveld methods as explained in Section 3.2, are shown on Figure 10.3, but the lattice parameters were again calculated by the simple fitting of a Gaussian function to the 100 and 112 reflections, details of the fitting of the (110) reflection are shown on Figure 10.4.

The neutron diffraction experiment was conducted at Lujan Neutron Science Center in Los Alamos National Laboratory, using the Neutron Powder Diffractometer (NPDF). This is a high resolution total scattering powder diffractometer with large detector coverage in the backscattering region. A schematic representation of the NPDF spectrometer is shown in Figure 10.5. The instrument is designed to collect data for pair distribution function (PDF) studies of disordered and nanocrystalline matter, and is also suitable for high resolution crystallographic studies.

The instrumental parameters are summarized on Table 10.2. The samples as free-flowing nanocrystalline powders were loosely packed up to 4/5 of the height of a 6.35 mm diameter by 38.1 mm high vanadium canister for an internal volume of 1.21 cm^3, sealed under helium exchange gas with an indium gasket. Data for each sample were collected for 10 h at two different temperatures (300 and 15 K).

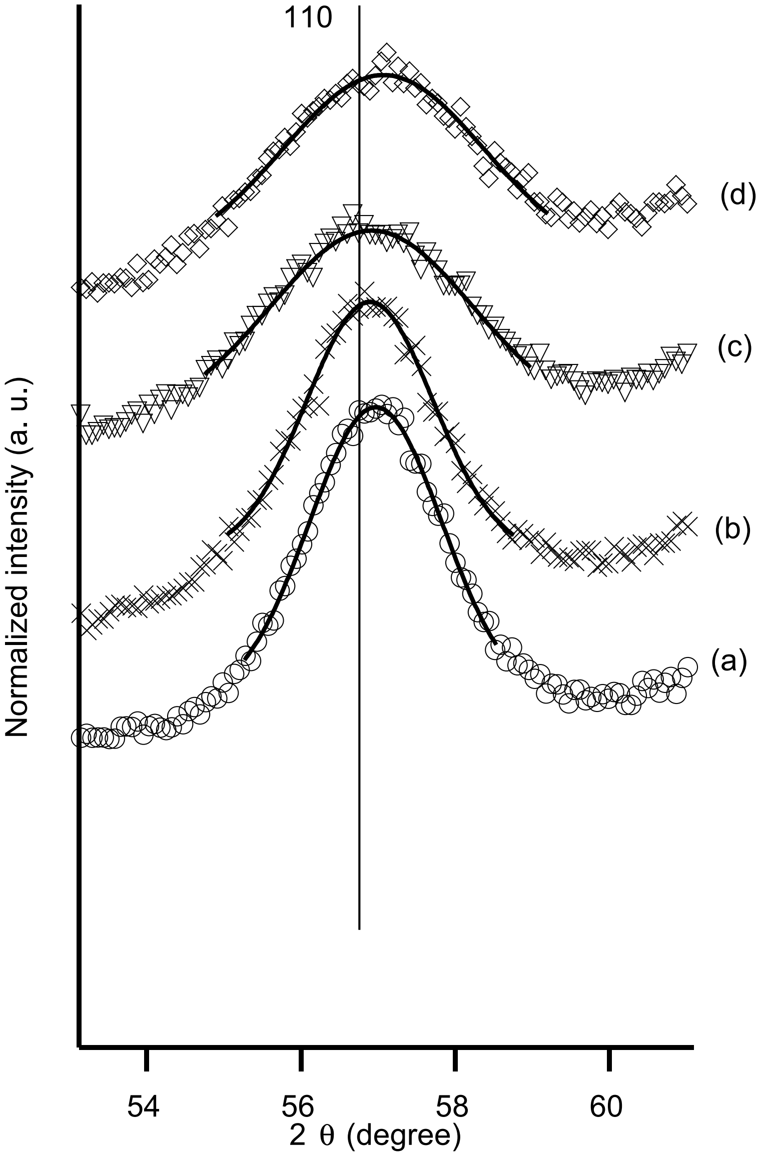

Figure 10.4. Fit of a Gaussian function to the broad (110) reflection in doped nc-ZnO

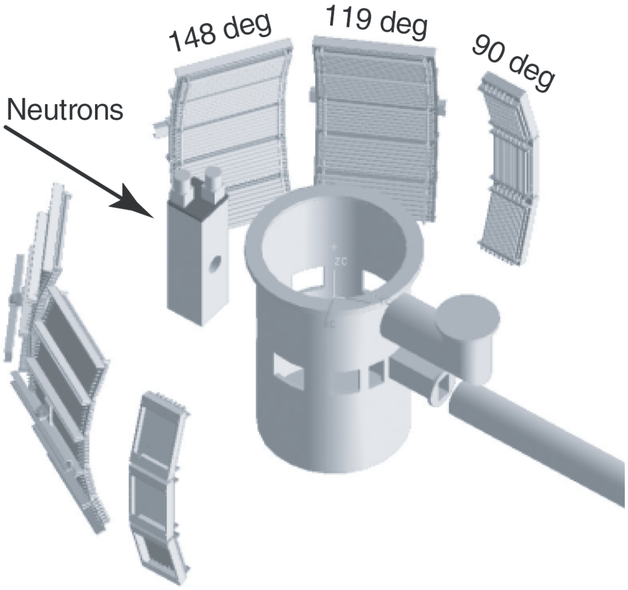

Figure 10.5. Schematic representation of the NPDF experimental station at LANSCE-LANL, from Reference [2]

General parameters			
Moderator	Chilled water (283 K)		
Flighpath	primary: 32m, secondary: 1.5m		
Beam size	5 cm high x 1 cm wide		
Detector bank information (DAQ setup)			
Bank	± 90	± 119	± 148
d-spacing (pm)	17 – 420	14 – 340	12 – 300
Q (pm^{-1})	0.0150 – 0.368	0.0185 – 0.4488	0.0209 – 0.5236
Measured Δd/d (%)	0.31	0.28	0.15
Detector type	124 ^{3}He tubes	80 ^{3}He PSDs	80 ^{3}He PSDs
Pixels	124	4000	4000
Pixel size(w x h, mm)	12.7 × 305	12.7 × 25.4	12.7 × 25.4
Ancillary equipment			
Displex	15 - 320K (closed cycle refrigerator)		

Table 10.2. Instrumental parameters for neutron diffraction experiment

10.3 Results and discussion

10.3.1 Size of nanocrystals

In Figure 10.8 the pair distribution functions (PDF) corresponding to bulk and nanocrystalline ZnO are shown. The amplitude of the oscillations have been normalized to the most frequent interatomic distance (Zn-O, first shell) and the graphs are offset for clarity. Inspection of this figure shows that whereas the PDF for the bulk material is undamped in the whole range of R over which the Fourier transform was calculated, in the case of the nanocrystalline sample it is difficult to distinguish the oscillations from the noise beyond 3500 pm. This distance corresponds approximately to the one fourth of the diameter of the nanoparticles, as shown in Figure 10.6, because the frequency of the atomic pairs separated by more than r_{core} drops exponentially with the increase of the distance.

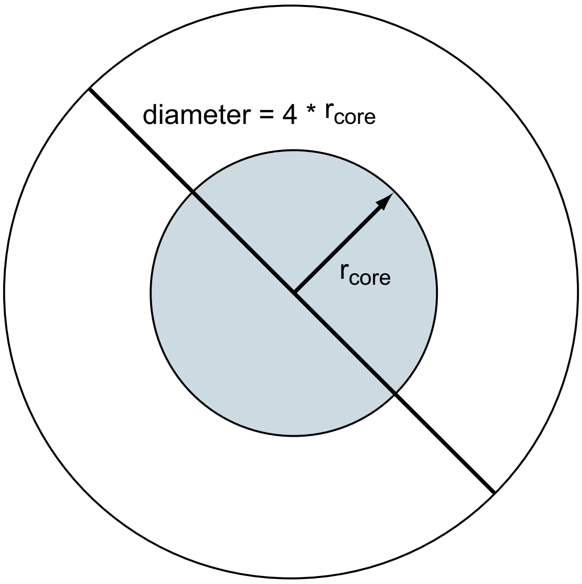

Figure 10.6. Schematic representation of critical core radius. The frequency of all atomic pairs separated by a distance longer than 2 r_{core} drops exponentially with the distance

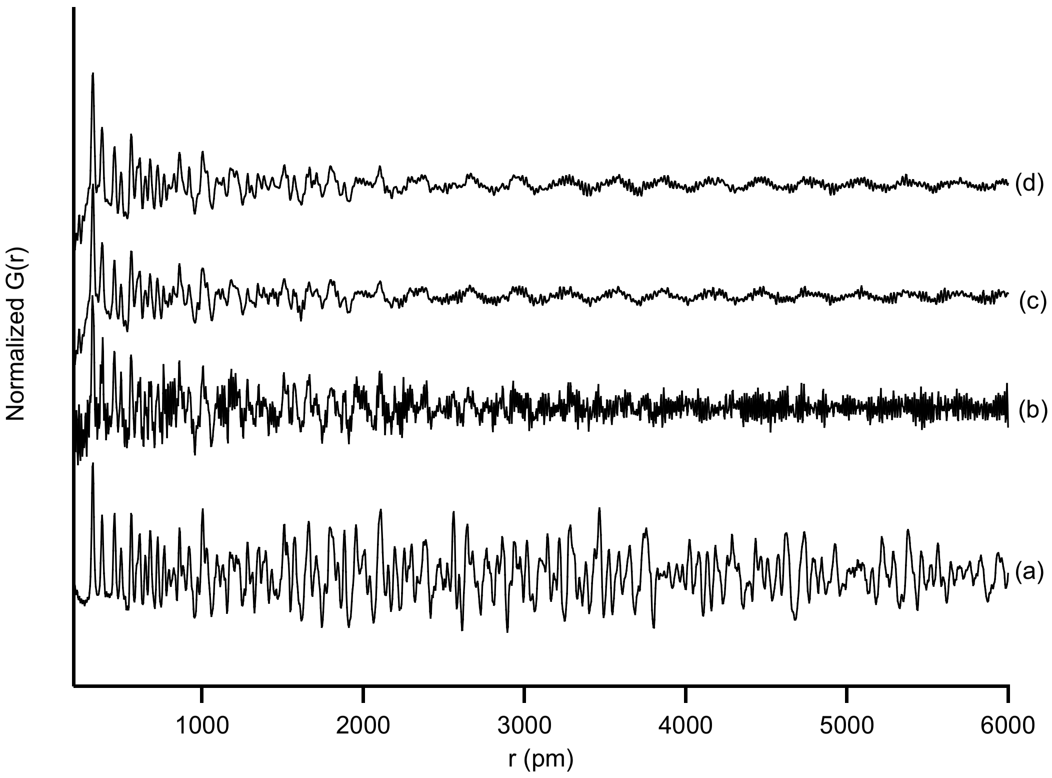

Figure 10.7. PDF of (a) bulk ZnO ; (b) nanocrystalline ZnO; (c) Mn:ZnO x = 0.020; (d)Mn:ZnO x = 0.032

Table 10.3. Comparison of nanoparticle size derived from Scherrer broadening with the size derived from neutron scattering PDF's

Sample	Size from XRD (nm)	Size from ND-PDF (nm)
nc-ZnO	28	29
ZnO:Mn x = 0.032	20	19
ZnO:Mn x = 0.020	20	17

In Figure 10.8A the maxima in the PDF have been fitted by an exponential function and the derivative of this function is plotted in the right axis vs. r, showing how the derivative asymptotically approaches zero. The same function and mathematic manipulation for the bulk sample in Figure 10.8B does not give any indication of a limited crystallite size.

In Table 10.3 we can appreciate good agreement between the size estimated from the neutron scattering data and the estimation derived from Scherrer broadening in the powder x-ray diffractograms as explained in Section 10.2.

10.3.2 Effect of introduction of dopant

A section of the PDF of samples of nanocrystalline ZnO containing around 2 mol % of Mn and Co collected at 15 K are shown in Figure 10.9. The PDF's are normalized to the frequency of the shortest Zn-Zn distance.

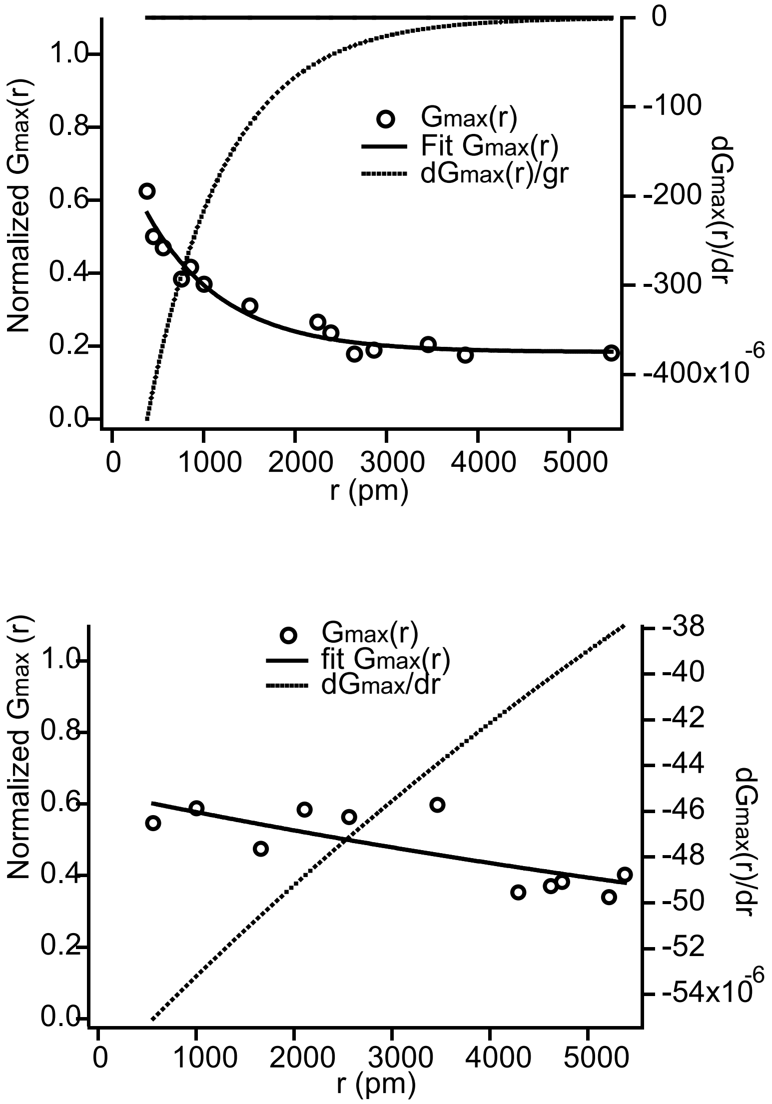

Figure 10.8. (A) Size of nanocrystals in nc-ZnO sample derived from the damping in the PDF (B) Bulk ZnO does not show appreciable damping of the PDF in the range of distances studied. Data points represent a sample of the maxima in the PDF's.

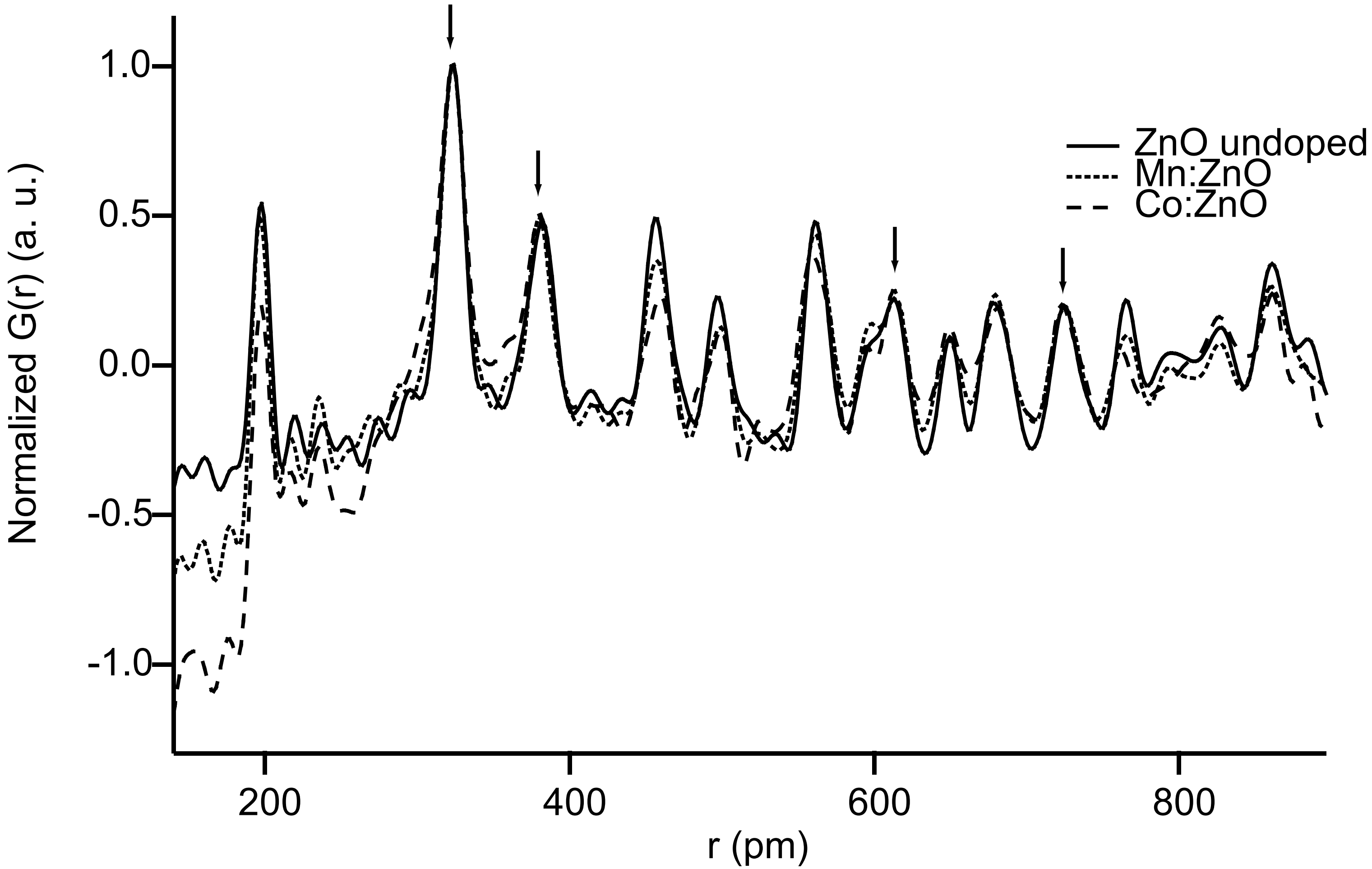

Figure 10.9. PDF of (a) nanocrystalline ZnO ; (b) Mn:ZnO, (c) Co:ZnO. The different curves are identified graphically and superimposed to show the sought effects. The arrow indicates pairs which frequency does not change with the presence of dopant

Strong evidence of substitutional doping can be derived from these plots. No new distances appear as a result of doping, ruling out the possibility of interstitial presence of the host. A remarkable feature in this graph is the fact that some pairs show the same frequency in the doped and undoped samples (peaks at 613, 724 pm) meanwhile most pairs show a smaller area in the doped samples. The explanation points again to substitutional doping, because the unchanged pairs correspond to distances anion-anion or cation-cation, which are insensitive to the substitution, but the distances involving cation-anion will show a variation in area due to the presence of two different pairs formed by atoms with different cross section for neutron absorption. A schematic representation of a fragment of the wurtzite-type ZnO structure shhowing the vectors corresponding to the maxima in the PDF is shown in Figure 10.10

10.3.3 Temperature effect

The NPDF allows to recording the of high resolution neutron powder diffraction from the samples as well. This is useful in the study of magnetic ordering at low temperature, because no changes in the PDF are to be expected because of the appearance of magnetic ordering, but in the diffractogram, a new magnetic phase will show as new diffraction peaks.

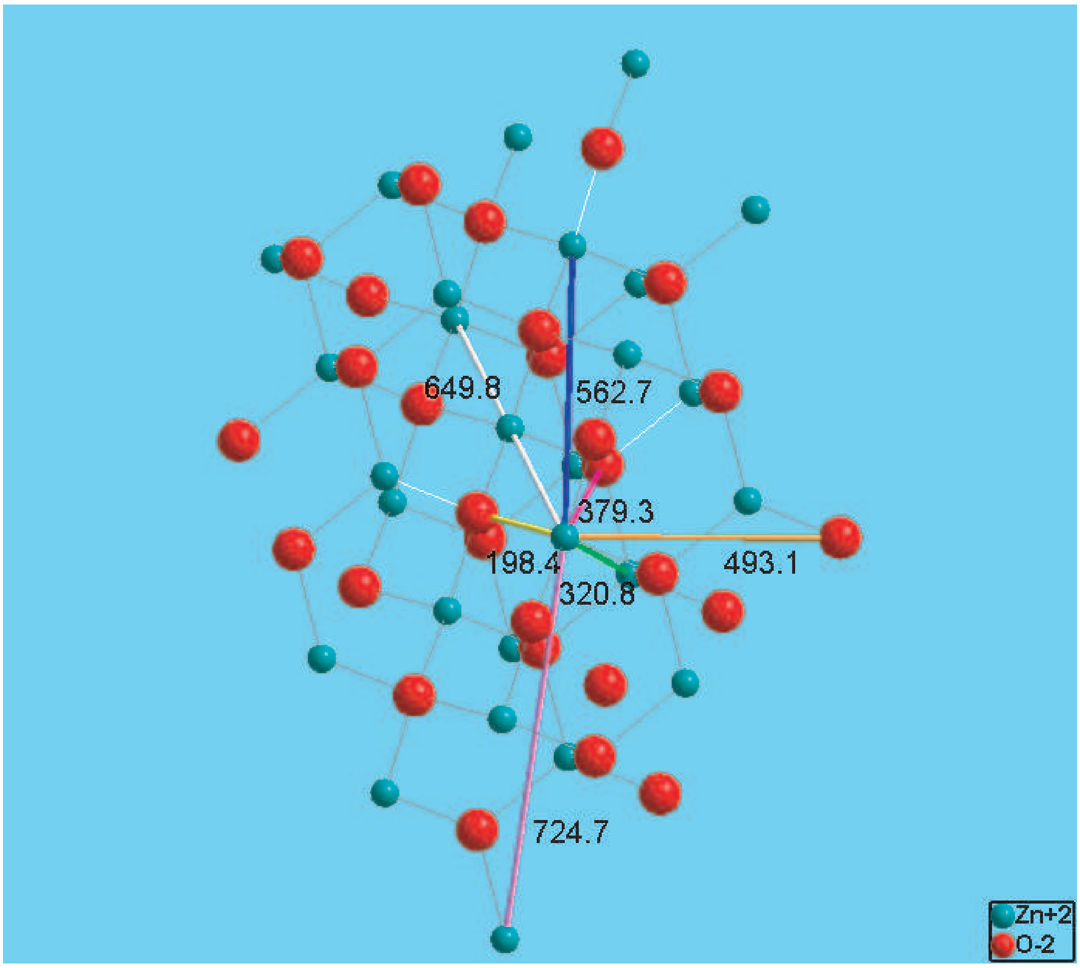

Figure 10.10. Fragment of the wurtzite-type ZnO crystal lattice showing the distances identified in the PDF of the nanoparticles.

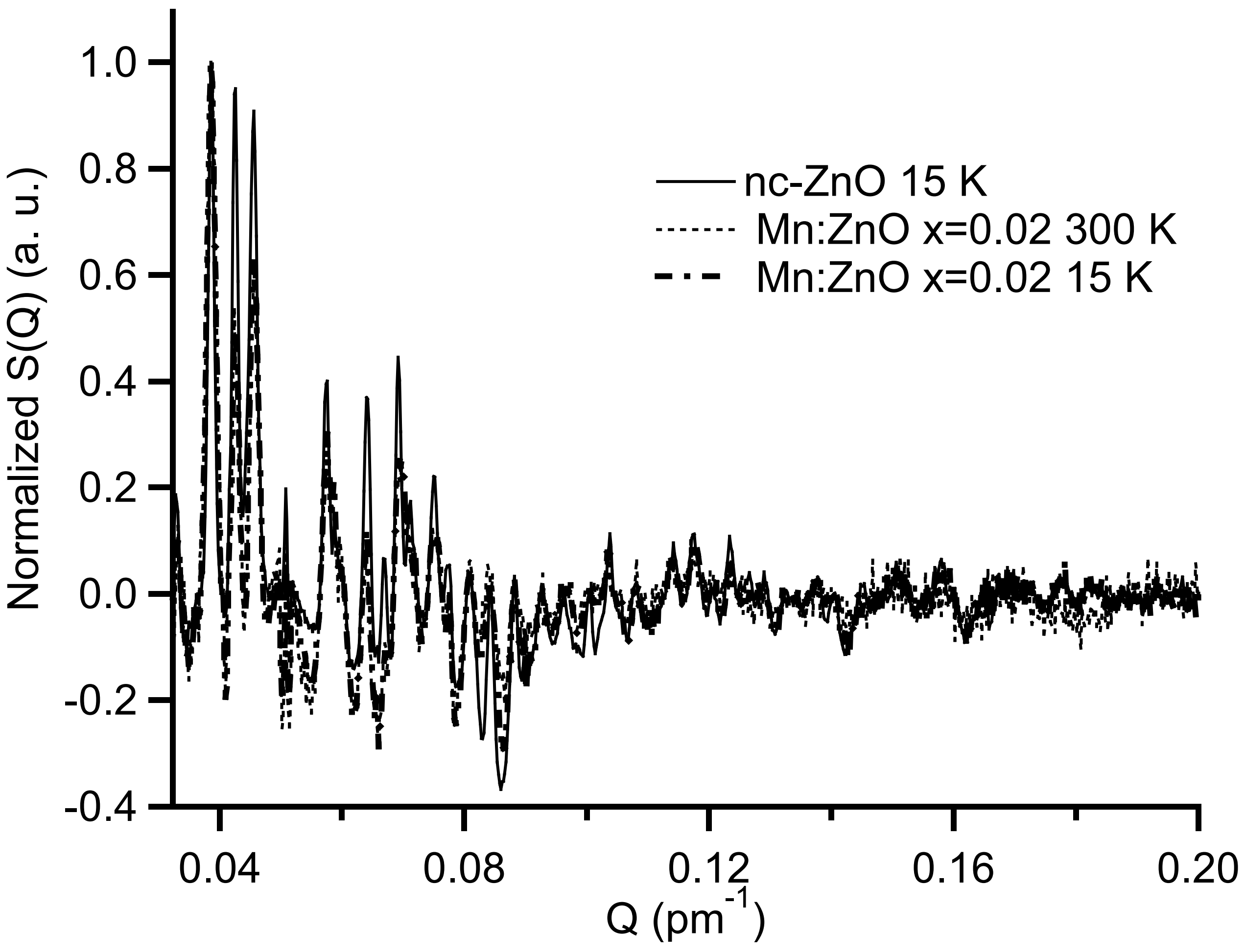

Figure 10.11. Powder neutron diffractogram of nanocrystalline Mn:ZnO x = 0.020(a) at 15 K; (b) at 300 K

In Figure 10.11 the neutron diffractograms of a Mn:ZnO sample with x=0.020 taken at 300 K and at 15 K are compared. The diffractogram of the undoped sample is also shown for reference. No new diffraction peaks appear at low temperature in the Mn doped sample, and therefore we can conclude that no new magnetic phase is formed in these materials up to the temperature explored. In a similar host-guest nanocrystalline material, Chang and coworkers [66] did not find antiferromagnetic ordering at temperatures as low as 5 K.

The Co-doped system does not show the appearance of new diffraction peaks indicating magnetic ordering within the nanocrystals. It has been reported that free-flowing nanocrystalline ZnO will not exhibit ferromagnetic ordering at low temperatures as theoretically predicted, but only when the nanoparticles agglomerate this type of magnetic behavior is observable [67].

Examination of the PDF shown in Figure 10.12 makes evident the presence of the dopant ion is since multiple distances appear split at 300 K. This behavior of the PDF in doped semiconductor materials has been previously reported in the study of bulk samples [68]. It is remarkable to find that those splittings in the pairs disappear at low temperature. This result is interesting because given the almost identical radii of Zn^{2+} (60 pm), Co^{2+} (58 pm) and Mn^{2+} (66 pm) [41], we did not expect a measurable splitting in these samples. It is noticeable, that the absence of splitting is consistent with with the absence of shift responding to Vegard's law in these materials, as shown in Section 10.2. A plausible explanation of this behavior can be given by the change in the crystallinity of the nanocrystals with the temperature, as has been discussed in the analysis of the EXAFS results of the CdSe:Eu materials.

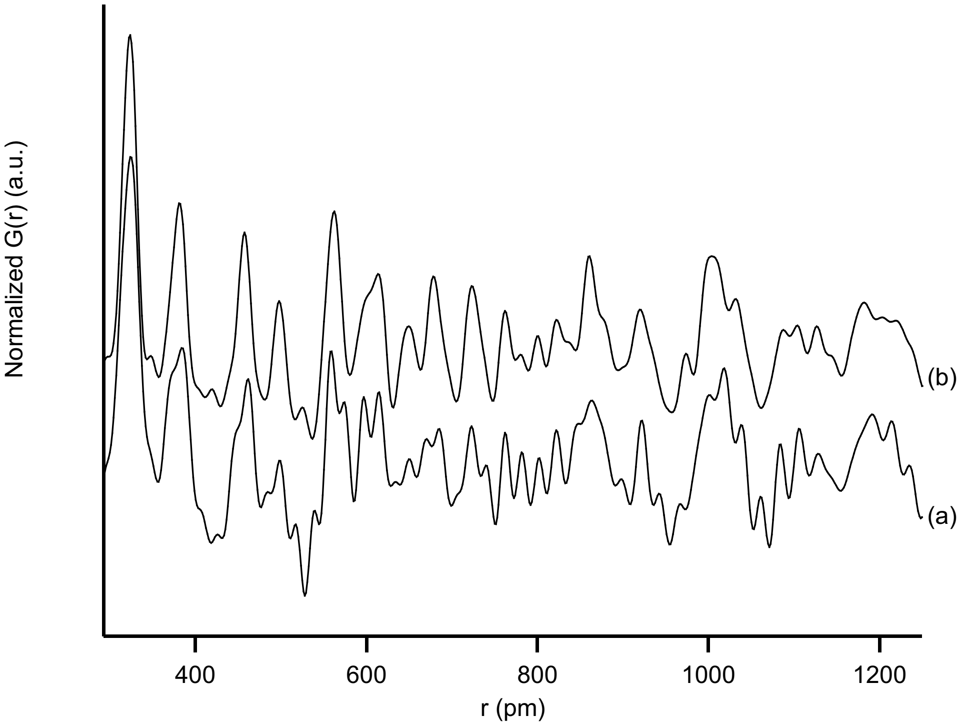

Figure 10.12. PDF of nanocrystalline Mn:ZnO x = 0.020(a) at 15 K; (b) at 300 K

10.4 Conclusions

The results obtained in this experiment have shown the suitability of neutron scattering techniques and more specifically of the recently developed high resolution total scattering (NPDF) machine at LANSCE for the study of local structure in nanocrystalline semiconductors.

The information that can be obtained by neutron scattering in some cases is complementary to data acquired by other analytical probes (ex. size of nanocrystals), but in other instances is unique to this technique, like the results showing the substitutional doping of manganese in the zinc sites of nc-ZnO.

The possibility of extending this study to cadmium-based materials is contingent upon the availability of samples synthesized with isotopically enriched Cd, since the naturally occurring isotope mixture is an extraordinarily strong neutron absorber (absorption cross section more than 2000 times larger than that of zinc). The isotopically purified materials can be very expensive to produce but the answers to the doping problems that can be provided by applying this technique might justify such an investment in future developments.

Another interesting possibility is the use of PDF based on synchrotron x-ray scattering, because in this case, the presence of Cd in the samples does not pose any particular difficulty. In any case, the PDF analysis will be a valuable tool for the further investigation into nanocrystalline systems, specially since it is not affected by the lack of long-range order that characterizes these materials.

Chapter 11

Future directions

- Z-contrast TEM.

  The ultimate prove of the guest ions position in a nanocrystalline semiconductor lattice could be provided by Z-contrast high resolution TEM, as described by Pennycock [69], and applied to the characterization of nanophase CdSe by Mew et al. [70].

  Preliminary data on our samples has been collected by Lupini and Pennycock [71] at the Electron Microscopy Lab of the Condensed Matter Sciences Division at Oak Ridge National Laboratory, using High-Angle Annular Dark-Field (HAADF) Microscopy, a variation of the Z-contrast technique. Figure 11.2 shows a selection of particles with different orientations of the sample CdSe:Eu x = 0.032, supported on a holey carbon film. At a higher magnification, a particle in the top right hand corner is close to the orientation where separate Cd and Se columns can be observed. The crystallinity of the sample is remarkable, as well as the absence of significant surface degradation for particles that had been prepared more than one year prior to this experiment and kept on air.

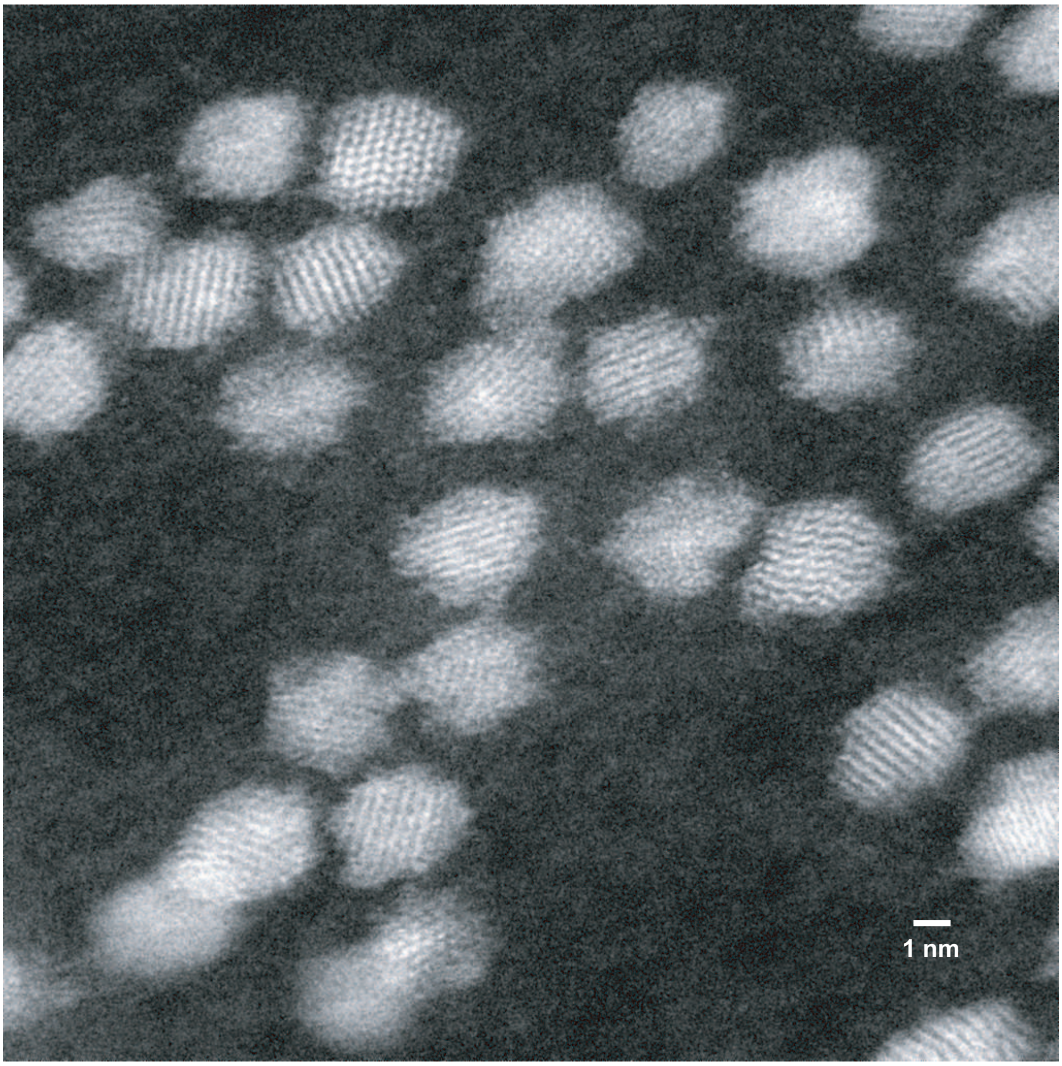

Figure 11.1. HAADF STEM micrograph of CdSe:Eu x = 0.032 nanoparticles, (Field of view 28.4 nm)

The main difficulty with this technique is getting the correct alignment of the nanoparticles and the fast drifting and damage caused by the electron beam. Further studies of the doped materials with these microscopy technique most likely will involve fixing the crystallites in a polymer matrix to get a better chance of observing the contrast difference generated by the difference in atomic number of the scatterers.

- Chemical reduction of dopant followed by the techniques discussed here and study of the new magnetic properties expected from that transformation. The variety of properties that can be generated by the chemical interconversion of Eu(II)/Eu(III) is a subject worth of further research, because of the potential applications of such systems in the emerging fields of nanomagnetics and spintronics.

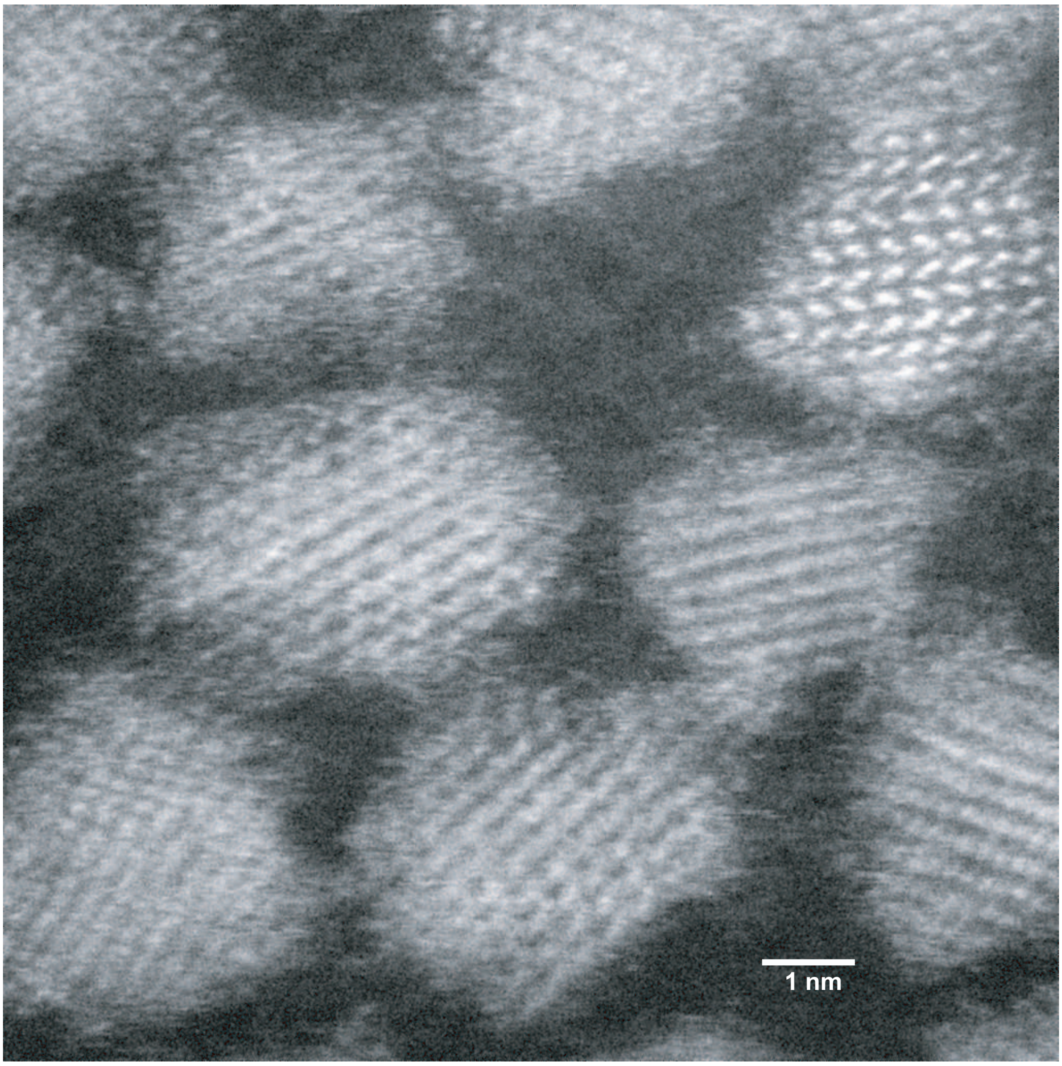

Figure 11.2. HAADF STEM micrograph of CdSe:Eu x = 0.032 nanoparticles, (Field of view 11.4 nm). The particle in the top right hand corner shows clearly atomic rows of Cd and Se

Chapter 12

Conclusions

The results of applying XAFS and Mössbauer spectrometry to the study of europium doped cadmium selenide nanocrystals provides evidence of the substitutional doping in the cadmium sites, together with an increase in the coordination around the cation and consequently with a more disordered environment around the absorbing atom, as shown by the decrease in the hight of the signal corresponding to the second coordination shells in the pseudo-RDF obtained by Fourier-transforming the EXAFS signal. Since the TEM and XRD data shown here and elsewhere show the conservation of the overall crystallinity in the nanoparticles, we conclude that the disorder is localized around the dopant. Another conclusion of this study is the understanding of the incorporation of europium into the crystalline lattice of the growing nanocrystals via an oxidative addition, since we did not succeed when trying to introduce Eu(III) directly into the reaction mixture but have proven to have Eu(III) as a dopant even if our starting material contained Eu(II) and the whole synthetic and characterization processes were carried out with exclusion of air.

Bibliography

[1] Grant Bunker. Elements of XAFS. *http://gbxafs.iit.edu/training/xafsoverview.pdf*, 1997.

[2] T. Proffen, T. Egami, S. J. L. Billinge, A. K. Cheetham, D. Louca, and J. B. Parise. Building a high resolution total scattering powder diffractometer upgrade of NPD at MLNSC. *Applied Physics A-Materials Science and Processing*, 74:S163–S165, 2002.

[3] International SEMATECH. International technology roadmap for semiconductors. http://public.itrs.net/Files/2003ITRS/Home2003.html,, 2003.

[4] A. I. Ekimov and A. A. Onushchenko. Quantum size effect in 3-dimensional microscopic semiconductor crystals. *JETP Letters*, 34(6):345–349, 1981. Article.

[5] C. B. Murray, C. R. Kagan, and M. G. Bawendi. Synthesis and characterization of monodisperse nanocrystals and close-packed nanocrystal assemblies. *Annual Review of Materials Science*, 30:545–610, 2000.

[6] A. D. Yoffe. Low-dimensional systems - quantum-size effects and electronic-properties of semiconductor microcrystallites (zero-dimensional systems) and some quasi-2-dimensional systems. *Advances in Physics*, 42(2):173–266, 1993.

[7] T. Trindade, P. O'Brien, and N. L. Pickett. Nanocrystalline semiconductors: Synthesis, properties, and perspectives. *Chemistry of Materials*, 13(11):3843–3858, 2001.

[8] R. Rossetti, J. L. Ellison, J. M. Gibson, and L. Brus. *J. Chem. Phys.*, 80:4464, 1984.

[9] C. Murray, D. J. Norris, and M. G. Bawendi. *J. Am. Chem. Soc.*, 115:8706, 1993.

[10] N. Revaprasadu, M. A. Malik, P. O'Brien, M. M. Zulu, and G. Wakefield. Single-source molecular precursors for the deposition of zinc selenide quantum dots. *Journal of Materials Chemistry*, 8(8):1885–1888, 1998.

[11] M. Lazell and P. O'Brien. A novel single source precursor route to self capping CdS quantum dots. *Chemical Communications*, (20):2041–2042, 1999.

[12] M. Shim, Wang Congjun, D. J. Norris, and P. Guyot-Sionnest. Doping and charging in colloidal semiconductor nanocrystals. *MRS Bulletin*, (December):1005, 2001.

[13] D. D. Awschalom and J. M. Kikkawa. *Physics Today*, 52:33, 1999.

[14] A. L. Efros, E. I. Rashba, and M. Rosen. Paramagnetic ion-doped nanocrystal as a voltage-controlled spin filter. *Phys. Rev. Lett.*, 87(20):206601, 2001.

[15] R. N. Bhargava, D. Gallagher, X. Hong, and A. Nurmikko. Optical-Properties of Manganese-Doped Nanocrystals of ZnS. *Physical Review Letters*, 72(3):416–419, 1994.

[16] R. N. Bhargava, D. Gallagher, and T. Welker. Doped nanocrystals of semiconductors - a new class of luminescent materials. *Journal of Luminescence*, 60-1:275–280, 1994.

[17] Perez-Conde J. Bhattacharjee, A. K. Optical properties of paramagnetic ion-doped semiconductor nanocrystals. *Physical Review B*, 68:045303, 2003.

[18] Christopher M. Bender, James M. Burlitch, Duane Barber, and Clifford Pollock. Synthesis and fluorescence of neodymium-doped barium fluoride nanoparticles. *Chem. Mater.*, 12:1969–1976, 2000.

[19] A. A. Bol, R. van Beek, and A. Meijerink. On the incorporation of trivalent rare earth ions in II-VI semiconductor nanocrystals. *Chemistry of Materials*, 14(3):1121–1126, 2002.

[20] F. V. Mikulec, M. Kuno, M. Bennati, D. A. Hall, R. G. Griffin, and M. G. Bawendi. Organometallic synthesis and spectroscopic characterization of manganese-doped CdSe nanocrystals. *Journal of the American Chemical Society*, 122(11):2532–2540, 2000.

[21] Thaddeus. Norman, Donny Magana, Thea Wilson, Colin Burns, Jin Z. Zhang, Daliang Cao, and Frank Bridges. Optical and Surface Structural Properties of Mn^{2+}-Doped ZnSe Nanoparticles. *J. Phys. Chem. B*, 107:6309–6317, 2003.

[22] S. L. Cumberland, K. M. Hanif, A. Javier, G. A. Khitrov, G. F. Strouse, S. M. Woessner, and C. S. Yun. Inorganic clusters as single-source precursors for preparation of CdSe, ZnSe, and CdSe/ZnS nanomaterials. *Chemistry of Materials*, 14(4):1576–1584, 2002.

[23] K. M. Hanif, R. W. Meulenberg, and G. F. Strouse. Magnetic ordering in doped $Cd_{1-x}Co_xSe$ diluted magnetic quantum dots. *Journal of the American Chemical Society*, 124(38):11495–11502, 2002.

[24] Ian G. Dance, Anna Choy, and Marcia L. Scudder. Syntheses, properties, and molecular and crystal structures of $(Me_4N)_4[E_4M_{10}(SPh)_{16}]$ (E = sulfur or selenium; M = zinc or cadmium): molecular supertetrahedral fragments of the cubic metal chalcogenide lattice. *Journal of the American Chemical Society*, 106(21):6285–95, 1984.

[25] A. Javier, D. Magana, T. Jennings, and G. F. Strouse. Nanosecond exciton recombination dynamics in colloidal cdse quantum dots under ambient conditions. *Applied Physics Letters*, 83(7):1423–1425, 2003.

[26] F. Parsapour, D. F. Kelley, and R. S. Williams. Spectroscopy of eu^{3+}-doped PtS_2 nanoclusters. *Journal of Physical Chemistry B*, 102(41):7971–7977, 1998.

[27] C. C. Chen, A. B. Herhold, C. S. Johnson, and A. P. Alivisatos. Size dependence of structural metastability in semiconductor nanocrystals. *Science*, 276(5311):398–401, 1997.

[28] W. Chen, J. O. Malm, V. Zwiller, Y. N. Huang, S. M. Liu, R. Wallenberg, J. O. Bovin, and L. Samuelson. Energy structure and fluorescence of Eu^{2+} in ZnS : Eu nanoparticles. *Physical Review B*, 61(16):11021–11024, 2000.

[29] Travis Jennings. *Private communication: Streak Camera TPL Fitting Program*. 2003.

[30] Y. N. Hwang, S. H. Park, and D. Kim. Size-dependent surface phonon mode of cdse quantum dots. *Physical Review B*, 59(11):7285–7288, 1999.

[31] G. Pass and H. Sutcliffe. Measurement of magnetic susceptibilities and adoption of SI units. *Journal of Chemical Education*, 48(3):180–181, 1971.

[32] Charles Kittel. *Introduction to solid state physics.* Wiley, New York, 7th edition, 1996.

[33] N. Tsujii, H. Kitazawa, and G. Kido. Magnetic properties of mn- and eu-doped zns nanocrystals. *Journal of Applied Physics*, 93(10):6957–6959, 2003.

[34] A. L. Patterson. The scherrer formula for x-ray particle size determination. *Physical Review*, 56:978–982, 1939.

[35] Leonid V. Azaroff. *Elements of X-ray Crystallography.* McGraw-Hill Book Company, 1968.

[36] B. H. Toby. Expgui, a graphical user interface for gsas. *Journal of Applied Crystallography*, 34(Part 2):210–213, 2001.

[37] A.C. Larson and R.B. Von Dreele. General Structure Analysis System (GSAS). Technical Report Report LAUR 86-748, Los Alamos National Laboratory, 1994.

[38] L Vegard. *Z. Phys.*, 5:17, 1921.

[39] M. A. Hines and P. Guyot-Sionnest. Synthesis and characterization of strongly luminescing zns- capped cdse nanocrystals. *Journal of Physical Chemistry*, 100(2):468–471, 1996.

[40] N. Samarth and J. K. Furdyna. *Proc. IEEE*, 78:990–1003, 1990.

[41] R. D. Shannon. Revised effective ionic radii and sytematic studies of interatomic distances in halides and chalcogenides. *Acta Crystallogr.*, A32:751–767, 1976.

[42] K. S. Hamad. *X-ray and photoelectron spectroscopy of the structure, reactivity and electronic structure of semiconductor nanocrystals.* Ph. D., University of California, 2000.

[43] Colvin V. L. Bowen Katari, J. E. and A. P. Alivisatos. X-ray photoelectron-spectroscopy of cdse nanocrystals with applications to studies of the nanocrystal surface. *Journal of Physical Chemistry*, 98(15):4109–4117, 1994.

[44] J. K. Furdyna. Diluted magnetic semiconductors. *Journal of Applied Physics*, 64(4):R29–R64, 1988.

[45] G. Concas, F. Congiu, G. Spano, M. Bettinelli, A. Speghini, and C. D. Flint. Investigation of structural questions on europium compounds by means of Eu-151 Mossbauer spectroscopy. *Zeitschrift fur Naturforschung Section A-A Journal of Physical Sciences*, 56(12):789–793, 2001.

[46] D. C. Koningsberger and Roelof Prins. *X-ray absorption : principles, applications, techniques of EXAFS, SEXAFS, and XANES.* Chemical analysis ; v. 92. Wiley, New York, 1988.

[47] D. E. Sayers, E. A. Stern, and F. W. Lytle. New technique for investigating noncrystalline structures - fourier analysis of extended x-ray - absorption fine structure. *Physical Review Letters*, 27(18):1204, 1971.

[48] Y. L. Soo, Z. H. Ming, S. W. Huang, Y. H. Kao, R. N. Bhargava, and

D. Gallagher. Local structures around mn luminescent centers in mn-doped nanocrystals of zns. *Physical Review B*, 50(11):7602–7607, 1994.

[49] J. Rockenberger, U. zum Felde, M. Tischer, L. Troger, M. Haase, and H. Weller. Near edge x-ray absorption fine structure measurements (XANES) and extended x-ray absorption fine structure measurements (EXAFS) of the valence state and coordination of antimony in doped nanocrystalline SnO_2. *Journal of Chemical Physics*, 112(9):4296–4304, 2000.

[50] Graham N. George. A suite of computer programs for analysis of x-ray absorption spectra. http://www-ssrl.slac.stanford.edu/exafspak.html,, 2000.

[51] Matthew Newville. *IFEFFIT*: interactive XAFS analysis and *FEFF* fitting. *Journal of Synchrotron Radiation*, 8(2):322–324, Mar 2001.

[52] B. Ravel. Exafs analysis with feff and feffit. *http://feff.phys.washington.edu/ ravel/*, 2001.

[53] O. E. Raola and G. F. Strouse. Synthesis and characterization of Eu-doped cadmium selenide nanocrystals. *Nano Letters*, 2(12):1443–1447, 2002.

[54] M. Berrettini and G. Strouse. *unpublished work,*, 2003.

[55] W. S. Yoon, K. K. Lee, and K. B. Kim. Structural and electrochemical properties of $LiAl_yCo_{1-y}O_2$ cathode for Li rechargeable batteries. *Journal of the Electrochemical Society*, 147(6):2023–2028, 2000.

[56] W. S. Yoon, K. B. Kim, M. G. Kim, M. K. Lee, H. J. Shin, J. M. Lee, J. S. Lee, and C. H. Yo. Oxygen contribution on Li-ion intercalation-deinterealation in $LiCoO_2$ investigated by O K-edge and Co L-edge X-ray absorption spectroscopy. *Journal of Physical Chemistry B*, 106(10):2526–2532, 2002.

[57] J. W. Sobczak, E. Sobczak, A. Kosinski, and A. Bilinski. XANES investigations of Pd-doped polyaniline. *Journal of Alloys and Compounds*, 328(1-2):132–134, 2001.

[58] A. A. Eliseev and O. A. Sadovskaya. Crystal chemical features of europium chalcogenides. *Izv. Akad. Nauk SSSR, Neorg. Mater.*, 13(8):1394–8, 1977.

[59] B. Ravel, E. Cockayne, and K. M. Rabe. The local structure of ferroelectric $Pb_{1-x}Ge_xTe$. *Journal of Synchrotron Radiation*, 6:567–569, 1999.

[60] B. Ravel, E. Cockayne, M. Newville, and K. M. Rabe. Combined EXAFS and first-principles theory study of $Pb_{1-x}Ge_xTe$. *Physical Review B*, 60(21):14632–14642, 1999.

[61] Z. R. Li, S. Q. Wei, Y. Wang, X. Y. Zhang, K. Q. Lu, and X. L. Chen. Local structures of nanocrystalline gan studied by xafs. *Journal of Synchrotron Radiation*, 8:830–832, 2001.

[62] O. Raola and G. Strouse. *unpublished work,*, 2001.

[63] K. Hanif and Strouse G.F. manuscript in preparation. 2004.

[64] B. V. Robouch and A. Kisiel. Exafs data resolved into individual site occupation preferences in quaternary compounds with tetrahedral coordinated structure. *Journal of Alloys and Compounds*, 286(1-2):80–88, 1999.

[65] P. V. Radovanovic and D. R. Gamelin. Electronic absorption spectroscopy of cobalt ions in diluted magnetic semiconductor quantum dots: Demonstration of an isocrystalline core/shell synthetic method. *Journal of the American Chemical Society*, 123(49):12207–12214, 2001.

[66] Chang Yong-Qin, Luo Xu-Hui, Xu Xiang-Yu, Li Lin, Chen Jin-Ping, Wang Rong-Ming, and Yu Da-Peng. Synthesis, Characterization and Magnetic Property Measurements of Zn $_{1-x}$ Mn $_{x}$ O Nanoparticles via Vapour Phase Growth. *Chinese Physics Letters*, 20(11):2058–2060, 2003.

[67] D. A. Schwartz, N. S. Norberg, Q. P. Nguyen, J. M. Parker, and D. R. Gamelin. Magnetic quantum dots: Synthesis, spectroscopy, and magnetism of Co^{2+}- and Ni^{2+}-doped ZnO nanocrystals. *Journal of the American Chemical Society*, 125(43):13205–13218, 2003.

[68] Billinge S. J. L. Egami T. Proffen, T. and D. Louca. Structural analysis of complex materials using the atomic pair distribution function – a practical guide. *Z. Kristallogr.*, 218:132–143, 2003.

[69] S. J. Pennycook. Z-contrast transmission electron-microscopy - direct atomic imaging of materials. *Annual Review of Materials Science*, 22:171–195, 1992.

[70] A. Mews, U. Banin, A. V. Kadavanich, and A. P. Alivisatos. Structure determination and homogeneous optical properties of CdS/HgS quantum dots. *Berichte Der Bunsen-Gesellschaft-Physical Chemistry Chemical Physics*, 101(11):1621–1625, 1997.

[71] A. Lupini and S. J. Pennycook. Personal communication. 2003.

Appendix: XAFS data processing

There are many programs available, both free and commercial, for the data processing of XAFS experiments. Each choice has pros and cons, since many compromises have to be made in the development of this type of software. The package IFEFFIT[1] in theory would allow to do all stages of data processing. I prefer do use a two-stage approach, doing the preliminary processing with EXAFSPAK and only then going to Athena/Artemis (based both on IFEFFIT).

12.1 From raw data to DAT file

I have used a specific file set of Se K-edge data. Change the element, edge, energy, etc. accordingly when processing other data sets. Check the EXAFSAK manual[2] for further information.

1. Move to the directory where you have stored the raw data files. **Raw data** from SSRL beamline 7-3 is gathered as data files with *.xxx, where xxx is a consecutive number for the different repetitions of the same sample.

2. Issue the command `mview <filespec> /num=8-28/den=4/notakelogs` or the former plus `/sum` to view your data and make sure it makes sense. You should get something like Figures 12.1 and 12.2. For transmission data, the command line should read: `mview <filespec> /num=4/den=5/takelogs`

3. Calibrate the energy of the spectra. For the first file of the list issue the command `mcalib /elem=se/edge=k <filespec.001> /newfile`. After that issue the command increasing the consecutive number and removing the

---

[1] for the full documentation see `http://cars9.uchicago.edu/ifeffit/tutorial/tutor.html`

[2] `http://www-ssrl.slac.stanford.edu/ george/exafspak/manual.pdf`

`/newfile` option. Make sure that the first inflection in the standard spectrum is selected before hitting `<Enter>`. The screen should look like Figure 12.3.

4. Check the structure of the *calibrate.dat* file and make sure that the value appearing in the heading of the file is the intended value for the energy of the absorption edge.

```
Se K  Edge,  Table Value :  12658.00000eV  Za : 34.0 I-edge :   1
    Calibration   filename
    12653.278   cdeuse8_se_006.001
    12653.185   cdeuse8_se_006.002
    12653.180   cdeuse8_se_006.003
    12653.178   cdeuse8_se_006.004
```

   Tabular value for Se K-edge = 12658 eV[3]

5. Run `mave /out=<filespec.ave>` using all the defaults except the positions for the numerator channels that should be 8,28 for fluorescence and 4 for transmission.

6. Call program `process <filespec.ave>`. Subtract a pre-edge polynomial of degree -1, calculate the spline resetting the defaults and make sure that you are dealing with the right edge. The final fallout should be close to 1. Calculate the EXAFS, smooth it and calculate the Fourier transform without phase correction and k=3 weighting . Exit to the top menu and go to the option 6 `file input/output`. Save the `filespec.ave` file (option 1) and a text `filespec.frm` file (option 2) with four columns (E [eV], k, I_0 and μ), which is done by accepting the defaults. The different stages of the process are summarized in Figures 12.4 and 12.5.

---

[3] Thompson, A. et al., *X-Ray Data Booklet.* Center for X-Ray Optics and Advanced Light Source, Berkeley, 2001

7. Once you get to this point and you are sure that your data makes sense, specially for the EXAFS and the FT plots, you will want to create a file that is directly readable by Athena. To generate the `<filespec>.dat` file, load Mathematica notebook `trim_frm.nb`, to execute the following set of operations:

```
Isolating the needed data from the frm files by O. Raola, 2003


SetDirectory["E:/Working files/1_Data/XAS/Mar2003/frm files"]
ReadFile = "cdsebulk_se_005.frm"
OutFile = "cdsebulk_se_005.dat"

TemporaryTable = Import[ReadFile, "Table"];

OutputTable =TemporaryTable[[All, {1, 4}]];

Export[OutFile, OutputTable]
```

   You have to supply the full path to the directory where your data is and the names of input and output files. Execute the notebook and you will have created the `<filespec>.dat`, a plain-text file containing E and mu(E) two columns, separated by spaces with no headings.

12.2 Athena and Artemis processing

8. Open from the DAT file using Athena[4]. Athena allows you to save ASCII files at different points of the processing. These files can be read in Igor

---

[4] For a complete tutorial on the use of this application check `http://feff.phys.washington.edu/ ravel/software/exafs/doc/Athena/athena.html`

in order to further explore and compare the data, as well as to produce publication-quality graphics. You will also consider saving the Athena project in as a separate file, what gives you the possibility of coming back to the same stage of the analysis every time you need to.

9. The last and most important stage of this endeavor is the modelling step. The files processed by Athena can be opened in Artemis[5], where all the modelling is done. . The modelling in Artemis requires theoretical phase and amplitude functions calculated by FEFF. To prepare the FEFF input, based on the crystallographic description of your model, use ATOMS[6]. FEFF itself is run on a DOS-shell by calling the executable inside the directory that contains the file `feff.inp` generated by atoms.

---

[5] For a complete tutorial on Artemis see `http://leonardo.phys.washington.edu/ ravel/software/exafs/doc/artemis.pdf`

[6] `http://leonardo.phys.washington.edu/ ravel/software/exafs/doc/Atoms/`

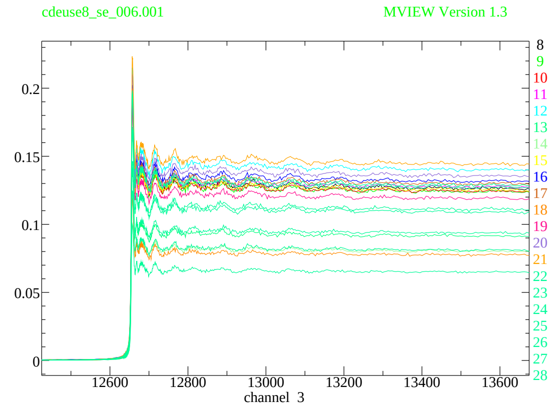

Figure 12.1. Output of mview

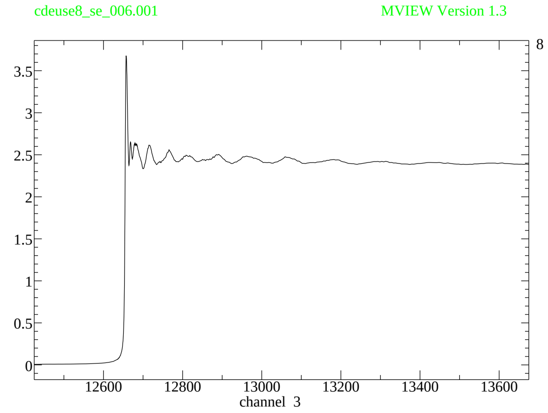

Figure 12.2. Output of mview with sum opiton

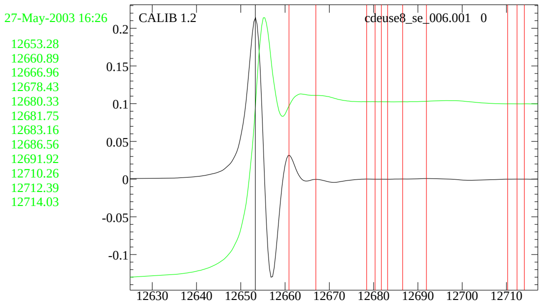

Figure 12.3. Calibration of XAS data

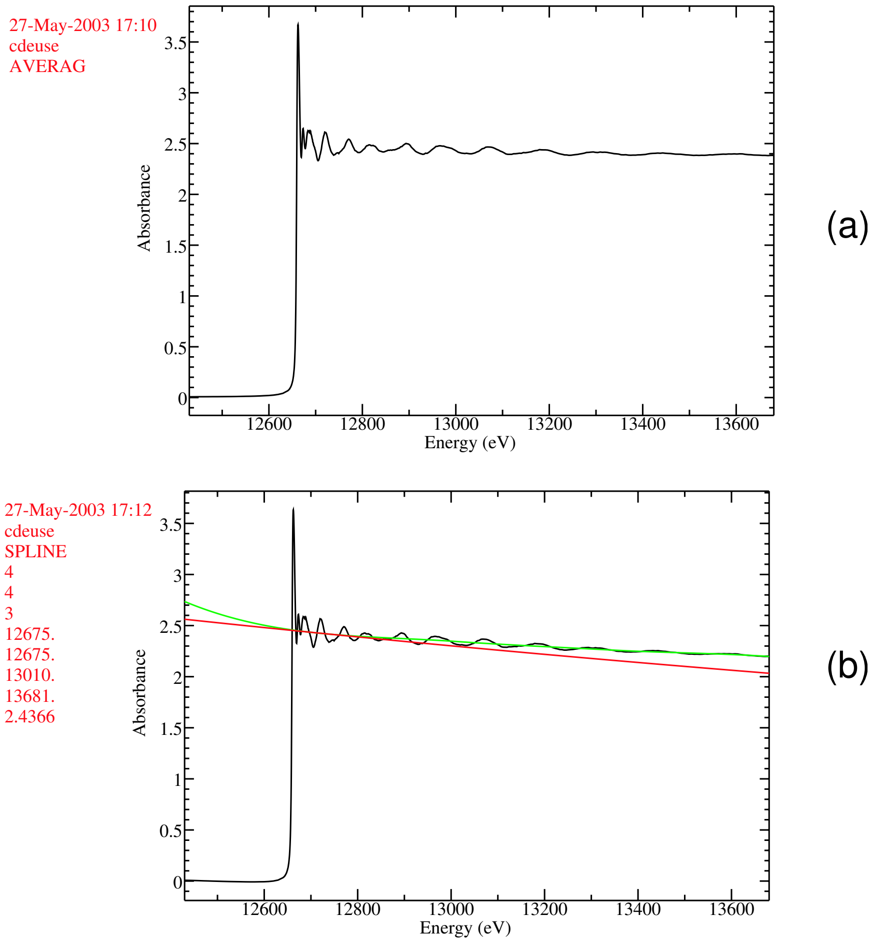
27-May-2003 17:10
cdeuse
AVERAG
Absorbance
0
0.5
1
1.5
2
2.5
3
3.5
12600
12800
13000
13200
13400
13600
Energy (eV)
(a)
27-May-2003 17:12
cdeuse
SPLINE
4
4
3
12675.
12675.
13010.
13681.
2.4366
Absorbance
0
0.5
1
1.5
2
2.5
3
3.5
12600
12800
13000
13200
13400
13600
Energy (eV)
(b)

Figure 12.4.

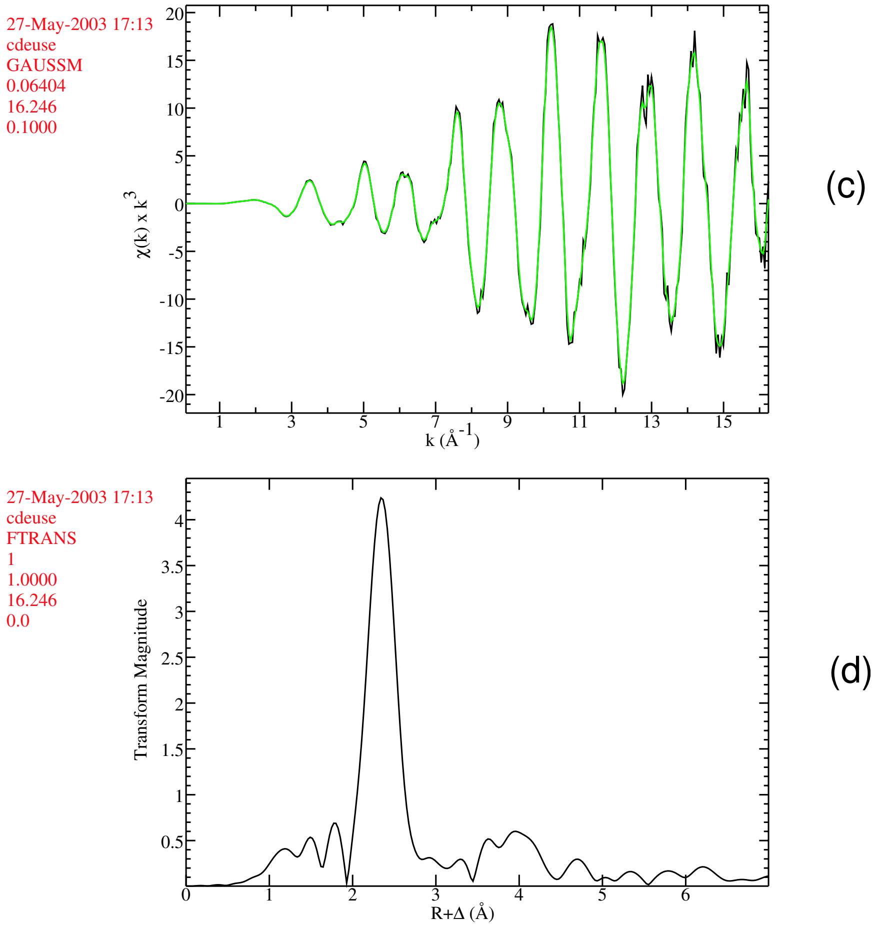

Figure 12.5. Results of `process` operation